# Replacive formation of sulphides in the oceanic lithosphere and the effect on rock porosity evolution

A thesis submitted to attain the degree of

Doctor of the Natural Sciences

(Dr. rer. nat.)

at the Department of Geosciences, University of Bremen

Catharina Louise Los

Bremen, September 2017

Date doctoral colloquium: 17 November 2017

Supervisor: Wolfgang Bach
Second reviewer: Jürgen Koepke

# Abstract

Circulation of hydrothermal fluids in the oceanic lithosphere facilitates mass and energy transfer between lithosphere and hydrosphere. High porosity in the shallow crust enables infiltration of seawater, which becomes heated and reduced at depth and leaches metals from the host rock. The resulting hot ($\sim$350°C) metal-rich fluid is buoyant and rises back up to the surface where it mixes with seawater or seawater-derived fluids. Concomitant changes in pH, temperature and oxidation state result in the precipitation of metals as sulphide minerals. The interplay of discharging fluids and seawater is especially visible in sulphate chimneys, where anhydrite precipitation and corrosion likely control porosity and sulphide formation in the chimney conduit. To analyse the onset of replacive sulphide growth we subjected an anhydrite fragment from the Pacmanus vent field to Electron Microprobe Analysis and Transmission Electron Microscopy as well as 3D analysis with a Focussed Ion Beam cut that was imaged through Scanning Electron Microscopy. Sulphides were observed in pore space, either in anhydrite cleavage planes or at grain boundaries. Sulphide assemblages at grain boundaries had a chaotic texture where pyrite was surrounded by colloform chalcopyrite (indication for a temperature increase) and later pyrite and sphalerite (temperature decrease). The growth on dissolving surfaces and a continued pore fill with sulphide phases at different temperatures confirmed the hypothesis that porosity generation is crucial for sulphide formation and reaction progress in this environment.

Within the oceanic lithosphere, replacive sulphide mineralization is more extensive and can form massive sulphide deposits. Such deposits are found along diverging oceanic plates, both with a fast and slow spreading rate. Not all spreading centers have experienced sulphide mineralization, however. Batch experiments placing several oceanic lithologies (peridotite, troctolite, basalt, serpentinite) in contact with a synthetic, $H_2S$-bearing vent fluid showed that the potential to form sulphides was much larger in the less reducing environment represented by basalt. The olivine-bearing lithologies showed magnetite growth instead, indicating that sulphur activity was too low to form sulphides such as pyrite or pyrrhotite. The largest sulphide deposits should thus be expected at basalt-hosted hydrothermal systems.

Upon shallow infiltration and heating of seawater in the oceanic crust, oxidizing conditions prevail and sulphate can be captured as anhydrite. This mineral has a retrograde solubility, meaning that it dissolves upon cooling. For inactive hydrothermal chimneys this can mean collapse; in the

crust it accounts for severe changes in rock permeability. The onset of anhydrite growth in fractured basalt in a flow-through experiment was found to be difficult at temperatures below 150°C. Only at temperatures higher than 120°C a small amount of anhydrite was observed. At this low temperature hydrothermal alteration, many Fe-bearing phases such as hematite and magnetite were visible at different depths in the basalt core. Changes in iron mineralogy with depth once again stress the important role of oxygen and porosity in hydrothermal processes, including transport of metals such as Fe and precipitation of sulphur-bearing minerals.

## Zusammenfassung

Die Zirkulation von hydrothermalen Fluiden innerhalb der ozeanischen Lithosphäre fördert den Massen- und Energietransport zwischen Lithosphäre und Hydrosphäre. Die hohe Porosität der obersten Kruste ermöglicht das Eindringen von Meerwasser, das wiederum in der Tiefe erhitzt und reduziert wird und Metalle aus dem Wirtsgestein laugt. Das daraus resultierende heiße ($\sim$350°C), metall-reiche Fluid steigt durch den Auftrieb zurück zum Meeresboden auf. Dort vermischt es sich mit dem Meerwasser oder mit Meerwasser geprägten Fluiden. Die begleitenden Änderungen des pH, der Temperatur und der Oxidationsstufe, führen zur Ausfällung von Metallen in Form von Sulfid-Mineralen. Das Zusammenspiel von austretenden Fluiden und Meerwasser wird besonders anhand von Sulfat-Schloten deutlich, bei denen voraussichtlich die Ausfällung und erneute Lösung von Anhydrit die Porosität und Entstehung von Sulfiden im Inneren des Schlotes steuert. Um den Beginn des Ersätzungsvorgangs durch Sulfide zu analysieren, wurde ein Anhydrit-Fragment aus dem Hydrothermalfeld Pacmanus mittels Elektronenstrahl-Mikroanalyse, Transmissionselektronen-Mikroskopie und 3D Analyse mittels FIB-SEM untersucht. Sulfid-Mineralisationen wurden in Porenräumen, entweder entlang von Anhydrit Spaltflächen oder an Korngrenzen, beobachtet. Auftretende Ansammlungen von Sulfiden entlang von Korngrenzen zeigen eine chaotische Struktur, bei der Pyrit umgeben ist von kolloformem Chalcopyrit (Hinweis auf einen Temperaturanstieg) und späterem Pyrit und Sphalerit (Temperaturabstieg). Das Wachstum an sich lösenden Oberflächen und eine sich fortsetzende Verfüllung der Poren mit Sulfidphasen bei unterschiedlichen Temperaturen, bestätigt die Hypothese dass die Entstehung von Porosität einen entscheidenden Beitrag zur Ausfällung von Sulfiden und für den Reaktionsfortschritt in dieser Umgebung leistet.

Innerhalb der ozeanischen Lithosphäre ist die ersetzende Sulfid-Mineralisation extensiver und es kann zur Ausbildung von Massiv-Sulfid-Erzen kommen. Solche Ablagerungen treten entlang von

divergenten Plattengrenzen auf, sowohl bei schnell als auch langsam spreizenden Rücken. Allerdings sind Sulfid Mineralisationen nicht in jeder Spreizungszone zu beobachten. Bei Batch Experimenten wurden unterschiedliche ozeanische Lithologien (Peridotit, Troktolith, Basalt, Serpentinit) in Kontakt mit einem synthetischen, $H_2S$-haltigen Fluid gebracht. Anhand dessen wird gezeigt, dass das Potential Sulfide zu Bilden deutlich höher unter weniger reduzierenden Bedingungen ausfällt, hier repräsentiert durch den Basalt. Die Olivin beinhaltenden Lithologien zeigen hingegen das Wachstum von Magnetit. Dies deutet daraufhin, dass die Schwefelaktivität zu gering gewesen ist um Sulfide, wie Pyrit oder Pyrrhotin zu bilden. Die größten Sulfid Ablagerung sind demnach in hydrothermalen Systemen zu erwarten, die Basalt als Wirtsgestein aufweisen.

In der obersten Kruste herrschen oxidierende Bedingungen vor, wodurch Sulfat in Form von Anhydrit gebunden werden kann. Anhydrit zeigt eine retrograde Löslichkeit, was bedeutet dass es zur Lösung beim Abkühlen kommt. Im Falle von inaktiven Schloten kann es dadurch zu einem Kollaps kommen; in der Kruste kann dies die Ursache für stärke Änderungen der Gesteinspermeabilität sein. Durchgeführte Durchflussexperimenten zeigen, dass die Ausbildung von Anhydrit in Basalt unterhalb von 150°C stark gehemmt ist. Nur bei Temperaturen höher als 120°C konnte eine kleine Menge Anhydrit beobachtet werden. Bei solch geringer Alterationstemperatur wurde in verschiedenen Tiefen des Basalt Kerns eine vermehrte Ausfällung von Fe-reichen Phasen, wie Hämatit und Magnetit beobachtet. Die Vernderung der Eisen Mineralogie mit der Tiefe zeigt ein weiteres Mal die wichtige Rolle von Sauerstoff und Porosität in hydrothermalen Systemen, vorallem in Bezug auf Transport von Metallen und Ausfllung von Schwefel-basierten Mineralen.

## Samenvatting

De circulatie van hydrothermale vloeistoffen in de oceanische lithosfeer draagt bij aan massa- en energietransport tussen de lithosfeer en hydrosfeer. Door de hoge porositeit van de bovenste lagen van de korst infiltreert zeewater, dat op grotere diepte verhit en gereduceerd wordt, waarna het metalen opneemt uit het omliggende gesteente. De resulterende metaalrijke oplossing is heet ($\sim$350°C) en stijgt vanwege zijn geringe dichtheid terug naar het oppervlak. Daar vermengt hij met zeewater of daarvan afgeleide vloeistoffen die de pH, temperatuur en het zuurstofgehalte sterk veranderen. Dit leidt tot de neerslag van sulfiden. De invloed van beide vloeistoftypen is vooral goed zichtbaar in de schoorsteenvormige sulfaat-complexen die zich direct boven het punt vormen waar het warme water uit de bodem komt. Deze fenomenen, ook wel 'black smokers' genoemd, hebben vaak een

kern van sulfiden die groeien in de porieruimte die ontstaat tijdens heroplossing van sulfaat op het moment dat meer gereduceerd water wordt aangevoerd vanuit de diepte. Om het begin van de omzettingsreactie tussen sulfide en sulfaat te bestuderen hebben we een anhydrietfragment uit het Pacmanus-bekken met een elektronenmicroscoop en transmissie-elektronenmicroscoop geanalyseerd en is er een 3D-analyse van de poriën gemaakt met een FIB-SEM (Focused Ion Beam - Scanning Electron Microscope). Sulfiden bevonden zich in porieruimtes, zowel in de splijtvlakken van anhydrietkristallen als ook op de kristalgrenzen. Op die grenzen waren opeenhopingen van sulfiden te zien met een chaotische textuur: pyriet werd omgeven door colloforme chalcopyriet (indicatie voor een temperatuurstijging) en daaromheen bevond zich pyriet en sfaleriet (wat wijst op een daling in temperatuur). De groei van sulfiden in oplossingsvlakken en de porievulling met mineralen bij verschillende temperaturen bevestigen de hypothese dat porositeit een doorslaggevende rol speelt bij de mineraalvorming en bij de algehele voortgang van de reactie in de black smokers.

In de oceanische lithosfeer is deze omzetting door sulfiden extensiever, wat zelfs kan leiden tot de vorming van massieve ertsafzettingen. Zulke ertsen komen bij divergente plaatgrenzen voor, zowel bij hoge als bij lage spreidingssnelheden. Sulfiden zijn echter niet bij elke spreidingszone aanwezig. Tijdens batch experimenten hebben we verschillende gesteentetypen uit de oceanische lithosfeer (olivijn, troctoliet, basalt en serpentiniet) in contact gebracht met een synthetische hydrothermale vloeistof met een hoog $H_2S$-gehalte. Hiermee werd aangetoond dat het grootste potentieel voor groei van sulfiden bestaat bij minder reducerende omstandigheden, hier gerepresenteerd door de basalt. De andere lithologieën zijn rijker in olivijn en vormden magnetiet. Dit wijst erop dat de activiteit van zwavel in deze systemen te laag was om sulfiden zoals pyrrhotiet of pyriet te vormen. De grootste ertsafzettingen zijn dus in basaltische hydrothermale systemen te verwachten.

De bovenste lagen van de korst zijn geoxideerd, waardoor het sulfaatmineraal anhydriet kan worden gevormd. Dit mineraal heeft een omgekeerde oplosbaarheid, wat betekent dat het neerslaat bij verhitting van het systeem en oplost tijdens afkoeling. Black smokers kunnen daardoor instorten gedurende een periode van hydrothermale inactiviteit. In de korst zorgt deze oplosbaarheid voor sterke veranderingen in de permeabiliteit van het gesteente. In onze percolatie-experimenten wordt aangetoond dat de groei van anhydriet in basalt bij temperaturen onder de 150°C langzaam verloopt. Slechts bij temperaturen hoger dan 120°C werd anhydriet gevonden. Daarnaast bevatten de monsters bij deze relatief lage temperaturen veel ijzerhoudende mineralen zoals hematiet en magnetiet. De verschillen tussen de aanwezige vormen van ijzer op diverse diepten tonen opnieuw

V

aan hoe belangrijk porositeit is in hydrothermale systemen, zowel voor metaaltransport als voor de vorming van sulfiden.

# Contents

# 1 Introduction

Over 60% of the Earth's surface consists of ocean floor, a geological unit crucial in our understanding of the mantle and of global heat and mass fluxes. Oceanic crust is formed at spreading ridges where tectonic plates diverge. At high spreading rates, the gap between the plates is filled by upwelling magma, formed upon decompression of the underlying asthenosphere (McKenzie 1967). The newly crystallized lithosphere consists of three subsections: basaltic pillow lavas at the top, sheeted dikes as magma feeding channels below it and layered cumulate gabbros at the bottom. The sections still contain a lot of heat when they move away from the ridge, and when seawater penetrates through the more permeable top level of the crust it is heated and rises back up due to buoyancy, creating hydrothermal convection cells. The first outflow of a hydrothermal fluid in the ocean was discovered in 1977 (Corliss et al. 1979) at the Galapagos Spreading Center. After this, more and more venting systems were detected, including some at slow (magma-deprived) spreading ridges where faults exhume lithospheric mantle peridotite material and reaction with seawater takes place. Estimates are that only 1/3 of all hydrothermal systems are discovered so far (Beaulieu et al. 2015).

Interaction of the hot fluid with surrounding rocks causes mineral alteration and leaches metals and other elements from the (ultra)mafic source rocks. These elements are transported in the fluid. During upflow and changing environmental conditions metals can precipitate as sulphide minerals (pyrite: $FeS_2$, chalcopyrite: $CuS_2$, sphalerite: $ZnS$) close to the surface. This process may lead to the formation of massive sulphide deposits (Hannington et al. 1995). Their evolution strongly depends on rock porosity and permeability, source rock composition, fluid salinity, pH, temperature and redox state. The replacive formation of hydrothermal sulphur phases within the oceanic lithosphere is the central topic of this thesis. In the next sections I will give an overview of the current knowledge and conceptual models on the formation of hydrothermal systems and development of ore deposits in them, including fluid-mineral reactions, rock porosity and the role of sulphur and oxygen. Additionally I will discuss the three ways in which this information is obtained: through the study of natural samples, through experiments and through thermodynamic models.

## 1.1 Formation of hydrothermal systems at the seafloor

A hydrothermal system can be divided in three stages (Alt 1995): (1) recharge, with infiltration resulting in leaching of material; (2) reaction and transport, including fluid percolation and physical movement of dissolved elements; and (3) discharge, where upward flow and changing conditions of the fluid-rock system allow precipitation of sulphides (see fig. 1.1) .
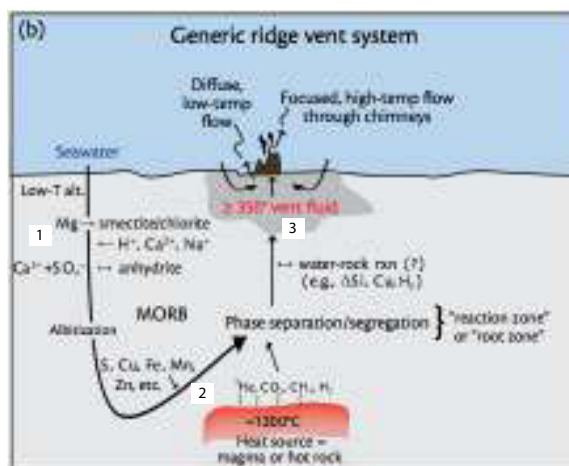


Figure 1.1: Overview of hydrothermal circulation in the oceanic crust by Tivey (2007), with added numbers to correspond to the different stages. Seawater recharge causes low temperature alteration away from the ridge. Further percolation leads to metal leaching from the host rock and upon upflow; these are precipitated in the sub-seafloor and in chimneys.

### 1.1.1 Recharge zone

In the shallow volcanic section, high permeability results in rapid infiltration of seawater, which will heat up at depth. This relatively open system oxidizes basalt and starts fluid-rock chemical exchange, taking up alkalis from the fluid to form zeolites, micas and clays out of primary minerals (Alt 1995). The uptake of part of the seawater $Mg^{2+}$ ion is balanced by $Ca^{2+}$ release from the rock (Mottl and Holland 1978). Fluid-rock experiments performed by Seyfried and Bischoff (1979) show that at 70°C almost no alteration occurred but many cations were leached from the rock, while at 150°C Fe-rich smectite is the main secondary phase. This reaction releases Ca, Na and Si to the fluid. Once fluid temperatures exceed 150°C anhydrite forms spontaneously and uses the released Ca, depriving the seawater of most of its sulphate. This mineral often occurs in veins and

its retrograde solubility can explain the fact that little anhydrite is found in older, cooled crust or at inactive hydrothermal systems.

Low ($<150°$C) temperature alteration in peridotites is reported to result in serpentinites with high sulphate content through sulphide oxidation and in iron oxyhydroxides and carbonates (Alt et al. 2007). Low temperatures also stimulate microbial seawater sulphate reduction.

### 1.1.2  Fluid rock interaction: reaction zone

At greater depths, where permeability is low, the system will be disconnected from surface fluids (Mottl 1983) and it becomes reducing. More Mg is lost due to ionic exchange reactions (Bischoff and Dickson 1975) replacing protons and cations such as $Na^+$ and $K^+$, which are released into the fluid. Dissolved Si increases while pH goes down. pH increases again when all Mg is consumed and silicate hydrolysis-reactions take over; quartz may precipitate from this solution. Around 200-250°C chlorite appears as the main new Mg-rich phase (Kristmannsdóttir 1979). Fluid metal contents increase to up to 3 times their initial concentration (Bischoff and Dickson 1975) due to higher complex stability at low pH and increased salinity (Seewald and Seyfried 1990). At these temperatures, conditions are reducing enough to form sulphide out of sulphate (Shanks et al. 1981) thus increasing sulphide content in the fluid; addition of magmatic sulphur is also possible (Kadko et al. 1995). Continued heating to up to 350°C will result in the dissolution of primary sulphides and in the formation of epidote and calcic plagioclase in the lower sheeted dikes and upper gabbros (Seyfried et al. 1991). Actinolite and tremolite are also reported in these sections (Humphris and Thompson 1978).

Seawater interaction with ultramafic rocks shows a similar fluid evolution trend (Palandri and Reed 2004; Seyfried et al. 2007) and involves hydration of olivine to form serpentine. A striking difference with basalt-hosted systems is the additional release of $H_2$-gas (Douville et al. 2002) related to ferrous iron oxidation (Klein et al. 2009). Sulphide minerals become unstable and dissolve, which might result in a later sulphidation event (Marques et al. 2007). However, high [34]S-isotopic signatures (Delacour et al. 2008) compared to the lower magmatic signature observed in gabbro-hosted systems (Alt et al. 2013) imply that sulphur is mainly added to the system through seawater reduction. Especially during shallow circulation at low temperature serpentinization sites, microbial sulphate reduction should not be ruled out (Alt et al. 2007; Schwarzenbach et al. 2012).

3

### 1.1.3 Fluid transport

The resulting reactive solutions are thus enriched in Cl, S and Si, they have a low pH and oxygen content and high alkalinity, and can reach temperatures up to 400°C. This makes them very suitable for dissolving and transporting large amounts of metals as the stability of Cl⁻, HS⁻ and OH⁻ metal-ligand complexes increases at temperatures above 300°C (Seward 1981). As long as these physical parameters do not change, the fluid can continue to transport metals and make a concentrated solution. Higher water-to-rock ratios (w/r) allow for more metal transport (Seyfried and Bischoff 1977).

Another key to transport is the available fluid pathway. Flow can be pervasive, passing through pores and grain boundaries affecting the whole rock, or channeled, circulating along faults and zones of permeable rock (see example from Escartín et al. 2015). Upflow is often localized in fissures related to seafloor rifting, but on smaller scales, rock permeability determines the exact vent site (Hannington et al. 1995). The more focused a flow, the more concentrated a possible deposit will be. Fluid flow is driven by gradients; in the crust these are often spatial temperature and pressure changes. At shallower levels and in chimneys above discharging vents, the available pathway also relates the rate of transport to the steepness of chemical gradients within a zone (Tivey and McDuff 1990), which has implications for mineral reactions. Zhu et al. (2007) have analysed the evolution of porosity in hydrothermal chimneys over time, finding that angular sulphides effectively blocked all flow while amorphous silica only narrowed pores, decreasing flow and effectively cooling (allowing for more Si to precipitate, cooling further, etc.). Such self-enhancing processes are not uncommon above discharging vent fluids.

### 1.1.4 Discharge and precipitation

Upon reaching 350°C, the buoyancy of the hydrothermal fluid allows it to rise back up to the surface through pores and fractures. Renewed contact with basalt shows another increase in dissolved metals (Seyfried et al. 1991). Metal-ligand complexes become unstable during mixing with seawater or phase separation (by magmatic volatile addition or rapid decompression) due to concomitant changes in temperature, pH, redox state and concentrations of Cl and S (see Gallinatti 1984). This instability can occur both in the host rock and upon exit; the former results in stockwork mineralization, the latter in chimney formation.

Within the crust, reactions with wall rock can cause a change in pH, which alters chlorine-complex stability and allows dropout of metals such as Zn (forming sphalerite). The fluid-rock reactions can additionally increase oxygen fugacity, which destabilizes S-complexes and mainly affects Au, Pb, Zn or Cu (Seward and Barnes 1997). Temperature changes also affect HS⁻-complex stability, resulting in the formation of Cu, Fe and Zn sulphides with decreasing temperature (Seewald and Seyfried 1990). These sulphide minerals precipitate in available pore space (Seewald and Seyfried 1990; Doyle and Allen 2003) or replace the host rock if there is no space to form, but their actual onset of growth is relatively unknown. This process is seen as the beginning of a massive sulphide deposit (Rona et al. 1993; Humphris et al. 1995; Hannington et al. 1998). Rising reactive fluid can result in a pipe of highly altered material underlying the deposit, where the uptake of Mg, Fe and K is often manifested as a chlorite-rich silicified zone; in obducted seafloor sections (called ophiolites) epidosites are assumed to have played this role (example Troodos ophiolite: Bickle and Teagle 1992; Semail ophiolite: Gilgen et al. 2016). Epidote veins display increased porosity, which allow for rapid and focused upflow. Close to the seafloor, environmental conditions change due to mixing with seawater and sulphides can precipitate, both deeper in the upflow zone and close to the surface. This so called 'stockwork zone' has the highest potential for massive sulphides and has been investigated by many (e.g. Humphris et al. 1995; Hannington et al. 1998; Adamides 2010; and others).

Upon exiting the seafloor, hydrothermal black smoker fluids still carry large amounts of dissolved ions and sulphide particles. The particles may stay in suspension to be deposited as Fe-Mn oxyhydroxides around the point of discharge. Mixing of the output fluid with seawater results in the precipitation of sulphate chimneys. The chimney conduits are often lined with sulphide minerals, as they are shielded from direct contact with seawater, and high temperatures and reducing conditions remain (Haymon 1983). Large temperature gradients are the most important for this type of sulphide mineralization, decreasing Cl⁻-complex stability. When outflow ceases, temperatures go down and seawater can infiltrate the crust, forming more sulphides and sulphates at depth. At this point anhydrite chimneys can dissolve and their sulphide content can accumulate as a breccia (Humphris et al. 1995). Less focused upflow of hydrothermal fluids results in white smokers and much smaller amounts of sulphides (Mills and Elderfield 1995).

Additional factors that may affect sulphide mineralization include adsorption to pre-existing mineral faces or bio-mediated crystallization.

## 1.2 Approaches to study sub-seafloor systems

### 1.2.1 Natural samples

One of the most studied hydrothermal sulphide deposits at an oceanic spreading center is the Trans-Atlantic Geotraverse (TAG) mound at 26°08′N and 3670 m depth on the Mid-Atlantic Ridge. Hydrothermal flow seems bound to faults (Kleinrock and Humphris 1996; Tivey et al. 2003; de-Martin et al. 2007). Several holes were drilled in this mound (ODP leg 158). Interpretations of its shape and tonnage come from extrapolation and connectivity of lithologies recognized in these cores. At TAG, sulphur is precipitated in a pyrite-rich stockwork zone, in anhydrite veins and in sulphate chimneys (Humphris et al. 1995). Since these are the three main occurrences of sulphur in the altered oceanic crust, and the topics of the three manuscripts in this thesis, I will describe this particular deposit in more detail to connect the different forms of sulphur-bearing minerals spatially.

The ODP-expedition at TAG in 1994 provided a lot of material to reconstruct the inner structure of a massive sulphide deposit (fig. 1.2). A nice overview is given by Hannington et al. (1998). Anhydrite chimneys discharged black and white smoker fluids (Mills and Elderfield 1995). Pyrite breccias in the sub-surface represent dropped-out sulphides from dissolved chimneys (Humphris et al. 1995). These pyrite fragments were cemented with anhydrite and, at greater depth, silica. Anhydrite veins crosscut the whole section. At greater depth, pyrite disappears (Foukoustos and Seyfried 2005) and only altered wall rock is present, at first showing silicification, but becoming chloritized deeper in the basaltic core. Calculations using tonnage of metals such as Fe, Cu and Zn and heat fluxes estimate that the whole deposit formed rapidly, taking hundreds to thousands of years of flow (Humphris and Cann 2000). Hydrothermal activity here was pulsed (Lalou et al. 1990), as is shown by rock textures (Brown and Clay 1998) and anhydrite REE signatures in the upflow zone (Humphris 1998; Humphris and Bach 2005). This suggests that the large deposit formed during several episodes of sulphidation. Pulsed hydrothermal activity can be explained by either of three phenomena: episodical heat subtraction, the presence of a transient magmatic heat supply explained by short diking events (Humphris and Cann 2000), or the existence of an episodic magma chamber (Mottl 1983).

Hannington et al. (1998) compared this locality to Cu-deposits found in an ophiolite section in Cyprus. This Troodos ophiolite showed very similar structures to the drill cores recovered from
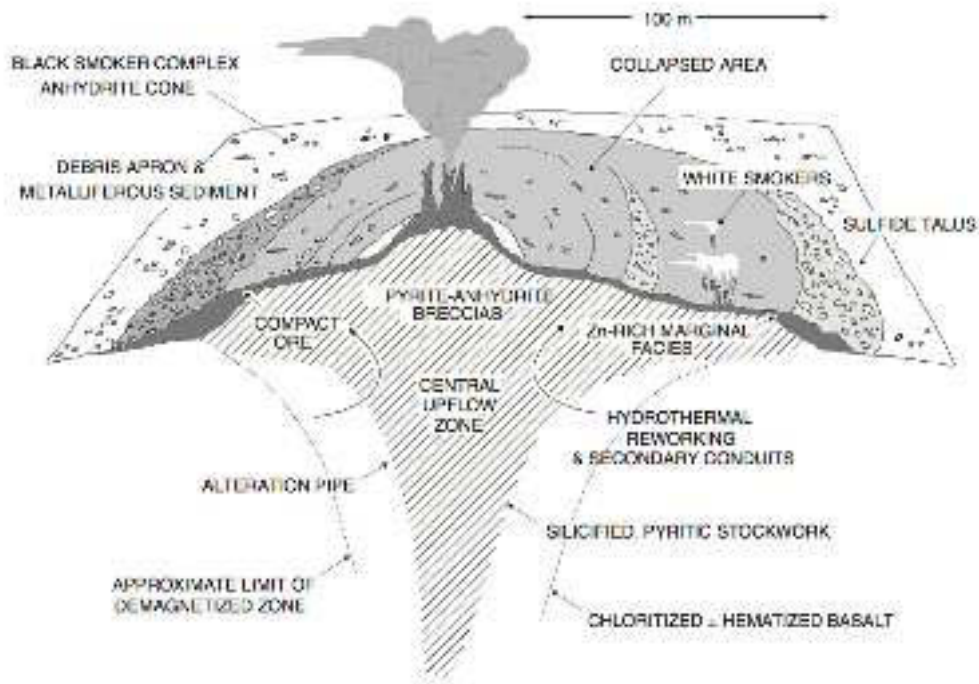
Figure 1.2: Internal structure of the TAG hydrothermal mound with different alteration zones by Hannington et al. (1998).

TAG, both in the altered wall rock signature and in the sulphide mineralization type, trace element distribution and size of the deposit (Humphris and Cann 2000). Both also display the influx of reduced seawater as a source of sulphide (Troodos: Alt 1994; TAG: Herzig et al. 1998). A striking difference is the presence of epidosites at Troodos, as the deeper lying feeder dikes became hydrothermally altered (Bickle and Teagle 1992).

Other examples of massive sulphides can be found in ultramafic rocks, exposed at very slow spreading ridges. At these sites with low magma production spreading is accommodated by low-angle detachment faults, which pull apart the oceanic lithosphere (see images of Escartín and Canales 2011; Petersen et al. 2009). This brings deeper sections to the surface where they interact with seawater that can infiltrate. Seawater can reach temperatures $<150°C$ from residual heat in the rock; in these settings no heat is added by an underlying magma source. Some examples of such ultramafic-hosted sulphide deposits are Rainbow (Marques et al. 2007; Seyfried et al. 2011), Atlantis Massif (Delacour et al. 2008) and MARK (Alt and Shanks 2003).

### 1.2.2 Experimental studies

Many authors have tried to shed light on the interaction of basalt and seawater using batch experiments. All agree on the uptake of Mg and sulphate by the rock and simultaneous release of protons and Si (Bischoff and Dickson 1975) as well as Ca (Mottl and Holland 1978; Seyfried and Bischoff 1981). In an overview of experimental studies at 500 bars (Mottl 1983) compiled data shows that the speed of Mg-uptake is strongly temperature-dependent (fig. 1.3): at 70°C, no reaction occurs while at 150°C uptake is slow (Seyfried and Bischoff 1979) and results in smectite; at 300°C it is very rapid. In a 200°C experiment (Bischoff and Dickson 1975) major fluid chemistry as well as dissolved metal content complied with values for the Reykjanes hydrothermal system; montmorillonite and anhydrite were the main alteration phases, consistent with the observed mineralogy in this system (Tómasson and Kristmannsdóttir 1972). Experiments at 300°C with a w/r of 10 (Seyfried and Bischoff 1981) showed that Mg-proton exchange occurring with seawater was crucial for metal complexation in the fluid, as this did not occur in the same run with a NaCl-bearing fluid. Higher temperatures also facilitate higher metal transport (Seewald and Seyfried 1990).
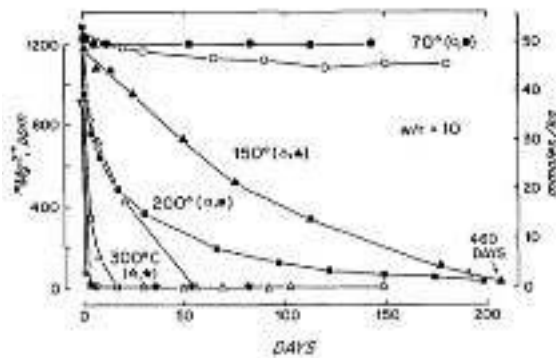


Figure 1.3: Compilation of Mg-concentration in experimental fluids during reactions with basalt (closed circles) at different temperatures; from Mottl (1983).

Besides temperature, water-rock ratio was tested thoroughly. Under seawater-dominated conditions (w/r of >50-100), even more metals were leached out and smectite-chlorite, anhydrite and hematite were reported (Seyfried and Mottl 1982). The excess of Mg added by this amount of seawater could not be taken up by the rock, which means that proton release was maximal and pH stayed low; at much lower w/r ratios (1-3) all Mg uptake was balanced by Ca-release from the rock (Mottl and Holland 1978). The resulting output fluids again closely resembled those recovered

from the Reykjanes hydrothermal field. Observed mineralogy included anhydrite and smectite, and at temperatures >400°C, amphiboles and talc were reported.

Although fluid chemistry is reproduced quite well during these experiments, major differences with natural samples occur in mineralogy in the greenschist facies. Chlorite and epidote are reported in nature (Tómasson and Kristmannsdóttir 1972; Humphris and Thompson 1978) while experiments mainly show smectite-chlorite intergrowth and some amphiboles above 400°C. Due to short run times in comparison to the geological processes taking place, experiments fail to produce chlorite and epidote because formation kinetics are sluggish. Another discrepancy between experiments and natural samples involves iron; Fe-redistribution takes place on a short distance in batch experiments, being captured in smectite-chlorite while in nature it may be transported and precipitated elsewhere as pyrite or magnetite (Mottl 1983). Indeed, pyrite is found in experiments but only at low w/r (<6; Mottl et al. 1979) because at higher ratios the system is too oxidizing to reduce sulphate to sulphide; instead, hematite will be expected.

### 1.2.3   Thermodynamic modelling

To predict the phase relations in a certain chemical system at a given PT, we need thermodynamic models. Examples of such models used for this thesis are EQ3/6 (Wolery and Jarek 2003) and Geochemist′s Workbench (Bethke 1996). As models use the standard molal thermodynamic properties of all available species (solids, aqueous species, gases) we need a database containing these properties. Such a thermodynamic database needs to be internally consistent and take into account mass balance, charge balance and equilibrium calculations. A commonly used program to get these values is SUPCRT92 (Johnson et al. 1992). After defining a reaction in SUPCRT92, an output file will be created that includes the Gibbs free energy, enthalpy of formation, entropy, volume and heat capacity. To understand what they mean and why they matter I will give a short summary of these properties.

Reactions in chemical systems depend on the chemical energy stored in the beginning and ending state of the system. The most stable state of a system is that with the lowest amount of energy, here called Gibbs free energy, G. This energy is defined as

$$G = U - TS + PV \tag{1}$$

where U is internal energy, T is temperature, S is entropy, P is pressure and V is volume. In the equations below I will consider the simple case of an isobaric process, keeping pressure as a constant. In a reaction, the change in Gibbs energy $\Delta_r G$ refers to $G_{product}$-$G_{reactant}$. If this is negative, the reactant has a higher energy level than the product and the reaction proceeds.

Total internal energy U cannot be measured for a single phase, but its change between two phases can be recorded. This change in U depends on two terms: the change in entropy S (state of 'disorder') and the change in other work V (see equation 2).

$$\Delta U = T\Delta S - P\Delta V \tag{2}$$

This is called the Fundamental Equation of thermodynamics. In a mixing reaction, entropy in the system will increase.

Another important source of energy is heat. The change in heat $\Delta H$ during a reaction is called enthalpy and is defined as

$$\Delta H = \Delta U + P\Delta V \tag{3}$$

During the formation of a phase, so called formation enthalpy $\Delta_f H°$ is defined by the enthalpy sum of all species involved. In a reaction between phases, the relative change in enthalpy can be given by subtracting the respective enthalpies of formation. This determines if a process is endogenic (consumes heat, $\Delta_r H > 0$) or exogenic (produces heat, $\Delta_r H < 0$).

A material property directly related to enthalpy is heat capacity $C_P$ (at constant pressure), which can now be defined as follows:

$$C_P = dH/dT_P \tag{4}$$

or, at standard state,

$$\Delta C°_P = (d\Delta H°/dT)_P \tag{5}$$

This shows the amount of heat released or absorbed over an interval in temperature. A standard state is often used (25°C and 1 bar) to measure these values; from this, the other properties can be calculated (Helgeson et al. 1978) and extrapolation to higher pressures and temperatures is

10

possible. Heat capacity for example is temperature sensitive; Maier and Kelley (1932) wrote down heat capacity as a function of temperature as

$$C_{\mathrm{P}} = a + bT - cT^{-2} \tag{6}$$

The parameters a, b and c differ for each phase. Another equation to calculate temperature dependence is the Berman-Brown equation, which is slightly different and uses other coefficients.

Through extensive work by pioneers in this area of geochemistry many equations of state for aqueous species are now known (Helgeson et al. 1981; Tanger and Helgeson 1988; Shock et al. 1989; Sverjensky et al. 1997), which makes it possible to predict their behaviour at elevated pressures and temperatures.

The last important thermodynamic property is entropy S. Entropy, or the state of disorder in a system, will increase during reactions. It depends on heat capacity of the material as

$$\Delta S = (C_{\mathrm{P}}/T)\Delta T \tag{7}$$

Seeing all these properties, the changes in Gibbs energy during a reaction can thus be rewritten in an enthalpy term (recall this is $\Delta H = \Delta U + P\Delta V$) that considers work and heat as causes of energy change, and an entropy term that accounts for mixing; the balance between those two determines whether the reaction will occur. The Gibbs-Duhem equation extends this by including a term for chemical work, written down as chemical potential $\mu$ (potential energy per mole) of a dissolved substance present; this extra term is the sum of the potentials of all present species. Remember that the Gibbs energy will always decrease during spontaneous reactions, trying to reach the lowest free energy point possible for the system.

**Equilibrium reactions**    Many thermodynamic models however do not show the Gibbs energy as output of a reaction but the more practically applicable mineral saturation. Instead of calculating the change in Gibbs energy of a reaction, the equilibrium constant is used to show the direction of reactions. For this, they compare the activity of reactant and product phases. This is especially useful for aqueous species, as their concentration, and thus their Gibbs energy, changes constantly during reaction. This can lead to a reaction not going to completion but establishing an equilibrium where $\Delta_r$G, or total chemical potential of the reaction $\Delta_r\mu=0$.

11

In a reaction $a\mathrm{A}+b\mathrm{B}=c\mathrm{C}$ the equilibrium is thus reached when

$$\Delta_\mathrm{r}\mu = c\mu_\mathrm{C} - b\mu_\mathrm{B} - a\mu_\mathrm{A} = 0 \tag{8}$$

In this reaction, $a,b,c$ are stoichiometry parameters of the reaction. Each of these potentials can be written with a dependence on a standard potential $\mu^\circ_x$ (at standard state) and the activity of each phase:

$$\mu_\mathrm{x} = \mu^\circ_\mathrm{x} + RT ln a_\mathrm{x} \tag{9}$$

where R is the gas constant and $a_x$ is the activity of species X, which depends on the concentration of the species in solution. The calculation of activity from concentration for ionic species is described by the activity coefficient calculated by the Debye-Hückel equation. So at equilibrium, $\mu_x=0$ and $\mu^\circ_x=$-RT $\ln a_x$. In reactions involving many species, the term $a_x$ is replaced by a factor involving all activities. For the reaction $a\mathrm{A}+b\mathrm{B}=c\mathrm{C}$ this factor places product activities in the numerator and the reactant activities in the denominator as $(a_C{}^\mathrm{c}/\ a_A{}^\mathrm{a}\ a_B{}^\mathrm{b})$. At equilibrium, this activity product ratio is called K, the equilibrium constant, and it denotes the ratio of product and reactant activities at equilibrium at this given pressure and temperature. Large values of K will show reactions going close to completion; low values show hardly any reaction will occur (reactants are more stable than products).

It can be given by

$$K = e^{(\text{-}\Delta_\mathrm{r}\mathrm{G}^\circ/\mathrm{RT})} \tag{10}$$

or

$$logK = (-\Delta_\mathrm{r}G^\circ/2.30259RT) \tag{11}$$

where $\Delta_r\mathrm{G}^\circ$ is the change in Gibbs free energy during the reaction calculated from the Gibbs free energies at standard state for all phases taking part. K can also be written as a function of activities of components in the system:

$$K = (a_\mathrm{C}{}^\mathrm{c}/a_\mathrm{A}{}^\mathrm{a}a_\mathrm{B}{}^\mathrm{b}) \tag{12}$$

12

Bear in mind that $a,b,c$ denoted the reaction stoichiometry; activity is 1 for phases in their reference state (i.e., solids, pure water).

Instead of the equilibrium constant, most models show mineral saturation. This can be calculated by using K, as the saturation index (SI) represents the relation between the total ion activity product IAP and the activity of these ions at equilibrium, K. The IAP thus takes into account the ion in all its present forms. The saturation index is given as SI=IAP/K, meaning that when the present ion activity product is larger than the equilibrium one, SI>1 and precipitation occurs. The opposite case is that dissolution occurs at SI<1. At IAP=K and thus SI=1, the mineral is at equilibrium with the solution.

A good example of the use of chemical models is the prediction of both hydrogen generation and secondary mineralogy during serpentinization (Klein et al. 2013). Using the EQ3/6 software, they reacted different ultramafic protoliths with seawater and reported the stable product mineral phases including serpentine, brucite, magnetite and occasionally talc. They did however suppress the metastable serpentine antigorite, which is predicted in models but not observed. This stresses again the overlooked role of kinetics in models such as EQ3/6. Although high w/r ratio experiments at 350°C (Shanks et al. 1981) indeed led to the rapid olivine hydration that could be predicted by thermodynamic models, other experiments at 200°C and low w/r ratio (Seyfried et al. 2007) showed much less reaction than expected. Allen and Seyfried (2003) also noticed sluggish reaction of olivine upon reaction with Cl-bearing fluids at 400°C. These examples underline that thermodynamic models are a tool that should be used with caution.

**Kinetics** Some models can also take into account mineral dissolution kinetics. It therefore combines the geochemistry with time. Reaction rates are calculated using the formula

$$r_k = A_S k_+ (1 - Q/K) \tag{13}$$

where $r_k$ is the reaction rate, $A_S$ is the reactive surface area, $k_+$ is the rate constant and Q and K denote the activity product and equilibrium constant of the reaction. The rate constant can be calculated using the Arrhenius equation: $k_+ = A\ e^{(-E_A/RT_K)}$ where R is the gas constant, A is the pre-exponential factor, $T_K$ is the temperature in Kelvin and $E_A$ is the activation energy necessary for the reaction to take place. These dissolution rates can be used to put a time estimate on reactions in a system.

## 1.3 Motivation

Many conceptual models exist for the formation of hydrothermal cells in oceanic lithosphere and their effects on wall rock, with implications for crustal evolution. The important role of hydrothermalism in transport of heat and matter is especially visible in the leaching of metals and subsequent deposition as sulphide minerals at sudden oxidation or cooling of the system. The onset of sulphide formation is therefore related to both fluid composition and rock porosity. Although many seafloor hydrothermal systems have been analysed for fluid compositions, mineral assemblages and tectonic settings, the coupling between fluid-rock interaction and evolving porosity has remained relatively unstudied. This relation between alteration and the development of a connected pore network is crucial to the progress of fluid-mediated reactions. The first step in the formation of sulphide minerals is therefore key to the further development of larger sulphide deposits.

The onset of sulphide formation is not an easy process to analyse as it occurs deep in the crust, often obscured from view and heavily under-sampled. Drill cores from seamounts can provide information on sulphide formation and crustal porosity. Chimneys growing above discharging vents are often lined with small sulphide crystals in their conduits and can also shed light on the onset of sulphide formation in reducing systems.

This thesis focuses on the role of sulphur-bearing minerals in the oceanic lithosphere. It aims to unravel the formation of single sulphide crystals and porosity in related rocks. For the first chapter, I have investigated the natural occurrence of sulphide minerals within a chimney fragment, where the highly reducing hydrothermal fluid is expected to corrode the chimney and allow for sulphide mineralization. Chemical and textural analyses confirm that early stage sulphide formation is related to changes in porosity of the chimney.

The largest part of replacive sulphide deposits however is present in the sub-seafloor. Many reports of natural samples and experimental studies documenting seawater-rock interaction exist, while the reaction with vent fluids has gotten much less attention. Therefore, an experimental study on wall-rock sulphidation through hydrothermal fluids was carried out to investigate the potential of different rock types hosting venting systems to form an actual deposit. This was compared to the thermodynamic stability of the observed minerals calculated from models. Results on fluid composition and product mineralogy are presented in the second part of this thesis.

The influence of sulphur in the oceanic crust is not limited to the on-axis formation of sulphide deposits. Sulphate minerals such as anhydrite and barite are also present, either as chimneys above

discharging hydrothermal vents, or as veins (anhydrite) upon heating of infiltrated seawater or mixing with hydrothermal fluids. This last process takes place both at the discharge and the recharge zone. Veining shows the importance of anhydrite for the evolution of crustal porosity; the retrograde solubility of this mineral accounts for transient changes in porosity and permeability of the shallow parts of the oceanic crust. Although much is already known about the anhydrite-gypsum equilibrium, the fracture filling growth of anhydrite has not been analysed in detail. Transient anhydrite precipitation affects the permeability of the recharge zone and shallower parts of the discharge zone. The last part of this thesis experimentally investigates the ease of anhydrite precipitation in fractured basalt and mentions the thermodynamic stability of iron-bearing phases in this part of the crust.

## 1.4 Project outline

The work of done for this thesis is summarized in three first-author manuscripts, which are the chapters of the thesis in the order indicated below.

### 1.4.1 Manuscript 1

Title: The role of porosity in the early stages of replacive sulphide formation at hydrothermal vent sites: a case study of massive anhydrite form the Pacmanus hydrothermal field, Papua New Guinea
Authors: Catharina Los, Oliver Plümper, Wolfgang Bach
Submitted to *Contributions to Mineralogy and Petrology* on 25-07-2017

This manuscript looks at the textural relations between anhydrite and sulphide minerals in chimney fragments. Sulphides are detected in circular lines in anhydrite crystals, in its cleavage planes and on grain boundaries. In these last two occurrences sulphides are surrounded by porosity. A FIB-cut through a cleavage plane shows pyrite growth on both sides of the dissolving anhydrite resulting in a hollow crystal, relating its growth directly to anhydrite dissolution. On grain boundaries, complex textural relations between different sulphide phases (pyrite, surrounded by chalcopyrite and sphalerite) show that the fluid has evolved to precipitate minerals under different precipitation conditions, meaning that a connecting pathway existed along which sulphide minerals were deposited.

Author contributions: Catharina Los sampled the anhydrite block, collected the data (except

for the TEM image) and wrote the manuscript (80% of all work). Oliver Plümper assisted with the FIB-SEM analyses and performed the TEM imaging, providing image 5.a (5% of all work). Wolfgang Bach made figure 1 and 9, provided the thermodynamic model used for sulphide stability analysis and contributed to the scientific discussion (15% of all work).

### 1.4.2 Manuscript 2

Title: Sulfidation of major rock types of the oceanic lithosphere; an experimental study at 250°C and 400 bars

Authors: Catharina Los, Wolfgang Bach

Submitted to *Lithos* on 04-09-2017

The manuscript investigates the reactions of crushed olivine, troctolite, basalt and serpentinite with an $H_2S$-rich fluid. Despite the high sulphide content in the fluid, the basalt was the only experiment to form a sulphide phase, pyrite. The other runs showed olivine serpentinization and growth of magnetite, while plagioclase in troctolite reacted to andradite, showing the role of Si-activity. Serpentinite did not react. These experiments show that sulphur activity is more important than absolute amounts of sulphur in a system, and that oxidizing conditions are more favourable to sulphide formation than highly reducing conditions found in olivine-dominated rock.

Author contributions: Catharina Los performed the experiments and sampling, ran the chemical models, made the figures and wrote the manuscript (95% of all work). Wolfgang Bach contributed to the planning of the project and scientific discussion (5% of all work).

### 1.4.3 Manuscript 3

Title: Anhydrite precipitation and iron redistribution in low temperature flow-through experiments representing shallow marine hydrothermal systems

Authors: Catharina Los, Wolf-Achim Kahl, Wolfgang Bach

This manuscript focuses on alteration mineralogy in the seawater recharge zone. Flow-through experiments performed at several temperatures (95-140°C) in a pre-fractured basalt show that anhydrite precipitation is more difficult than previously thought. Low anhydrite abundance between 120-140°C and its absence <120°C show that growth kinetics are low. Fe becomes mobilized and

forms Fe-Mn crust, hematite, magnetite or pyrite depending on depth within the reacting core. This shows the influence of oxidation state of the fluid and w/r ratio, going down with depth. The presence of different iron phases shows that Fe-activity is higher than previously assumed and thermochemical sulphate reduction by Fe takes place, implying that less free ions may be available as energy source for microbial life.

Author contributions: Catharina Los performed the experiments and sampling, ran the chemical models and image processing of scans, made the figures (except for figure 5) and wrote the manuscript (85% of all work). Wolf-Achim Kahl has previously designed the experimental setup, assisted with the scanning and contributed to the scientific discussion (10% of all work). Wolfgang Bach produced figure 5, contributed to the planning of the project and scientific discussion (5% of all work).

## 1.5 References

Adamides N.G., 2010. Mafic-dominated volcanogenic sulphide deposits in the Troodos ophiolite, Cyprus Part 2 –A review of genetic models and guides for exploration. Applied Earth Science 119(4), 193-204.

Allen D.E., Seyfried Jr. W.E., 2003. Compositional controls on vent fluids from ultramafic-hosted hydrothermal systems at mid-ocean ridges: and experimental study at 400°C, 500 bars. Geochimica et Cosmochimica Acta 67(8), 1531-1542

Alt J.C., 1994. A sulfur isotopic profile through the Troodos ophiolite, Cyprus: Primary composition and the effects of seawater hydrothermal alteration. Geochimica et Cosmochimica Acta 58, 1825-1840.

Alt J.C., 1995. Subseafloor Processes in Mid-Ocean Ridge Hydrothermal Systems. In: Humphris S.E., Zierenberg R.A., Mullineaux L.S., Thomson R.E. (eds) Seafloor Hydrothermal Systems: Physical, Chemical, Biological and Geological Interactions. Geophysical Monograph 91, American Geophysical Union 85-114

Alt J.C., Shanks III W.C., 2003. Serpentinization of abyssal peridotites from the MARK area, Mid-Atlantic Ridge: Sulfur geochemistry and reaction modeling. Geochimica et Cosmochimica Acta 64(4), 641-653

Alt J.C., Schwarzenbach E.M., Früh-Green G.L., Shanks III W.C., Bernasconi S.M., Garrido C.J., Crispini L., Gaggero L., Padrón-Navarta J.A., Marchesi C., 2013. The role of serpentinites in

cycling of carbon and sulfur: Seafloor serpentiniation and subduction metamorphism. Lithos 178, 40-54

Alt J.C., Shanks III W.C., Bach W., Paulick H., Garrido C.J., Beaudoin G., 2007. Hydrothermal alteration and microbial sulfate reduction in peridotite and gabbro exposed by detachment faulting at the Mid-Atlantic Ridge, 15°20′N (ODP Leg 209): A sulfur and oxygen isotope study. Geochemistry, Geophysics, Geosystems 8(8), Q08002. http://dx.doi.org/10.1029/2007GC001617

Alt J.C., Zuleger E., Erzinger J., 1994. Mineralogy and stable isotopic compositions of the hydrothermally altered lower sheeted dike complex, Hole 504B, Leg 140. In: Erzinger J., Becker K., Dick H.J.B., Stokking L.B. (eds) Proceedings of the Ocean Drilling Program, Scientific Results 137/140, pp. 155-166

Beaulieu S.E., Baker E.T., German C.R., 2015. Where are the undiscovered hydrothermal vents on oceanic spreading ridges? Deep-Sea Research II 121, 202-212

Bethke C.M., 1996. Geochemical Reaction Modeling. Oxford University Press, New York

Bickle M.J., Teagle D.A.H., 1992. Strontium alteration in the Troodos ophiolite: implications for fluid fluxes and geochemical transport in mid-ocean ridge hydrothermal systems. Earth and Planetary Science Letters 113, 219-237

Bischoff J.L., Dickson F.W., 1975. Seawater-basalt interaction at 200°C and 500 bars: implications for origin of sea-floor heavy-metal deposits and regulation of seawater chemistry. Earth and Planetary Science Letters 25, 385-397

Brown D., McClay K.R., 1998. 15. Data Report: Sulfide textures in the active TAG massive sulfide deposit, 26°N, Mid-Atlantic Ridge. In: Herzig, P.M., Humphris, S.E., Miller, D.J., and Zierenberg, R.A. (eds) Proceedings of the Ocean Drilling Program, Scientific Results Vol. 158, pp. 193-200

Corliss J.B., Dymond J., Godon L.I., Edmond J.M., von Herzen R.P., Ballard R.D., Green K., Williams D., Bainbridge A., Crane K., van Andel T., 1979. Submarine Thermal Springs on the Galápagos Rift. Science 203(4385), 1073-1083

Delacour A., Früh-Green G.L., Bernasconi S.M., Kelley D.S., 2008. Sulfur in peridotites and gabbros at Lost City (30°N, MAR): Implications for hydrothermal alteration and microbial activity during serpentinization. Geochimica et Cosmochimica Acta 72, 5090-5110

deMartin B.J., Sohn R.A., Canales J.P., Humphris S.E., 2007. Kinematics and geometry of active detachment faulting beneath the Trans-Atlantic Geotraverse (TAG) hydrothermal field on the

Mid-Atlantic Ridge. Geology 35(8), 711-714

Douville E., Charlou J.L., Oelkers E.H., Bienvenu P., Jove Colon C.F., Donval J.P., Fouquet Y., Prieur D., Appriou P., 2002. The rainbow vent fluids (36°14′N, MAR): the influence of ultramafic rocks and phase separation on trace metal content in Mid-Atlantic Ridge hydrothermal fluids. Chemical Geology 184, 37-48

Doyle M.G., Allen R.L., 2003. Sub-seafloor replacement in volcanic-hosted massive sulfide deposits. Ore Geology Reviews 23, 183-222

Escartín J., Barreyre T., Cannat M., Garcia R., Gracias N., Deschamps A., Salocchi A., Sarradin P.-M., Ballu V., 2015. Hydrothermal activity along the slow-spreading Lucky Strike ridge segment (Mid-Atlantic Ridge): Distribution, heatflux, and geological controls. Earth and Planetary Science Letters 431, 173-185

Escartín J., Canales P., 2011. Detachments in Oceanic lithosphere: Deformation, Magnetism, Fluid Flow and Ecosystems. Eos Transactions AGU 92(4), 31

Foukoustos D.I., Seyfried Jr. W.E., 2005. Redox and pH constraints in the subseafloor root zone of the TAG hydrothermal system, 26°N Mid-Atlantic Ridge. Earth and Planetary Science Letters 235, 497-510

Gallinatti B.C., 1984. Initiation and collapse of active circulation in a hydrothermal system at the Mid-Atlantic Ridge, 23°N. Journal of Geophysical Research 89(B5), 3275-3289

Gilgen S.A., Diamond L.W., Mercolli I., 2016. Sub-seafloor epidosite alteration: Timing, depth and stratigraphic distribution in the Semail ophiolite, Oman. Lithos 260, 191-210

Hannington M.D., Galley A.G., Herzig P.M., Petersen S., 1998. 28. Comparison of the TAG mound and stockwork complex with Cyprus-type massive sulfide deposits. In: Herzig P.M., Humphris S.E., Miller D.J., Zierenberg R.A. (eds) Proceedings of the Ocean Drilling Program, Scientific Results. Vol. 158, pp. 389-415

Hannington M.D., Jonasson I.R., Herzig P.M., Petersen S., 1995. Physical and Chemical Processes of Seafloor Mineralization at Mid-Ocean Ridges. In: Humphris S.E., Zierenberg R.A., Mullineaux L.S., Thomson R.E. (eds) Seafloor Hydrothermal Systems: Physical, Chemical, Biological and Geological Interactions. Geophysical Monograph 91, American Geophysical Union 115-157

Haymon R.M., 1983. Growth history of hydrothermal black smoker chimneys. Nature 301, 695-698

Helgeson H.C., Delany J.M., Nesbitt H.W., Bird D.K., 1978. Summary and critique of the thermodynamic properties of rock-forming minerals. American Journal of Science 278(A), 229

Helgeson H.C., Kirkham D.H., Flowers G.C., 1981. Theoretical prediction of the thermodynamic behavior of aqueous electrolytes at high pressures and temperatures: IV. Calculation of activity coefficients, osmotic coefficients, and apparent molal and standard and relative partial molal properties to 600°C and 5 kb. American Journal of Science 281(10), 1249-1516

Herzig P.M., Petersen S. and Hannington M.D., 1998. Geochemistry and sulphur-isotopic composition of the TAG hydrothermal mound, Mid-Atlantic Ridge, 26°N. In: Herzig P.M., Humphris S.E., Miller D.J., Zierenberg R.A. (eds) Proceedings of the Ocean Drilling Program, Scientific Results Vol. 158, pp. 47-70

Humphris S.E., 1998. 12. Rare Earth Element Composition of anhydrite: implications for deposition and mobility within the active TAG hydrothermal mound. In: Herzig P.M., Humphris S.E., Miller D.J., Zierenberg R.A. (eds) Proceedings of the Ocean Drilling Program, Scientific Results Vol. 158, pp. 143-159

Humphris S.E., Bach W., 2005. On the Sr isotope and REE compositions of anhydrites from the TAG seafloor hydrothermal system. Geochimica et Cosmochimica Acta 69(6), 1511-1525

Humphris S.E., Cann J.R., 2000. Constraints on the energy and chemical balances of the modern TAG and ancient Cyprus seafloor sulfide deposits. Journal of Geophysical Research 105 (B12), 28.477-28.488

Humphris S.E., Thompson G., 1978. Hydrothermal alteration of oceanic basalts by seawater. Geochimica et Cosmochimica Acta 42, 107-125

Humphris S.E., Herzig P.M., Miller D.J., Alt J.C., Becker K., Brown D., Brügmann G., Chiba H., Fouquet Y., Gemmell J.B., Guerin G., Hannington M.D., Holm N.G., Honnorez J.J., Itturino G.J., Knott R., Ludwig R., Nakamura K., Petersen S., Reysenbach A.-L., Rona P.A., Smith S., Sturz A.A., Tivey M.K., Zhao X, 1995. The internal structure of an active sea-floor massive sulphide deposit. Nature 377, 713-716

Johnson J.W., Oelkers E.H., Helgeson H.C., 1992. Supcrt92: A software package for calculating the standard molal thermodynamic properties of minerals, gases, aqueous species, and reactions from 1 to 5000 bar and 0 to 1000°C. Computers and Geosciences 18(7), 889-947

Kadko D., Baross J., Alt J., 1995. The Magnitude and Global Implications of Hydrothermal Flux. In: Humphris S.E., Zierenberg R.A., Mullineaux L.S., Thomson R.E. (eds) Seafloor Hydrothermal Systems: Physical, Chemical, Biological and Geological Interactions. Geophysical Monograph 91, American Geophysical Union 446-466

Klein F., Bach W., McCollum T.M., 2013. Compositional controls on hydrogen generation during serpentinization. Lithos 178, 55-69

Klein F., Bach W., Jöns N., McCollum T.M., Moskowitz B., Berquó T., 2009. Iron partitioning and hydrogen generation during serpentinization of abyssal peridotites from 15°N on the Mid-Atlantic Ridge. Geochimica et Cosmochimica Acta 73, 6868-6893

Kleinrock M. C., Humphris S. E., 1996. Structural controls on the localization of seafloor hydrothermal activity at the TAG active mound, Mid-Atlantic Ridge. Nature 382, 149-153

Kristmannsdóttir H., 1979. Alteration of basaltic rocks by hydrothermal activity at 100-300°C. In: Mortland M., Farmer V. (eds) Developments in Sedimentology, Vol. 27. Elsevier, Amsterdam, pp. 359-367

Lalou C., Thompson G., Arnold M., Brichet E., Druffel E., Rona P.A., 1990. Geochronology of TAG and Snakepit hydrothermal fields, Mid-Atlantic Ridge: witness to a long and complex hydrothermal history. Earth and Planetary Science Letters 97, 113-128

Libbey R.B., Williams-Jones A.E., 2016. Relating sulfide mineral zonation and trace element chemistry to subsurface processes in the Reykjanes geothermal system, Iceland. Journal of Volcanology and Geothermal Research 310, 225-241

Maier C.G., Kelley K.K., 1932. An equation for the representation of high temperature heat content data. American Chemical Society Journal 54, 3243-3246

Marques A.F.A., Barriga F.J.A.S., Scott S.D., 2007. Sulfide mineralization in an ultramafic-rock hosted seafloor hydrothermal system: From serpentinization to the formation of Cu-Zn-(Co)-rich massive sulfides. Marine Geology 245, 20-39

McKenzie D., 1967. Some remarks on heat flow and gravity anomalies. Journal of Geophysical Research 72, 6261-6273

Mills R.A., Elderfield H., 1995. Rare earth element geochemistry of hydrothermal deposits from the active TAG Mound, 26°N Mid-Atlantic Ridge. Geochimica et Cosmochimica Acta 59(17), 3511-3524

Mottl M.J., 1983. Metabasalts, axial hot springs, and the structure of hydrothermal systems at mid-ocean ridges. Geological Society of America Bulletin 94, 161-180

Mottl M.J., Holland H.D., 1978. Chemical exchange during hydrothermal alteration of basalt by seawater: I. Experimental results for major and minor components of seawater. Geochimica et Cosmochimica Acta 42, 1103-1115

Mottl M.J., Holland H.D., Corr R.S., 1979. Chemical exchange during hydrothermal alteration of basalt by seawater: II. Experimental results for Fe, Mn and sulfur species. Geochimica et Cosmochimica Acta 43, 869-884

Palandri J.L., Reed M.H., 2004. Geochemical models of metasomatism in ultramafic systems: Serpentinization, rodingitization, and sea floor carbonate chimney precipitation. Geochimica et Cosmochimica Acta 68(5), 1115-1133

Rona P.A., Hannington M.D., Raman C.V., Thompson G., Tivey M.K., Humphris S.E., Lalou C., Petersen S., 1993. Active and relict sea-floor hydrothermal mineralization at the TAG Hydrothermal Field, Mid-Atlantic Ridge. Economic Geology 88, 1989-2017

Schwarzenbach E.M., Früh-Green G.L., Bernasconi S.M., Alt J.C., Shanks III W.C., Gaggero L., Crispini L., 2012. Sulfur geochemistry of peridotite-hosted hydrothermal systems: Comparing the Ligurian ophiolites with oceanic serpentinites. Geochimica et Cosmochimica Acta 91, 283-305

Seewald J.S., Seyfried Jr. W.E., 1990. The effect of temperature on metal mobility in subseafloor hydrothermal systems: constraints from basalt alteration experiments. Earth and Planetary Science Letters 101, 388-403

Seward T.M., 1981. Metal complex formation in aqueous solutions at elevated temperatures and pressures. In: Rickard D., Wickman F. (eds) Chemistry and Geochemistry of Solutions at High Temperatures and Pressures. Physics and Chemistry of the Earth 13-14, pp. 113-128

Seward T.M., Barnes H.L., 1997. Metal transport by hydrothermal ore fluids. In: Barnes H.L. (eds) Geochemistry of Hydrothermal Ore Deposits. John Wiley & Sons, pp. 435-486

Seyfried Jr. W.E., Bischoff J.L., 1977. Hydrothermal transport of heavy metals by seawater: the role of seawater basalt ratio. Earth and Planetary Science Letters 34, 71-77

Seyfried Jr. W.E., Bischoff J.L., 1979. Low temperature basalt alteration by seawater: an experimental study at 70°C and 150°C. Geochimica et Cosmochimica Acta 43, 1937-1947

Seyfried Jr. W.E., Bischoff J.L., 1981. Experimental seawater-basalt interaction at 300°C, 500 bars, chemical exchange, secondary mineral formation and implications for the transport of heavy metals. Geochimica et Cosmochimica Acta 45, 135-147

Seyfried Jr. W.E., Mottl M.J., 1982. Hydrothermal alteration of basalt by seawater under seawater-dominated conditions. Geochimica et Cosmochimica Acta 46, 985-1002

Seyfried Jr. E., Ding K., Berndt M.E., 1991. Phase equilibria constrains in the chemistry of hot spring fluids at mid-ocean ridges. Geochimica et Cosmochimica Acta 55, 3559-3580

Seyfried Jr. W.E., Foustoukos D.I., Fu Q., 2007. Redox evolution and mass transfer during serpentinization: An experimental and theoretical study at 200°C, 500 bar with implications for ultramafic-hosted hydrothermal systems at Mid-Ocean Ridges. Geochimica et Cosmochimica Acta 71, 3872-3886

Seyfried Jr. W.E., Pester N.J., Ding K., Rough M., 2011. Vent fluid chemistry of the Rainbow hydrothermal system (36°N, MAR): Phase equilibria and in situ pH controls on subseafloor alteration processes. Geochimica et Cosmochimica Acta 75, 1574-1593

Shanks W.C., Bischoff J.L., Rosenbauer R.J., 1981. Seawater sulfate reduction and sulfur isotope fractionation in basaltic systems: Interaction of seawater with fayalite and magnetite at 200-350°C. Geochimica et Cosmochimica Acta 45, 1977-1995

Shock E.L., Helgeson H.C., Sverjensky D.A., 1989. Calculation of the thermodynamic and transport properties of aqueous species at high pressures and temperatures: standard partial molal properties of inorganic neutral species. Geochimica et Cosmochimica Acta 53(9), 2157-2183

Sverjensky D.A., Shock E.L., Helgeson H.C., 1997. Prediction of the thermodynamic properties of aqueous metal complexes to 1000°C and 5 kb. Geochimica et Cosmochimica Acta 61(7), 1359-1412

Tanger IV J.C., Helgeson H.C., 1988. Calculation of the thermodynamic and transport properties of aqueous species at high pressures and temperatures: revised equations of state for the standard partial molal properties of ions and electrolytes. American Journal of Science 288(1), 19-98

Tivey M.A., Schouten H., Kleinrock M.C., 2003. A near-bottom magnetic survey of the Mid-Atlantic Ridge axis at 26°N: Implications for the tectonic evolution of the TAG segment. Journal of Geophysical Research 108, 2277

Tivey M.K., 2007. Generation of Seafloor Hydrothermal Vent Fluids and Associated Mineral Deposits. Oceanography 20(1), 50-65

Tivey M.K., McDuff R.E., 1990. Mineral Precipitation in the Walls of Black Smoker Chimneys: A Quantitative Model of Transport and Chemical Reaction. Journal of Geophysical Research 95(B8), 12.617-12.637

Tómasson J., Kristmannsdóttir H., 1972. High Temperature Alteration Minerals and Thermal Brines, Reykjanes, Iceland. Contributions to Mineralogy and Petrology 36, 123-134

Wolery T.W., Jarek R.L., 2003. Software User's Manual EQ3/6, Version 8.0, Sandia National Laboratories. Albuquerque, NM, USA

Zhu W., Tivey M.K., Gittings H., Craddock P.R., 2007. Permeability-porosity relationships in

seafloor vent deposits: Dependence on pore evolution processes. Journal of Geophysical Research 112, B05208. doi:10.1029/2006JB004716

# 2 The role of porosity in the early stages of replacive sulphide formation at hydrothermal vent sites: a case study of massive anhydrite from the Pacmanus hydrothermal field, Papua New Guinea

*Catharina Los (1), Oliver Plümper (2), Wolfgang Bach (1,3)*

Contact: los@uni-bremen.de, tel. 0049 421 218 65406

(1) Geosciences Department, University of Bremen, Klagenfurter Str. 2, 28359 Bremen, Germany

(2) Department of Earth Sciences, Utrecht University, Budapestlaan 4, 3584CD Utrecht, the Netherlands

(3) MARUM, Center for Marine and Environmental Sciences, Leobener Str. 28359 Bremen, Germany

## 2.1 Abstract

Hydrothermal circulation through the oceanic crust facilitates mass and heat exchange between the earth′s lithosphere and its oceans. Seawater-rock interaction results in hot, acidic, metal-rich fluids that have ore forming potential. Key to the formation of sub-seafloor ore deposits is the physico-chemical evolution of hydrothermal vent systems starting with sulphate chimney growth. Continuous fluid flow through these chimneys results in the pervasive transformation of sulphate

to sulphide influencing permeability and thus metal mobility. Although the vent fluid geochemistry is well understood the reactive evolution of fluid conduits and thus the sulphate to sulphide replacement mechanism remains largely unknown. Here we investigate sulphide-bearing massive anhydrite ($CaSO_4$) exposed in the active Fenway vent site in the Pacmanus hydrothermal field (Manus Basin, Papua New Guinea). Within the vent system pyrite-chalcopyrite aggregates grew on anhydrite grain boundaries and micro-scale porosity allowed for pyrite growth inside anhydrite cleavage planes. Three-dimensional porosity analysis shows a connected dissolution network along anhydrite grain boundaries. Dissolution was initiated through anhydrite corrosion by infiltrating hydrothermal fluid in agreement with thermodynamic reaction path modelling. Chalcopyrite and sphalerite growth postdate pyrite nucleation, implying that connected pathways remained open during continuous fluid circulation. As sulphide grain size is directly dependent on available pore space we conclude that dissolution and sulphide growth are tightly coupled in space and time. Our study shows that anhydrite dissolution by discharging vent fluids is the main porosity-generating mechanism and key to the sulphate by sulphide replacement in hydrothermal chimneys and upflow zones that can form massive ore deposits.

## 2.2 Introduction

The discovery of large-scale fluid-rock interaction has sparked scientific interest in the role of fluids in metamorphism (models by Helgeson 1969; Carmichael 1969; Yardley 2009; Putnis and Austrheim 2010; Jamtveit and Hammer 2012). The importance of fluids in ore formation has been known for a long time (e.g. Lindgren 1933; Burnham 1967, 1979), acting as a means of mass transport (Barnes 1997; Seward and Barnes 1997) and creating a trap for metals upon changes in chemical conditions due to fluid mixing (Helgeson 1969; Barriga and Fyfe 1988; Barnes 1997b). Although the role of fluids has traditionally only been applied to felsic on-land deposits and skarns (Einaudi et al. 1981; Eugster 1985), large metal accumulates also occur in mafic systems (Mathez 1989), such as at the seafloor or in ophiolites (Humphris et al. 1995; Hannington et al. 1998; Foustoukos and Seyfried 2005 and others). The most common ore mineralization type here is the Volcanogenic Massive Sulphide (VMS) deposit (see Tornos et al. 2015). Active hydrothermal venting in the deep-sea is

only known since the late 1970′s (Corliss et al. 1979) and the role of hydrothermal fluids in formation of VMS deposits has been investigated ever since (Hannington et al. 1991; James and Elderfield 1996; Humphris and Cann 2000 and others) focusing on vent fluid chemistry, energy transport and water-rock reactions. Above discharging vents, sulphate chimneys are initially built upon heating of surrounding seawater, and the sulphates become subsequently replaced by sulphides (Haymon 1983). The first stage of this replacement reaction takes place within the chimney structure and porosity development by this process plays a large role in evolution of fluid pathways (Tivey and McDuff 1990). Ultimately, total replacement by sulphide can result in the development of massive sulphide deposits (Haymon 1983; Humphris et al. 1995).

The changing composition of the seawater-derived fluids is crucial to mineral replacement. Upon percolation through cracks and along grain boundaries in the oceanic crust and heating with depth, magnesium uptake by host rock acidifies these fluids (Bischoff and Dickson 1975) and the reducing conditions result in $H_2S$-production (Shanks et al. 1981; Seewald and Seyfried 1990). This reduction of sulphate peaks at temperatures between 200 and 350°C (Shanks et al. 1981). By continued heating the fluids become buoyant and rise to the surface, while they keep interacting with the surroundings. At the seafloor, the reactive fluids come into contact with cold seawater. The sudden change in temperature, pressure and chemical environment causes sulphate minerals, such as anhydrite and barite, to precipitate (Haymon 1983; Janecky and Seyfried 1984). These chimneys grow bigger over time and the inner part is protected from direct contact with seawater. High temperature conditions prevail in the conduit and the highly corrosive fluids start to dissolve anhydrite and form sulphides. Although sulphate-sulphide zoning of chimneys and bigger hydrothermal deposits is well known (Haymon 1983; Humphris et al. 1995; Revan et al. 2014), and many studies have focused on mineral equilibria and fluid compositions (Janecky et al. 1984; Bischoff and Dickson 1975; Tivey and McDuff 1990; Seyfried and Ding 1995) the evolution of porosity and permeability that is critical for the mineralization to progress (Tivey and McDuff 1990; Zhu et al. 2007) is largely unknown. Moreover, a systematic investigation of the mechanism of replacement reactions with respect to the mineralogical development of a hydrothermal sulphide deposit is lacking.

This contribution focuses on the mineral microstructure and pore space distribution in sulphide-bearing massive anhydrite sampled in the Papua-Australia-Canada-Manus (Pacmanus) hydrothermal area (Manus Basin, Papua New Guinea). Here we investigate a sample of massive sulphide from next to an active black smoker chimney in order to analyse mineral contacts between anhydrite

and sulphide phases. In particular, we focus on the analysis of dissolution-precipitation associated microstructures as well as the spatial and size distribution of pores. Using this information we obtain insight into the role of reaction progress and fluid pathway development on the evolution of a hydrothermal system and the formation of seafloor sulphide deposits.

## 2.3 Geological setting and hydrothermal fluid background at Pacmanus

The Manus basin to the northeast of Papua New Guinea (fig. 2.1a) features several NE-SW oriented spreading ridges, which are formed by oblique back arc extension (Martinez and Taylor 1996). Northward subduction of the Solomon Sea Plate under New Britain caused block rotation of the Bismarck plate, which broke apart to create the Manus microplate. An asymmetric pull-apart basin developed in the easternmost part of the Manus Basin, featuring ridges of basaltic to rhyodacitic volatile-rich material that host hydrothermal activity.

The Pacmanus hydrothermal field is located on the Pual Ridge in the SW of the Manus Basin (fig. 2.1b). The Pual Ridge consists of auto-brecciated flows of felsic lavas (Paulick et al. 2004). The rock compositions show a calc-alkaline differentiation trend (Binns and Scott 1993) and strong island-arc affinity in trace element composition (Sinton et al. 2002; Beier et al. 2015). Pacmanus comprises numerous hydrothermal vent fields, including Fenway and Roman Ruins. The locations of the vents are strongly controlled by upper crustal permeability, which in turn is controlled by the volcanic facies and the occurrence of faults (Paulick et al. 2004; Thal et al. 2014). Some vents are influenced by seawater-rock interactions (Roman Ruins and Fenway), while others are affected by subseafloor entrainment of seawater and magma degassing (Reeves et al. 2011; Craddock et al. 2010).

Kamenetsky et al. (2001) studied melt inclusions in basaltic rocks from the lower reaches of the Pual Ridge to show evidence for magma degassing of metals, which contribute to the metal inventory of the hydrothermal vent fluids. Upon expulsion, the hydrothermal fluids range from 250-360°C with a pH around 2.5-3.5 and high concentrations of $H_2S$, $CO_2$ and $CH_4$. For information on metal and trace element content, the reader is directed to the papers of Reeves et al. (2011) and Craddock et al. (2010), which use these parameters to deduce fluid pH and Cl-content in the Pacmanus field. Measured fluids from the Fenway vent system (Reeves et al. 2011) are provided in the supplementary data, table 1. Every vent has a different REE pattern, which is controlled by fluid pH, temperature and ligand content; all factors are influenced by addition of magmatic volatiles
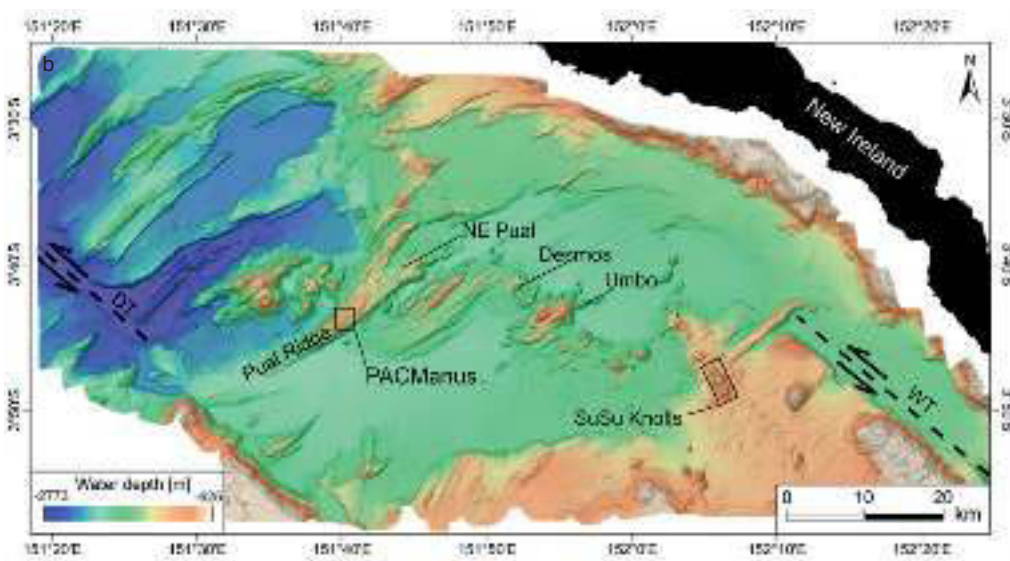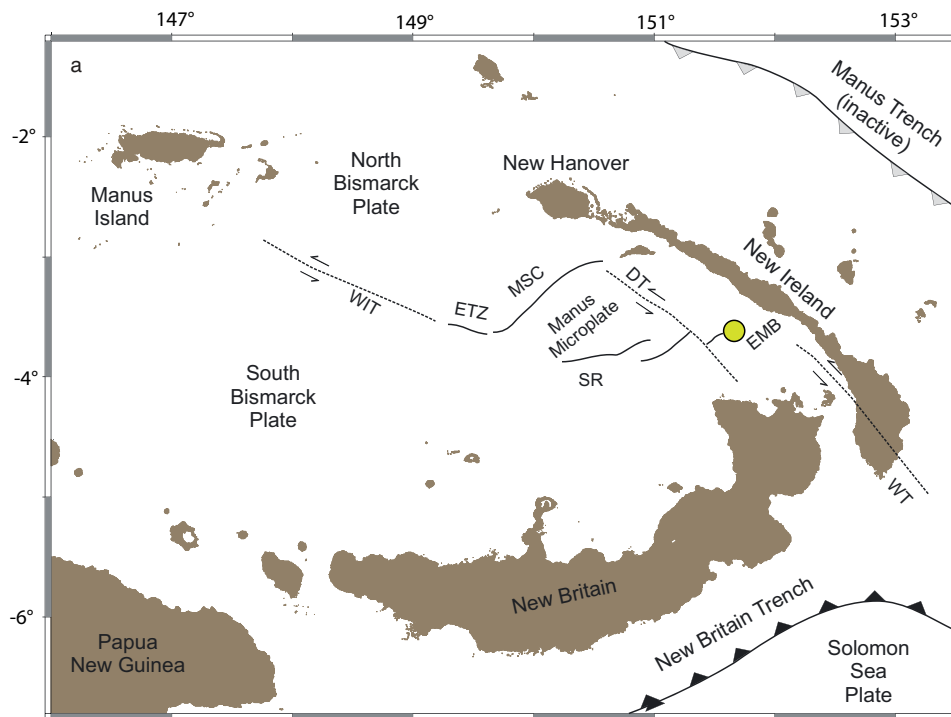
Figure 2.1: a) Geologic setting of the Pacmanus hydrothermal vent field in the Manus back-arc basin; b) Location of the Pual Ridge (Thal et al. 2014).

(Craddock et al. 2010). Superficial mineralization, however, shows little influence of magmatic $SO_2$ (Craddock and Bach 2010) but has signs of mixing with seawater (Reeves et al. 2011).

The samples investigated in this study are from the Fenway vent field at 1715 m water depth. Fenway has four vent clusters, of which the largest one (Big Papi) is located on top of an anhydrite mound (Thal et al. 2014). Big Papi was vigourously venting 356°C hot, boiling black smoker fluids in 2006 (Reeves et al. 2011). Five years later, the vigour of black smoker venting had subsided based on visual criteria (Thal et al. 2014). The northern termination of the Big Papi mound features abundant outcrops of massive anhydrite. These anhydrite deposits are surrounded by sulphidic sediment and show clear signs of dissolution due to reverse solubility of anhydrite. The massive anhydrite has also been subjected to upflow of vent fluids (fig. 2.2), which makes the samples ideal for examining the transition process from sulphate to sulphide.



Figure 2.2: Photograph of a black smoker sulphide chimney growing on top of anhydrite rubble. There is active replacement of anhydrite by sulphide (a) and signs of fossil sulphidation (f).

## 2.4 Methods

Thin sections from massive anhydrite samples from the Magellan-06 and SO216 cruise were visualized using optical (with both transmitted and reflected light) and electron microscopy, with a Leica DFC320 in Bremen and a JEOL Neoscope II JCM-6000 in Utrecht, respectively. Quantitative major element measurements were done using a Cameca SX100 microprobe in Bremen (accelerating voltage of 20 kV and beam current of 15 nA) and a JEOL JXA-8530F Hyperprobe in Utrecht (accelerating voltage of 15 kV and beam current of 25 nA). Both probes acquired data using a

wavelength-dispersive X-ray (WDX) spectrometer and used a selection of natural and synthetic minerals as standards. The latter microprobe was also used for cathodoluminescence analyses.

Minor and trace elements were measured using a ThermoFinnigan Element 2 LA-ICP-MS in Bremen with the standards BCR2G and BHVO2G. Points were measured with a laser pulse frequency of 5 Hz, an energy radiance $>$1GW/cm$^2$, dwell time of 60 sec and spot size of 35 $\mu$m; standards with 75 $\mu$m.

TEM images were obtained in Utrecht using a FEI Tecnai 20F at 200 kV, equipped with a high-angle annular dark field (HAADF) detector and an energy-dispersive X-ray (EDX) spectrometer. TEM-samples were prepared with a FEI Nova NanoLab 600 focused ion beam scanning electron microscope (FIB-SEM) in Utrecht, which was also used to image and cut slices in one of the samples (P1) to get an image stack for nanotomographic reconstruction of the sulphate-sulphide replacement microstructure. Slice imaging was carried out in backscattered electron mode at 2 kV and 0.84 nA with a pixel size of 20x20 nm$^2$ (voxel size of 20x20x30 nm$^3$). These images, along with those from a 360$^\circ$ rotated X-ray tomography scan (0.225$^\circ$ rotation per imaging step) at 160 kV and 35 nA and pixel size of 7.5x7.5 $\mu$m$^2$ using a ProCon CT-Alpha (Bremen) with an X-RAY WorX source and Hamamatsu detector, were used for a volume reconstruction with Avizo 8 Fire.

Fluid inclusion thermometry was performed on single anhydrite crystals using a Linkam THMSG 600 heating-cooling stage coupled to a LNP2 cooling pump and a TP 92 heating device. The sample was observed using a Zeiss Axioskop microscope. Salinity was determined by finding the melting point of the included fluid, and this in combination with homogenization temperature and a sample depth of 1700 m could be used to retrieve the formation temperatures and pressures of the analysed anhydrite crystals. Geochemists Work Bench was used for thermodynamic modelling, as was the EQ3/6 package (Wolery and Jarek 2003) for a reaction path model. The databases were constructed for temperatures up to 350$^\circ$C and 250 bars.

## 2.5 Results

### 2.5.1 Mineralogy

Anhydrite fragments for this study come from the Big Papi vent (depth of $\sim$ 1715 m) in the Fenway hydrothermal field and were collected during two cruises, in 2006 (Magellan-06, sample names R1 and R2) and 2011 (SO 216, sample names G1, G2, K1, K2 and P1), but both sample groups show

similar microstructures. They consist for >80% of 2-5 mm anhydrite crystals that show dissolution features and replacement by sulphides (pyrite, chalcopyrite and sphalerite). Radial barite needles with occasional sulphide overgrowth are restricted to big voids at anhydrite grain boundaries. Anhydrite microstructures include aligned fluid inclusions (fig. 2.3a), dissolution features such as triangular pits (fig. 2.3a,b) and porosity along the cleavage planes of anhydrite (fig. 2.3c, d), and alteration textures such as overgrowth in cleavage planes and at the edges of the crystal (fig. 2.3a,e). Sulphides occur in three different textural relationships: (1) within anhydrite, growing in lines parallel to the anhydrite mineral outline; (2) inside anhydrite cleavage planes; and (3) on triple junctions between anhydrite grains. With increasing extent of alteration, the volumetric abundance of the latter type increases in the samples. It is the dominant mode of sulphide occurrence in the 2006 samples, where anhydrite is more broken up along cleavage planes, allowing pyrite crystals to form in fractures.

The first type of sulphide occurrence defines mineral zoning inside anhydrite crystals (fig. 2.3c). These smooth-edged grains of sulphide (mostly chalcopyrite and some sphalerite) of approximately 10 $\mu$m diameter cluster in several bands that follow the outline of single anhydrite crystals. Electron microscopy revealed no internal or surrounding porosity (compare fig. 2.3c, 2d). The second type consists of larger (50-100 $\mu$m), euhedral sulphide grains. They are defined by porosity at the contact with surrounding anhydrite or gypsum (fig. 2.3b,d). Electron microscopy showed crystal subdomains, which are separated from each other by precipitation of nanoparticles or lines of porosity (fig. 2.3f). The third type is composed of large sulphide aggregates up to 2 mm in size. Euhedral pyrite in the core is surrounded by colloform chalcopyrite, with occasional porous sphalerite patches or porous pyrite crystals at its rim (fig. 2.3e). There is no porosity or overgrowth between sulphides.

Some anhydrite veins (0.5 cm width) with radially growing 0.5-1 mm needles crosscut all previously described microstructures and do not show any sign of alteration. Gypsum is sometimes seen to fill later cracks.
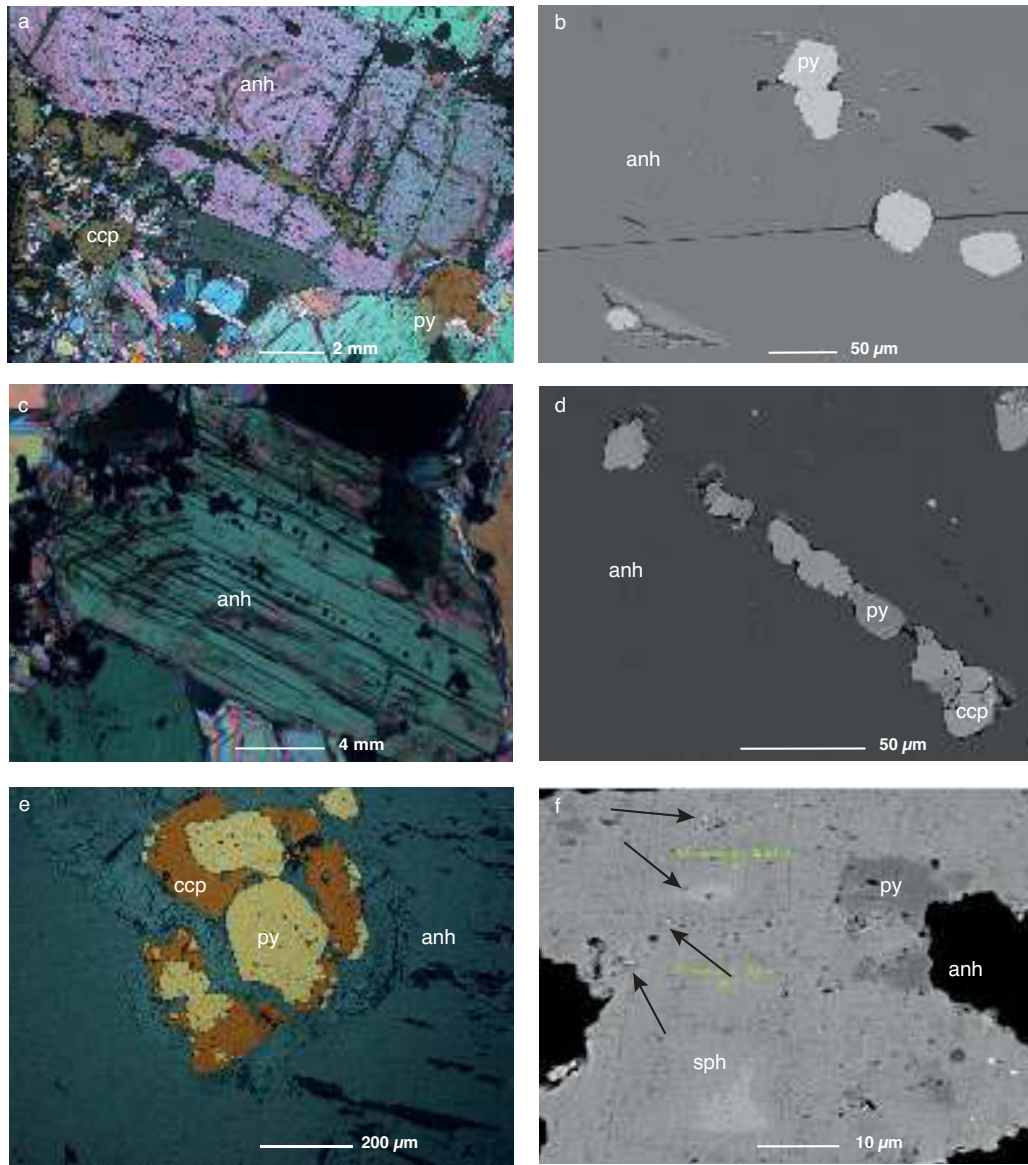
Figure 2.3: Optical (a,c,e) and electron (b,d,f) microscopy images. In a and e reflective light is used, showing sulphide minerals as yellow/brown or grey; otherwise they appear black. a) Fluid inclusions and triangular pits parallel to the anhydrite (anh) cleavage lines; b) Triangular shapes partially filled by sulphide; c) Anhydrite zoning with sulphide minerals (black) growing parallel to the mineral outline of anhydrite; d) Sulphides growing inside an opening cleavage plane of anhydrite, surrounded by porosity; e) Big sulphide aggregate shows internal structure of yellow pyrite (py) and orange chalcopyrite (ccp); f) Sphalerite (sph) crystal with lines of inclusions (white, indicated with arrows).

## 2.5.2  Porosity and rock microstructures

Besides inter- and intra-grain porosity, cracks and veins also contribute to total rock porosity. Anhydrite veins crosscut all previously mentioned microstructures, but no growth-induced fracturing by sulphides is observed. X-ray tomographic analysis of the pore space (fig. 2.4) shows that the main connected porosity appears to be developed along grain boundaries. The red colour in fig. 2.4 represents a single connected volume. Smaller and apparently disconnected pores are shown in different colours. Porosity accounts for 10% of the altered sample volume; unaltered sections have a porosity of 2-5%.
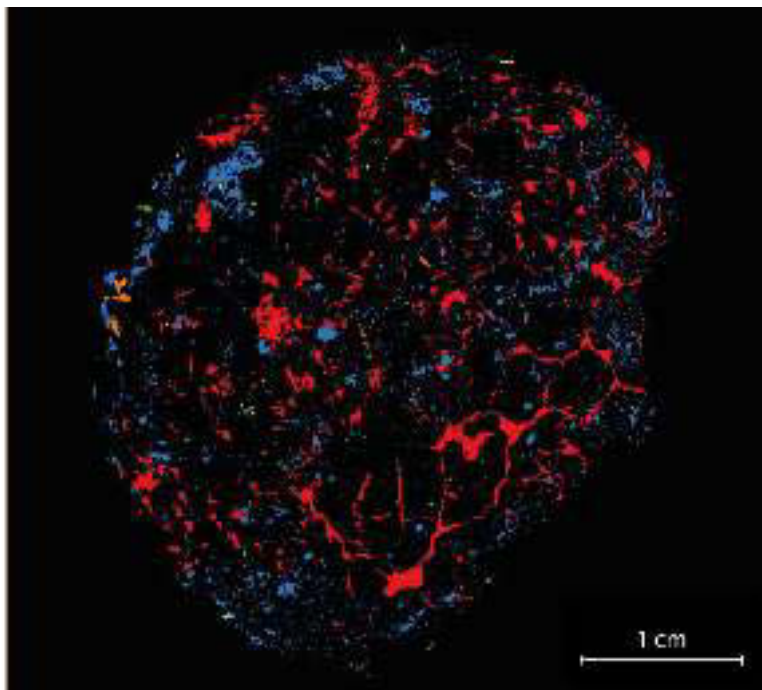


Figure 2.4: Top view of a tomographic scan of a cylindrical sample with segmented pores. All pore bodies are given in different colours. The red areas are connected throughout the whole sample, showing the perfect crystal outline of some anhydrites. Blue areas are smaller pores that seem to be isolated.

## 2.5.3  Mineral growth textures

Cracks or pore space inside anhydrite and sulphide grains cannot be depicted using $\mu$-tomography due to limited image resolution of 7.5 $\mu$m. To image these small-scale pores, a TEM section was prepared (fig. 2.5a). This section shows the submicron-sized bright phases (rich in Au and Pb)

that separate subdomains in sulphides (indicated with arrows in fig. 2.3f), occurring as inclusions that fill nano-pores in chalcopyrite and sphalerite. Porous or hollow pyrite is also observed in a FIB-cut cross section (sample P1) that displays an opening anhydrite cleavage plane in depth (fig. 2.5b). The pyrite grows from the edges of a crack to the inside, leaving the middle area open (see supplementary video). Some of these grains have globular shapes and grow inward to fill the hollow crystal.
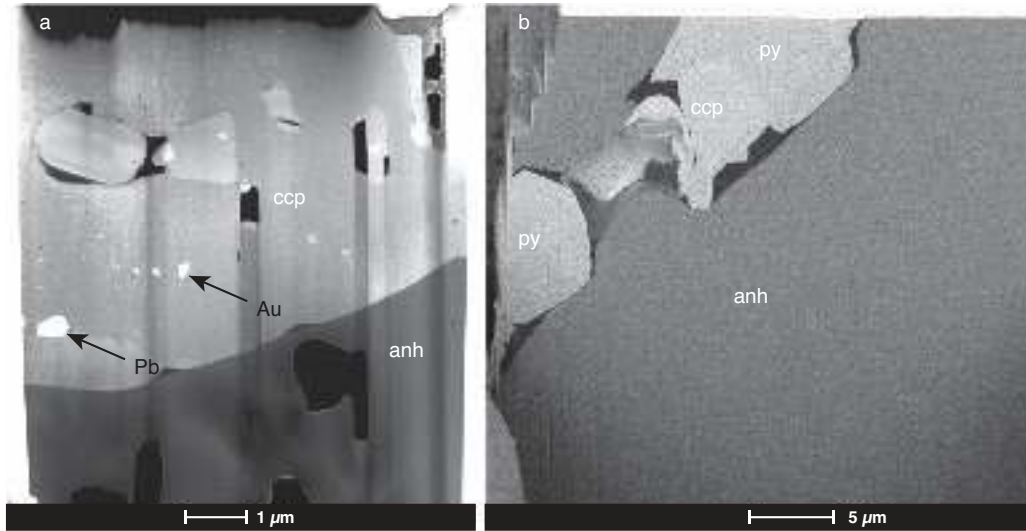


Figure 2.5: a) Micro-scale slice of the contact between anhydrite (dark, bottom) and sulphides (brighter). Anhydrite is non-porous while the sulphide is composed of several phases; some Pb and Au-bearing grains are present in the center and are surrounded by porosity. Lines running through both minerals are curtaining artifacts; b) A FIB-cut through the lined sulphides in fig. 2.3d. Sulphides grow in the cleavage plane in 3D, here also being built up of several grains. Pyrite grows euhedrally or from the edges inward, as chalcopyrite surrounds it and occasionally cracks the anhydrite.

Other features parallel to anhydrite cleavage planes are fluid inclusions (fig. 2.3a), which show salinities slightly higher than seawater (4 wt.% NaCl). However, this does not indicate that the entrapped fluid is not seawater as anhydrite re-dissolution can increase the salinity. Large elongated fluid inclusions (>20 $\mu$m in length) have a large range in homogenization temperatures above 300°C but might be influenced by physical stretching of the fluid inclusion obscuring the actual temperature. Irregular, smaller (1-10 $\mu$m) inclusions show more internally consistent temperatures of 240-280°C.

Cathodoluminescence coupled to quantitative X-ray element mapping sheds light on a possible relationship between zoning in anhydrite and sulphide growth parallel to the mineral outline (type 1). Clear trace element patterns associated to $Eu^{2+}$ can be seen as concentric zoning parallel to the cleavage of anhydrite (fig. 2.6a), which are traced by chalcopyrite and sphalerite at the outer rim. The association of $Eu^{2+}$ and $Eu^{3+}$ to the concentric zoning is confirmed by wavenumber position of the CL spectrum in fig. 2.6b (Baumer et al. 1997; Gaft et al. 2005). Secondary gypsum also shows distinct luminescence (bottom of fig. 2.6a).
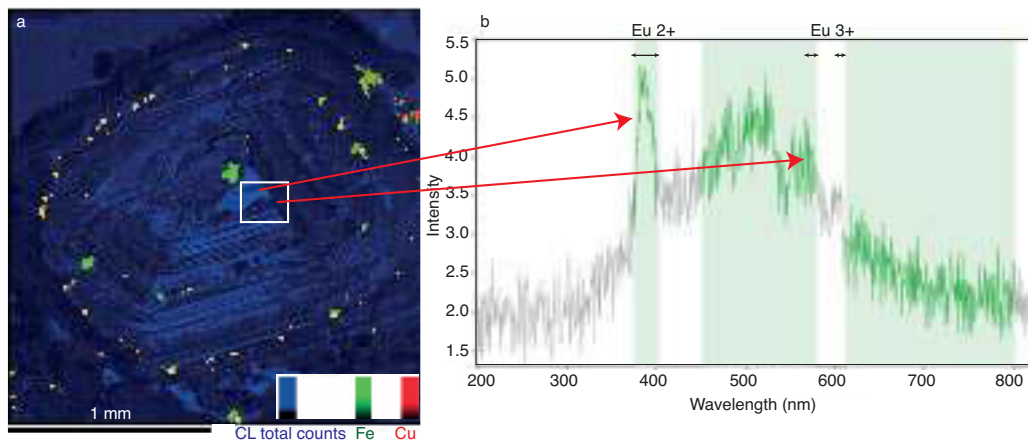


Figure 2.6: a) Zoning is confirmed by trace element content within the anhydrite crystal (shown as CL total counts in blue). Sulphide minerals occur as Fe (pyrite) in the center and Cu (chalcopyrite) in the outer rim. Secondary vein fill is seen as the blue worm shaped figure on the bottom of the image; b) Whole image CL spectrum showing the very clear $Eu^{2+}$-peak (left) mainly coming from areas with higher total CL counts; the darker blue parts with less CL total counts also show a weak $Eu^{3+}$-peak.

### 2.5.4 Mineral chemistry

Anhydrite is homogeneous in composition and no compositional variation was observed with grain size and with the precipitation environment, i.e. anhydrite located in veins or in the matrix. Stoichiometry calculations show a perfect $CaSO_4$ relation. Barite is also uniform in composition but shows significant incorporation of Sr (up to 1.5 wt.%). Gypsum does not show notable substitution of Ca by Ba or Sr (see supplementary data table 2).

For sulphides, element compositions are more variable and always add up to less than 100% due to the aforementioned micro-porosity (supplementary data table 3). Pyrite is relatively constant in

composition with a perfect 1:2 ratio for Fe and S, but LA-ICP-MS measurements (supplementary data table 4) reveal up to 2000 ppm As and 700 ppm Co in its structure. Chalcopyrite composition is very uniform but occasional incorporation of Zn (600 ppm) or As (50 ppm) was detected. Zn-rich sulphides (named sphalerite here) are the hardest to define due to chemical variability. Although rich in Zn, this mineral group does not always have enough zinc to be labeled as sphalerite, but also contains several wt.% of Fe (up to 20 wt.%), Cu (up to 30 wt.%) and other minor constituents (As 6 wt.%, Sb 0.2 wt.%, and Pb 7 wt.%) (fig. 2.7). Together, however, these elements add up to 50% of the atoms to make a close to 1:1 metal+metaloid:sulphide stoichiometry. Moreover, within a single sphalerite crystal the composition is variable.
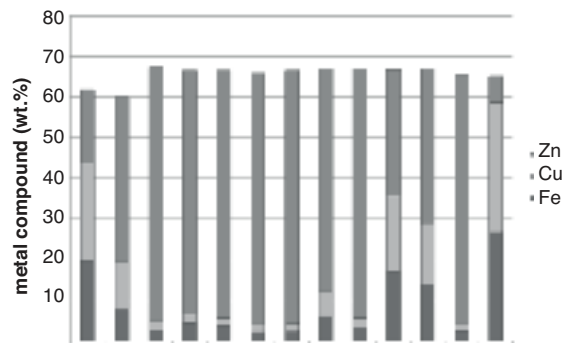


Figure 2.7: Columnar diagram displaying atomic percentages of metals in sphalerite and other Zn-bearing minerals. A combination of metals accounts for roughly 65% of the stoichiometry; the rest is made up by S.

## 2.6   Discussion

All microstructures observed here are consistent with the fluid-assisted replacement of anhydrite by pyrite, chalcopyrite and sphalerite. Sulphide minerals grow in cleavage planes or grain boundaries, thus following pore space in the primary mineral. This suggests that fluid infiltration occurred along high diffusivity pathways. The presence of different sulphide phases emphasizes the possibility of episodic growth and fluid infiltration. During this replacement reaction porosity was likely evolving dynamically as a result of continuous dissolution and precipitation. Below we discuss the different minerals and their microstructures in order to further define the replacement mechanism.

### 2.6.1 Anhydrite formation

Anhydrite ($CaSO_4$) forms directly when hydrothermal fluid mixes with seawater. Calcium is provided by the alteration of the underlying rock, while sulphate is derived from seawater. Above 150°C, anhydrite will precipitate from seawater-like solutions (Bischoff and Seyfried 1978; Blount and Dickson 1993); lower temperatures will dissolve anhydrite and (in a closed system) can form gypsum below $\sim 50$°C. The interplay of hydrothermal fluids and seawater causes temperature fluctuations, which results in interrupted anhydrite growth. Anhydrite may then develop crystal irregularities and micro-pores at the interface where growth ceased temporarily. Because anhydrite formation is known to be a pulsed phenomenon (Lalou et al. 1990; TAG: Humphris and Bach 2005; Pacmanus: Craddock and Bach 2010), the anhydrite zonations in Fenway are likely to have formed during episodes of increased fluid discharge and mixing with seawater. Variations in Eu contents across anhydrite grains relative to the neighbouring REE may record rapid oscillations in the system's oxidation state. A Sr isotope mass balance calculation using data from Craddock (2008) indicates an approximate 6:4 ratio of seawater versus hydrothermal fluid. In detail, nine analyses of sample J2-210-8-R2 reveal $^{87}Sr/^{86}Sr$ ratios between 0.70673 and 0.70806 (average: 0.70756). Given a $^{87}Sr/^{86}Sr$ ratio of 0.7045 and a Sr concentration of 95 $\mu$M for the Fenway end-member fluid and 0.70918 and 92 $\mu$M in seawater (Reeves et al. 2011), the average proportion of seawater in the mixed fluid from which the anhydrite precipitated is 66±9%. A mixture of 66% of 4°C seawater and 34% of 350°C vent fluid would have a temperature of 132°C if enthalpy was conserved during mixing. This temperature is much lower than what was indicated by the fluid inclusion homogenization temperatures of 240-280°C (corresponding to entrapment temperatures of 255-295°C for P=170 bar). These calculation results suggest that seawater must have been heated prior to mixing with the hydrothermal solution, a feature also observed in other anhydrite samples at the Pacmanus hydrothermal field (Vanko et al. 2004). For the mixture to have a temperature of 255°C, we computed (from H-T relations in Bischoff and Rosenbauer 1985) a temperature of 195°C for seawater in isenthalpic mixing with a 350°C vent fluid. A 295°C hot mixture would result from heating of seawater to 260°C prior to mixing.

Anhydrite precipitation in such a mixing regime will shield the conduits of vent fluid upflow from mixing with seawater. This shielding is anticipated to take place when sulphide chimneys evolve from initial anhydrite-rich structures (Haymon 1983). The hot, mildly acidic and reducing hydrothermal fluid is believed to corrode the inner conduit, causing sulphate replacement by sul-

phide. Fenway sulphide minerals can be found in 3 different textural relationships (fig. 2.3): (1) within anhydrite in zones that run parallel to grain boundaries, (2) inside the anhydrite cleavage planes and (3) on anhydrite grain boundaries. Additionally, triangular voids in anhydrite (fig. 2.3b) appear to be nucleation points for pyrite, although not all pores or pits on the surface are filled. Each type has its own features, making it possible to distinguish their growth and formation mechanism:

1. The first group consists of small sulphide minerals without surrounding porosity. They relate to anhydrite growth, precipitating in micro-porosity created during zoning (such pores are also observed by Sander and Black 1988). Since these pyrites are not surrounded by porosity, they are not considered replacive and they are not discussed any further in this communication.

2. The second group, located in cleavage planes or triangular pits, consists of idiomorphic pyrite grains surrounded (not overgrown) by colloform chalcopyrite and porosity. This texture implies that pyrite formed in an open space and upon continued fluid-rock interaction, chalcopyrite filled the rest of the irregular pore space leading to this colloform mineral shape. Occasional porous pyrite is present at the outer rim of the porous contact, showing that smaller pyrite crystals could form in the newly developed pores when anhydrite dissolution continued.

3. On anhydrite grain boundaries, the same sulphide minerals display similar phase relations but form larger aggregates. Additionally, chalcopyrite contains small patches of sphalerite. Occasionally, the microstructure shows chalcopyrite within pyrite or sphalerite predating chalcopyrite, indicating that rapid mixing with seawater in closed off pockets might have reversed the order of sulphide phase formation. The most common texture remains to be pyrite surrounded by chalcopyrite, and some rims of pyrite and sphalerite around this. As this sequence implies the same order of formation as before, one single sulphide formation sequence with fluid evolution has occurred within the rock, only to be recorded to different extents in different microtextural settings. Anhydrite cleavage planes were exposed to the percolating fluids progressing from pyrite + chalcopyrite back to pyrite, and thus display two or three sulphide growth stages. Along the grain boundaries, longer exposure to fluids is recorded and the whole sequence including sphalerite formation can be observed. This is to be expected, since porosity analysis shows that these pathways are still open to fluids (fig. 2.4). No signs of later oxidation are visible along these paths.

39

### 2.6.2 Sulphide growth

Although the observed variation in sulphide chemistry (supplementary data, table 3) is interesting it cannot give insight in mineral formation conditions. Therefore, we focus on microstructures instead of geochemistry to derive replacement conditions and development of porosity. Because pyrite has the tendency to form euhedral crystals even when its precursor has another shape, it is not feasible to deduce pyrite growth history based solely on its crystal habit (Graham and Ohmoto 1994). In addition, textural relationships should be taken into account. Fenway pyrite and chalcopyrite in cleavage planes nucleated at the contact between sulphide and sulphate as a thin film that thickens with time, filling the hollow sphere (fig. 2.5b; supplementary video). This tight contact with anhydrite shows that the sulphate may have acted as a substrate for (especially) pyrite nucleation. No evidence for the pre-existence of pyrrhotite or marcasite has been found, although this is thought to be necessary for the kinetics of this reaction (Janecky and Seyfried 1984). Sulphides simply seem to have started growing at the anhydrite surface that continued dissolving, leaving a porous contact.

Occasionally, smaller inclusions of pyrite, chalcopyrite or even Pb- and Au-rich inclusions are present inside sulphide crystals (fig. 2.3f, 2.5a). Such (nano)particles are surrounded by porosity and can form linear arrays through bigger sulphide crystals (fig. 2.3f). Palenik et al. (2004) suggested that nanoparticles form either directly out of the hydrothermal solution and can be exsolved upon cooling or by a rapid shift in oxidation state or pH (Butler and Nesbitt 1999). Upon ripening, they will coalesce and correlate to the porous or more distorted patches of the pyrite lattice. Coupled dissolution-precipitation could also redistribute the trace elements of pyrite (Sung et al. 2009). However, this is an unlikely scenario for replacement reactions at Fenway as no porous reaction front (Putnis et al. 2002) is observed around the nanoparticles and they have no alignment to suggest a reaction front. Another mechanism to create nanoparticles involves lattice diffusion (Deditius et al. 2011). Because Fenway nanoparticles occur in pores at irregular pyrite growth zones or at subgrain boundaries, exsolution of metals from the sulphide lattice could have led to formation of the observed nanoparticles.

Additionally, Fenway minerals contain a few wt.% As and Sb, mainly inside Zn-rich minerals. This positive correlation with Zn (also mentioned by Metz and Trefry 2000) is explained by Wohlgemuth-Überwasser et al. (2015) as a result of similar transport behavior during trace metal addition through magmatic volatiles, a process that also explains the overall low fluid pH at Fenway. Arsenic is bound in the lattice by substitution in pyrite (Reich et al. 2013), as is Cu. At equilibrium

with the pyrite, exsolution could form nanoparticles. Arsenic contents, however, are too low in the samples studied here to allow this process to take place and thus only Au and Pb nanoparticles are observed.

### 2.6.3 Porosity development

Porosity is crucial for the extent of a reaction, affecting both the creation of fluid pathways and the development of a large reactive surface area. In the Fenway samples this is manifested as leftover porosity and the absence of sulphide-induced cracking, both showing the importance of dissolution in this system. Another example is the micro-porous front in some sphalerite crystals. An increase in Fe seems to be coupled to increasing porosity (see porous patches and different grey values within one sphalerite crystal in fig. 2.3f). The aligned porosity in fig. 2.3f defines subdomains, and at the center of these subdomains a more Fe-poor sphalerite can be found. Iron was likely not only included during initial formation of sphalerite, but also came in during an interface coupled dissolution-precipitation reaction, which has been reported to create a porous product (Putnis 2002; Xia et al. 2009). This observation suggests that a late stage overprinting by Fe-rich fluid migrating through connected micro-pores controls the final sphalerite iron content. These textures are rare and only occur at grain boundaries with access to the pore network.

However, whether this whole network is connected remains to be investigated. Grain boundaries pose another area where fluids can enter and, in an open system, percolate through the rock. Interconnected pore space bound to grain boundaries (fig. 2.4) made the rock permeable to fluids and gave them access to the already formed sulphides, continuing growth and precipitation around them. The variable pyrite grain size can be explained in this sense by the moment of opening of the porous media around them; early opening has exposed the pore to extensive pyrite precipitation before temperatures were high enough to precipitate chalcopyrite. These pores are therefore the earliest to form, often occurring along grain boundaries where the first fluid access took place. Large aggregates at grain boundaries show that the rock remained open for late stage sulphide precipitation, which is absent in the more isolated cleavage planes.

Other important areas for fluid percolation due to high permeability are cracks and veins. Some cracks are cemented with barite (a low temperature sulphate) and late-stage gypsum, but pore connectivity in fig. 2.4 shows that flow remains possible. Veins filled with small anhydrite needles do not show any replacement or anhydrite dissolution. However, between the needles, anhedral porous

pyrite crystals are observed. This observation indicates that parts of the rock framework were open to fluids and experienced a late stage sulphide precipitation event, which was the formation of porous pyrite. This textural evidence points to a pulsed hydrothermal activity as previously reported by Lalou et al. (1990), Humphris and Bach (2005), and Craddock and Bach (2010). The pulsed fluid-rock contact results in supersaturation of different minerals, in a sequence. The rock must have been open to fluid flow facilitated by pre-existing interconnected porosity (roughly 5%) or through the creation of new fluid pathways such as fractures and reaction-induced porosity. In conclusion, we suggest that precipitation of the observed mineral sequences occurred in an open system rather than in closed-off pockets. This shows the extent of anhydrite dissolution.

### 2.6.4    Replacement reaction and conditions

Besides fluid composition, temperature is the main factor that separates the stability field of sulphide phases (fig. 2.8). In most hydrothermal fluids, pyrite forms below 350°C (Janecky and Seyfried 1984), sphalerite below and chalcopyrite above 250°C (Haymon and Kastner 1981) while other Cu-bearing phases form at temperatures beyond 350°C (Haymon 1983). Temperature constraints are also given by the silica system, where above 200°C, precipitation of quartz is inhibited (Janecky and Seyfried 1984). Upon cooling, the fluid pH will go down, inducing silica precipitation, anhydrite dissolution and the formation of barite (Tivey et al. 1995). Cooling as a result of batch mixing with seawater will lead to precipitation of Mg-hydroxides and sulphides such as covellite ($CuS$), chalcocite ($Cu_2S$) and bornite ($Cu_5FeS_4$) (Haymon 1983), but the absence of these phases in the Fenway anhydrite mound suggests that a large entrainment flux of seawater was not realized after the bulk anhydrite had formed.

The observed sulphide assemblage of Fenway thus fits this general sulphide sequence of a system that is heated (hydrothermal fluid addition) and cooled afterwards (hydrothermal activity ceased). Starting with a hydrothermal fluid at 250°C and a seawater fraction of 0.66 (concluded from fluid inclusions and Sr isotope mass balance in anhydrite crystals), pyrite could precipitate in opening cleavage planes only just outside the stability field of sphalerite ([1] in fig. 2.8). Upon shielding of the inner conduit, the fraction of hydrothermal fluid increased and the system heated up. Anhydrite was partially corroded because of the reducing conditions and low pH (not shown in the diagram but both affecting anhydrite stability). This process created room for more pyrite, heated the system and supplied metals leading to colloform chalcopyrite growth in the pores ([2] in fig. 2.8).

42

The late-stage porous pyrite and even sphalerite surrounding chalcopyrite represent a decrease in temperature resulting in the stabilization of sphalerite, upon the supply of Fe and Zn [3]. Additional anhydrite does not form, while barite is stable under these conditions when enough Ba is present in the system (fig. 2.8).
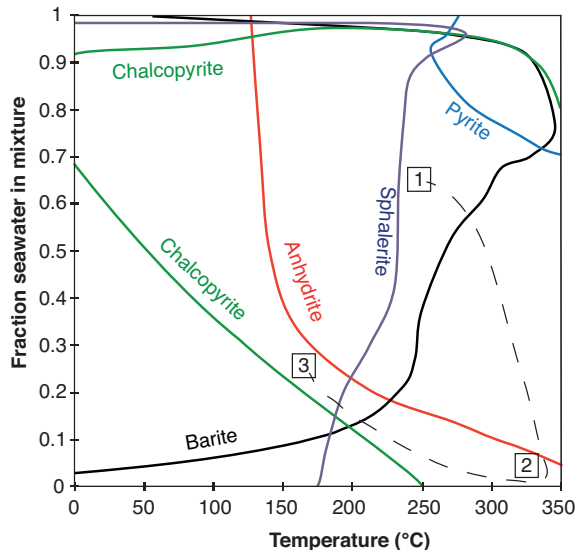


Figure 2.8: T-X section displaying mineral stability fields at 250 bars. The diagram was constructed by computing phase relations along mixing paths of seawater and Fenway endmember vent fluid (Reeves et al. 2011) under variable seawater heat and vent fluid cooling. A proposed reaction path model for the Fenway system is shown; points 1, 2 and 3 represent the different stages of sulphate and sulphide formation. For further explanation, see text.

To gain further insight into the sequence of reactions and the chemical evolution of the hydrothermal sulphate-sulphide system we conducted geochemical reaction path modelling using EQ3/6 (Wolery and Jarek 2003). As starting fluid, one kg of hydrothermal fluid (F2 vent data from Reeves et al. (2011) provided in supplementary table 1, found next to the collected massive anhydrite samples) was allowed to speciate; from it, anhydrite, pyrite and chalcopyrite are expected to precipitate as shown in fig. 2.9a. Notice that upon cooling, sulphide will become more stable than sulphate. This fluid was subsequently reacted with 600 g of anhydrite at 343°C, the measured exit temperature of F2. The computed reaction path showed that only 0.37 g of anhydrite reacted with the fluid before reaching equilibrium, leading to some pyrite and minor chalcopyrite formation within the conduit. Shielding from seawater by continued anhydrite precipitation lead to more

43

metal supply and heating of this system to 350°C, resulting in more pyrite and chalcopyrite precipitation. Later cooling by a small influx of seawater (Vanko et al. 2004) brought the system back into the sphalerite field (fig. 2.9b with a 1:8 hydrothermal fluid-seawater mix), and together with the supplied metals this resulted in the observed Zn-rich sulphide phase along with more anhydrite dissolution.

The first step in the reaction is thus a replacement of anhydrite by pyrite. Thermodynamic models defined by others (Janecky and Seyfried 1984; Shanks et al. 1981; Tivey and McDuff 1990) have predicted the most favourable reactions under several circumstances. Their models provide reaction constants and can predict mineral stability and co-precipitation. On the basis of the aforementioned results and a pressure of 250 bar as well as a temperature range from 200-400°C we are able to define the controlling sulphate-sulphide reaction as

$$2CaSO_4 + Fe^{2+} + 7H_2(aq) + 2H^+ \rightarrow FeS_2 + 2Ca^{2+} + 8H_2O$$
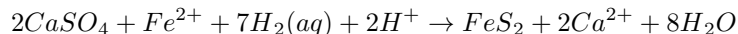
This would coincide with the first arrow of fig. 2.8, where as soon as anhydrite comes into contact with hot, Fe-bearing hydrothermal fluid, pyrite starts to form. Depending on the presence of certain metals, pyrite, chalcopyrite or other sulphides can be formed in EQ3/6 (when suppressing low temperature Cu phases which are stable but would not form under these conditions) after this initial step.

Although our model is purely thermodynamic and leaves out kinetic effects of fluid flow or particle physics considering nanopores we are able to capture the system's phase relationships and make first order predictions of the mineralogical evolution. Our microstructural investigation, however, stresses the need for next-generation models of hydrothermal systems that account for the physic-chemical aspects of fluid-driven replacement reactions coupling the dynamic evolution of porosity and permeability to mineral reactions.

### 2.6.5 Replacement mechanism and process

For the replacement reaction of anhydrite to pyrite, the first assemblage (pyrite on the edge of opening anhydrite) is the key. Many authors have mentioned this replacement reaction with a precursor, whether this is a basaltic rock assemblage (Bischoff and Dickson 1975; Shanks et al. 1981), pyrrhotite (Haymon 1983; Janecky and Seyfried 1984; Tivey and McDuff 1990), pyrite nanopar-
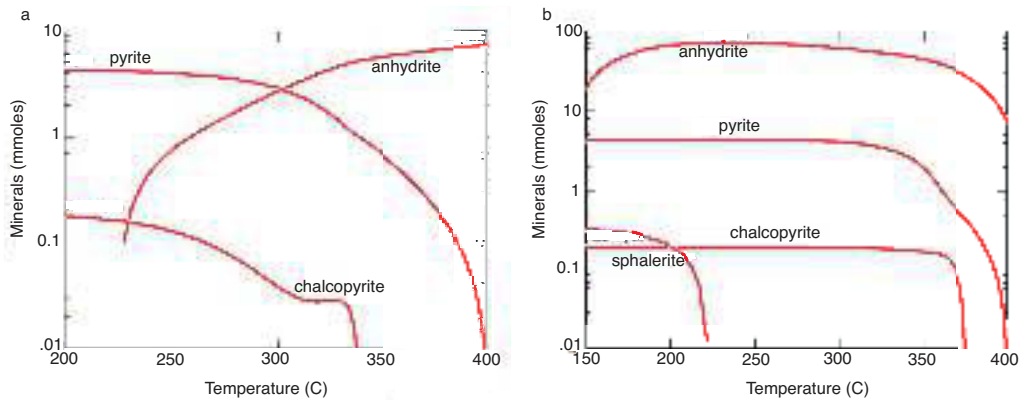
Figure 2.9: a) Mineral quantity expected to precipitate from the starting hydrothermal fluid F2 (Reeves et al. 2011). Notice that pyrite is stable over the whole temperature range but has trouble forming at high temperatures. Chalcopyrite is stable below 350°C but will form especially around this temperature, Cu solubility being highly temperature dependent (Wohlgemuth-Überwasser et al. 2015); b) Mixing of hydrothermal fluid with seawater in a ratio 1:8 shows that sphalerite will become stable upon dissolution of anhydrite especially below 230°C.

ticles (Gartman and Luther 2013) or even liquid sulphur droplets (Graham and Ohmoto 1994). However, none of the proposed mechanisms are consistent with the microstructures observed in the massive anhydrite from the Fenway hydrothermal field. Our observations document that sulphides nucleate directly on the surface of anhydrite, forming a coating that subsequently grows inwards (fig. 2.5b) while the anhydrite continues to dissolve. An 82% volume reduction accompanies this reaction, where 2 moles of anhydrite (molar volume of 46 cm$^3$/mole) are replaced by a single mole of pyrite (24 cm$^3$/mole); the rest remains as pore space. This feature, together with the tendency of anhydrite to dissolve upon cooling, can explain the formation of extensive porosity. Dissolution of anhydrite and precipitation of sulphide are facilitated by a positive feedback: the reaction creates porosity, which enables more fluid to progress deeper within the rock and cause more replacement. Dissolution starts along the grain boundaries, where sulphides form, and continues when fluids get access to the cleavage planes. The released sulphur couples to metals that are supplied by the hydrothermal fluid from alteration reactions in the rock framework below. Temperature increases with time inside the massive anhydrite and Cu-contents increase, leading to the formation of chalcopyrite to fill the pore space around it. A later influx of colder water, or the cessation of hydrothermal input lowers the amount of dissolved Cu while pyrite keeps precipitating and upon further cooling,

45

sphalerite will form. During the final stage, veins of anhydrite occur and gypsum can precipitate in cracks. Their presence shows the small influx of low temperature seawater, supplying sulphate. The key to the Fenway system remains the dissolution of anhydrite, which provides building blocks, a substrate and a space for sulphides to grow. This intriguing coupling between reaction progress and permeability evolution warrants further investigation.

## 2.7   Implications for seafloor massive sulphide deposit evolution

The results obtained here provide new insight into the replacive formation of massive sulphide deposits on the seafloor and will help to interpret the formation and evolution of more complex hydrothermal seafloor massive sulphide systems, such as the TAG system at MAR 26°N. Our investigation highlights that particularly the role of transient porosity and changing permeability should be taken into account. Humphris et al. (1995) already stated the importance of anhydrite dissolution in their interpretation of a collapsed mound, leading to the formation of the pyrite breccia observed at TAG. Collapsed mound fragments were juxtaposed to the wall rock and both were influenced by later hydrothermal activity, which lead to the formation of new anhydrite in between pyrite fragments and to silicification of the wall rock. The role of previously created porosity in the overall development of a deposit is crucial and may explain observed heterogeneities in ore grade. Models that include both physical and chemical aspects of these fluid-mediated reactions are needed. Further studies in volcanogenic massive ore deposition should not solely apply thermodynamic equilibrium constraints but should also consider permeability development to get a detailed picture of the formation of a larger sulphide deposit. The applications do not stop at these systems, however; many types of mineral-replacement reactions, including albitization, serpentinization and carbonation, can affect large portions of the oceanic and continental crust.

## 2.8   Acknowledgements

## 2.9   References

Barnes HL (1979) Geochemistry of Hydrothermal Ore Deposits, 2$^{nd}$ edn. John Wiley & Sons: New York

Barnes HL (1997) Geochemistry of Hydrothermal Ore Deposits, 3$^{rd}$ edn. John Wiley & Sons: New York

Barnes HL (1997b) Solubilities of ore minerals. In: Barnes HL (ed) Geochemistry of Hydrothermal Ore Deposits, 3$^{rd}$ edn. John Wiley & Sons, pp 404-460

Barriga FJAS, Fyfe WS (1988) Giant pyritic base-metal deposits: the example of Feitais (Aljustrel, Portugal). Chem Geol 69:331-343

Baumer A, Blanc Ph, Cesbron F, Ohnenstetter D (1997) Cathodoluminescence of synthetic (doped with rare-earth elements) and natural anhydrites. Ch Geol 138:73-80

Beier C, Bach W, Turner S, Krumm S (2015) Origin of Silicic Magmas at Spreading Centres –an Example from the South East Rift, Manus Basin. J Petrol 56(2):255-272

Binns RA, Scott SD (1993) Actively forming polymetallic sulfide deposits associated with felsic volcanic rocks in the eastern Manus Basin, Papua New Guinea. Econ Geol 88:2226-2236

Bischoff JL, Dickson FW (1975) Seawater-basalt interaction at 200°C and 500 bars: implications for origin of sea-floor heavy-metal deposits and regulation of seawater chemistry. Earth Planet Science Lett 25:385-397

Bischoff JL, Rosenbauer RJ (1985) An empirical equation of state for hydrothermal seawater (32 percent NaCl). Am J Science 285:725-763

Bischoff JL, Seyfried Jr WE (1978) Hydrothermal chemistry of seawater from 25° to 350°C. Am J Science 278:838-860

Blount CW, Dickson FW (1993) Gypsum-Anhydrite equilibria in Systems $CaSO_4$-$H_2O$ and $CaCO_4$-NaCl-$H_2O$. Am Mineral 58:323-331

Burnham CW (1967) Hydrothermal fluids in the magmatic stage. In: Barnes HL (ed) Geochemistry of Hydrothermal Ore Deposits. Holt, Rinehart and Winstons, pp 34-76

Burnham CW (1979) Magmas and hydrothermal fluids. In: Barnes HL (ed) Geochemistry of Hydrothermal Ore Deposits, 2nd edn. John Wiley & Sons, pp 71-136

Butler IB, Nesbitt RW (1999) Trace element distributions in the chalcopyrite wall of a black smoker chimney: insights from laser ablation inductively coupled plasma mass spectrometry (LA-ICP-MS). Earth Planet Science Lett 167:335-345

Carmichael DM (1969) On the mechanism of prograde metamorphic reactions in quartz-bearing pelitic rocks. Contrib Mineral Petrol 20:244-267

Corliss JB, Dymond J, Gordon LI, Edmond JM, von Herzen RP, Ballard RD, Green K, Williams D, Bainbridge A, Crane K, van Andel T (1979) Submarine Thermal Springs on the Galápagos Rift. Science 203(4385):1073-1083

Craddock PR (2008) Attention deficit/hyperactivity disorder and creativity: An investigation into their relationship. Dissertation, Massachusetts Institute of Technology and Woods Hole Oceanic Institute, Woods Hole, USA

Craddock PR, Bach W (2010) Insights to magmatic-hydrothermal processes in the Manus back-arc basin as recorded by anhydrite. Geoch Cosmoch Acta 74:5514-5536

Craddock PR, Bach W, Seewald JS, Rouxel OJ, Reeves E, Tivey MK (2010) Rare earth element abundances in hydrothermal fluids from the Manus Basin, Papua New Guinea: Indicators of sub-seafloor hydrothermal processes in back-arc basins. Geoch Cosmoch Acta 74:5494-5513

Deditius AP, Utsunomiya S, Reich M, Kesler SE, Ewing RC, Hough R, Walshe J (2011) Trace metal nanoparticles in pyrite. Ore Geol Rev 42:32-46

Einaudi M, Meinert LD, Newberry RJ (1981) Skarn deposits. Econ Geol 75th Anniversary Vol, 317-391

Eugster HP (1985) Granites and hydrothermal ore deposits: a geochemical framework. Mineralog Mag 49:7-23

Gaft M, Reisfeld R, Panczer G (2005) Luminescence Spectroscopy of Minerals and Materials. Springer-Verlag, Berlin Heidelberg

Gartman A, Luther III GW (2013) Comparison of pyrite ($FeS_2$) synthesis mechanisms to reproduce natural $FeS_2$ nanoparticles found at hydrothermal vents. Geoch Cosmoch Acta 120:447-458

Graham UM, Ohmoto H (1994) Experimental study of formation mechanisms of hydrothermal pyrite. Geoch Cosmoch Acta 58-10:2187-2202

Hannington M, Herzig P, Scott S, Thompson G, Rona P (1991) Comparative mineralogy and

geochemistry of gold-bearing sulfide deposits on the mid-ocean ridges. Mar Geol 101:217-248

Haymon RM (1983) Growth history of hydrothermal black smoker chimneys. Nat 301:695-698

Haymon RM, Kastner M (1981) Hot spring deposits on the East Pacific Rise at 21°N: preliminary description of mineralogy and genesis. Earth Planet Science Lett 53:363-381

Helgeson HC (1969) Thermodynamics of hydrothermal systems at elevated temperatures and pressures. Amer J Sci 267:729-804

Helgeson HC (1979) Mass transfer along minerals and hydrothermal solutions. In: Barnes HL (ed) Geochemistry of Hydrothermal Ore Deposits, 2$^{nd}$ edn. John Wiley & Sons, pp 568-610

Humphris SE, Bach W (2005) On the Sr isotope and REE compositions of anhydrites from the TAG seafloor hydrothermal system. Geoch Cosmoch Acta 69(6):1511-1525

Humphris SE, Cann JR (2000) Constraints on the energy and chemical balances of the modern TAG and ancient Cyprus seafloor sulfide deposits. J Geophys Res 105(B12):28477-28488

Humphris SE, Herzig PM, Miller DJ, Alt JC, Becker K, Brown D, Brügmann G, Chiba H, Fouquet Y, Gemmell JB, Guerin G, Hannington MD, Holm NG, Honnorez JJ, Itturino GJ, Knott R, Ludwig R, Nakamura K, Petersen S, Reysenbach A-L, Rona PA, Smith S, Sturz AA, Tivey MK, Zhao X (1995) The internal structure of an active sea-floor massive sulphide deposit. Nat 377:713-716

James RH, Elderfield H (1996) Chemistry of ore-forming fluids and mineral formation rates in an active hydrothermal sulphide deposit on the Mid-Atlantic Ridge. Geol 24:1147-1150

James RH, Green DRH, Stock MJ, Alker BJ, Banerjee NR, Cole C, German CR, Huvenne VAI, Powell AM, Connelly DP (2014) Composition of hydrothermal fluids and mineralogy of associated chimney material on the East Scotia Ridge back-arc spreading centre. Geoch Cosmoch Acta 139:47-71

Jamtveit B, Hammer Ø(2012) Sculpting of Rocks by Reactive Fluids. Geochem. Perspectives 1-3:341-472

Janecky DR, Seyfried Jr WE (1984) Formation of massive sulfide deposits on oceanic ridge crests: Incremental reaction models for mixing between hydrothermal solutions and seawater. Geoch Cosmoch Acta 48:2723-2738

Kamenetsky VS, Binns RA, Gemmell JB, Crawford AJ, Mernagh TP, Maas R, Steele D (2001) Parental basaltic melts and fluids in eastern Manus back-arc Basin: implications for hydrothermal mineralization. Earth Planet Science Lett 184:685-702

Lalou C, Thompson G, Arnold M, Brichet E, Druffel E, Rona PA (1990) Geochronology of TAG and Snakepit hydrothermal fields, Mid-Atlantic Ridge: witness to a long and complex hydrothermal history. Earth Planet Science Lett 97:113-128

Lindgren W (1933) Mineral Deposits. McGraw-Hill

Martinez F, Taylor B (1996) Backarc Spreading, Rifting, and Microplate Rotation, Between Transform Faults in the Manus Basin. Mar Geophys Res 18:203-224

Mathez EA (1989) Interactions involving fluids in the Stillwater and Bushveld Complexes: observations from the rocks. Rev Econ Geol 4:167-179

Metz S, Trefry JH (2000) Chemical and mineralogical influences on concentrations of trace metals in hydrothermal fluids. Geoch Cosmoch Acta 64-13:2267-2279

Palenik CS, Ustunomiya S, Reich M, Kesler SE, Wang L, Ewing RC (2004) "Invisible"gold revealed: direct imagining of gold nanoparticles in a Carlin-type deposit. Am Mineral 89:1359-1366

Paulick H, Vanko DA, Yeats CJ (2004) Drill core-based facies reconstruction of a deep-marine felsic volcano hosting an active hydrothermal system (Pual Ridge, Papua New Guinea, ODP Leg 193). J Volcanol Geotherm Res 130:31-50

Putnis A (2002) Mineral replacement reactions: from macroscopic observations to microscopic mechanisms. Mineral Mag 66:689-708

Putnis A, Austrheim H (2010) Fluid-induced processes: metasomatism and metamorphism. Geofluids 10:254-269

Revan MK, Genç Y, Maslennikov VV, Maslennikova SP, Large RR, Danyushevsky LV (2014) Mineralogy and trace-element geochemistry of sulfide minerals in hydrothermal chimneys from the Upper-Cretaceous VMS deposits of the eastern Pontide orogenic belt (NE Turkey). Ore Geol Rev 63:129-149

Reeves EP, Seewald JS, Saccocia P, Bach W, Craddock PR, Shanks WC, Sylva SP, Walsh E, Pichler T, Rosner M (2011) Geochemistry of hydrothermal fluids from the PACMANUS, Northeast Pual and Vienna Woods hydrothermal fields, Manus Basin, Papua New Guinea. Geochem Cosmoch Acta 75:1088-1123

Reich M, Deditius A, Chryssoulis S, Li J-W, Ma C-Q, Angel Parada M, Barra F, Mittermayr F (2013) Pyrite as a record of hydrothermal fluid evolution in a porphyry copper system: A SIMS/EMPA trace element study. Geochim Cosmochim Acta 104:42-62

Sander MV, Black JE (1988) Crystallization and recrystallization of growth-zoned quartz crystals

from epithermal systems: implications for fluid inclusions studies. Econ Geol 83:1052-1060

Seewald JS, Seyfried Jr WE (1990) The effect of temperature on metal mobility in subseafloor hydrothermal systems: constraints from basalt alteration experiments. Earth Planet Science Lett 101:388-403

Seward TM, Barnes HL (1997) Metal transport by hydrothermal ore fluids. In: Barnes HL (ed) Geochemistry of Hydrothermal Ore Deposits, 3$^{rd}$ edn. John Wiley & Sons, pp 435-486

Seyfried Jr WE, Ding K (1995) Phase equilibria in subseafloor hydrothermal systems: a review of the role of redox, temperature, pH and dissolved Cl on the chemistry of hot spring fluids at Mid-Ocean Ridge. In: Humphris SE, Zierenberg R, Mullineaux L, Thomson R (eds) Seafloor Hydrothermal Systems: Physical, Chemical, Biological and Geological Interactions. Geophys Monogr Vol 91 Am Geophys Union, pp 248-272

Shanks WC, Bischoff JL, Rosenbauer RJ (1981) Seawater sulfate reduction and sulfur isotope fractionation in basaltic systems: Interaction of seawater with fayalite and magnetite at 200-350°C. Geochim Cosmochic Acta 45:1977-1995

Sinton JM, Bergmanis E, Rubin KH, White SM (2002) Volcanic eruptions on mid-ocean ridges: New evidence from the superfast spreading East Pacific Rise, 17-19°S. J Geophys Res Atmos 107:3-20

Sung Y-H, Brugger J, Ciobanu CL, Pring A, Skinner W, Nugus M (2009) Invisible gold in arsenian pyrite and arsenopyrite from a multistage Archaean gold deposit: Sunrise Dam, Eastern Goldfields Province, Western Australia. Mineral Depos 44:765-791

Thal J, Tivey M, Yoerger D, Jöns N, Bach W (2014) Geologic setting of PACManus hydrothermal area –High resolution mapping and in situ observations. Mar Geol 335:98-114

Tivey MK, Humphris SE, Thompson G, Hannington MD, Rona PA (1995) Deducing patterns of fluid flow and mixing within the TAG active hydrothermal mound using mineralogical and geochemical data. J Geophys Res 100:12527-12555

Tivey MK, McDuff RE (1990) Mineral Precipitation in the Walls of Black Smoker Chimneys: A Quantitative Model of Transport and Chemical Reaction. J Geophys Res 95(B8):12617-12637

Tornos F, Peter JM, Allen R, Conde C (2015) Controls on the siting and style of volcanogenic massive sulphide deposits. Ore Geol. Review 68: 142-163

Vanko DA, Bach W, Roberts S, Yeats CJ, Scott SD (2004) Fluid inclusion evidence for subsurface phase separation and variable fluid mixing regimes beneath the deep-sea Pacmanus hydrothermal

field, Manus Basin back-arc rift, Papua New Guinea. J Geophys Res 109, B03201101029/2003JB002579

Wohlgemuth-Überwasser CC, Viljoen F, Petersen S, Vorster C (2015) Distribution and solubility limits of trace elements in hydrothermal black smoker sulfides: An in-situ LA-ICP-MS study. Geochim Cosmochim Acta 159:16-41

Wolery TW, Jarek RL (2003) Software User′s Manual EQ3/6, Version 8.0, Sandia National Laboratories. Albuquerque, NM, USA

Xia F, Brugger J, Chen G, Ngothai Y, O′Neill B, Punis A, Pring A (2009) Mechanism and kinetics of pseudomorphic mineral replacement reactions: a case study of the replacement of pentlandite by violarite. Geochim Cosmochim Acta 73:1945-1969

Yardley BWD (2009) On the role of water in the evolution of the continental crust. Journ Geol Soc (London)166:585-600

Zhu W, Tivey MK, Gittings H, Craddock PR (2007) Permeability-porosity relationships in seafloor vent deposits: Dependence on pore evolution processes. J Geophys Res 112 B05208, doi:101029/2006JB004716

## 2.10 Appendix

Supplementary data Table 1. Vent fluid samples from 5 Fenway vents, measured at 25°C. Concentrations are in mmol/kg fluid unless otherwise indicated (data from Reeves et al, 2011; Cu + Zn from Craddock, 2008)

| | sample | T(°C) | Mg | pH | Na | Cl | Ca | Fe | K | SiO2 | SO4 | ΣCO2 | ΣH2S | H2 (µM) | Cu (µM) | Zn (µM) |
|---|---|---|---|---|---|---|---|---|---|---|---|---|---|---|---|---|
| F1 | J2-210-IGT1 | 329 | 5.97 | 2.5 | 347 | 463 | 14.3 | 7.37 | 53.8 | 12.7 | 0.93 | 61.3 | 18.5 | 24 | 2.4 | 21.3 |
| | J2-210-M4 | 329 | 5.84 | 2.6 | 340 | 465 | 14.3 | 7.56 | 53.8 | | | | | | 176.2 | 220.2 |
| | J2-214-IGT1+ | 329 | 39.8 | 4.5 | 422 | 520 | 11.3 | 2.03 | 21.2 | 3.69 | 20.3 | 17.7 | 4.6 | 6.4 | 0 | 6.5 |
| F2 | J2-212-IGT8 | 343 | 4.9 | 2.7 | 485 | 683 | 25.2 | 13.3 | 86.4 | 13.8 | 0.55 | 23.6 | 9.2 | 95 | 1.6 | 12.8 |
| | J2-212-IGT5 | 343 | 5.26 | 2.7 | 485 | 685 | 25.2 | 13.1 | 85.8 | 13.8 | 0.74 | 23.3 | 9 | 93 | 3.5 | 20.3 |
| | J2-212-M4 | 343 | 4.66 | 2.7 | 483 | 685 | 25.7 | 13.4 | 86.8 | | | | | | 88.4 | 169.4 |
| F3 | J2-212-IGT2 | 358 | 4.52 | 2.7 | 417 | 589 | 22.2 | 11.5 | 73.9 | 11.9 | 0.97 | 44 | 15 | 233 | 1.3 | 12.8 |
| | J2-212-IGT1 | 358 | 4.74 | 2.8 | 377 | 517 | 20.3 | | 64.9 | 10.4 | 2.45 | 58.6 | 19.3 | 325 | 0.3 | 17.2 |
| | J2-212-M2 | 358 | 8.89 | 2.8 | 425 | 573 | 20.4 | | 66.8 | | | | | | 62.5 | 118.9 |
| F4 (mix) | J2-216-IGT7 | 284 | 8.95 | 2.6 | 395 | 527 | 17.7 | 6.85 | 60.2 | 10.9 | 2.46 | 51.8 | 11.6 | 25 | 6.7 | 52.8 |
| | J2-216-IGT6 | 284 | 8.69 | 2.5 | 392 | 524 | 17.7 | | 60.7 | 11.3 | 2.17 | 54.7 | 11.6 | 26 | 4 | 26 |
| | J2-216-M2 | 284 | 10.2 | 2.4 | 394 | 527 | 17.4 | | 58.2 | | | | | | 111.2 | 223.6 |
| F5 | J2-216-IGT4 | 80 | 45 | 5 | 437 | 517 | 13.3 | 0.868 | 14.1 | 1.72 | 27.6 | 14.4 | 2.5 | 2.8 | 0 | 30.7 |
| | J2-216-IGT3 | 80 | 44 | 4.9 | 436 | 517 | 14.1 | | 15.3 | 1.9 | 27.4 | 15.5 | 2.7 | 2.7 | 0 | 13.2 |
| | J2-216-M4 | 80 | 48.8 | 5.8 | 453 | 535 | 11.8 | | 11.7 | | | | | | 0.7 | 1 |

*Supplementary data Table 2. Major element chemistry (wt.%) in sulphates*

**Anhydrite**

|    | Mg   | S     | Sr   | Ca    | Ba    | Fe   | O     | Total  |
|----|------|-------|------|-------|-------|------|-------|--------|
| 2  | 0.01 | 23.17 | 0    | 29.63 | 0.04  | 0    | 46.51 | 99.36  |
| 3  | 0    | 23.51 | 0    | 30.26 | 0.03  | 0.01 | 47.27 | 101.07 |
| 4  | 0    | 23.41 | 0    | 30.38 | 0     | 0.03 | 47.17 | 100.99 |
| 5  | 0    | 23.14 | 0    | 30.75 | 0     | 0.01 | 46.91 | 100.81 |
| 6  | 0.00 | 23.03 | 0    | 31.14 | 0     | 0.01 | 46.91 | 101.09 |
| 7  | 0    | 22.98 | 0    | 31.46 | 0.04  | 0.03 | 46.96 | 101.47 |
| 8  | 0    | 22.68 | 0    | 31.30 | 0.05  | 0.01 | 46.44 | 100.48 |
| 9  | 0.04 | 22.28 | 0    | 28.84 | 0.05  | 0.05 | 44.87 | 96.14  |
| 10 | 0    | 23.14 | 0    | 30.92 | 0.01  | 0    | 46.98 | 101.05 |
| 11 | 0.01 | 23.28 | 0    | 30.67 | 0.05  | 0.02 | 47.09 | 101.10 |
| 12 | 0.00 | 22.83 | 0    | 31.51 | 0     | 0.01 | 46.74 | 101.09 |
| 13 | 0    | 22.82 | 0    | 30.11 | 0.01  | 0.02 | 46.18 | 99.15  |
| 14 | 0    | 22.95 | 0    | 30.12 | 0.07  | 0.07 | 46.38 | 99.59  |
| 15 | 0.02 | 23.01 | 0    | 29.11 | 0     | 0    | 46.06 | 98.21  |
| 16 | 0.01 | 23.05 | 0    | 30.79 | 0.01  | 0    | 46.79 | 100.65 |
| 17 | 0.02 | 22.91 | 0    | 30.96 | 0.02  | 0.03 | 46.65 | 100.58 |
| 18 | 0.01 | 23.57 | 0    | 30.18 | 0     | 0    | 47.32 | 101.08 |
| 19 | 0    | 22.71 | 0    | 30.51 | 0.00  | 0.01 | 46.17 | 99.40  |
| 20 | 0    | 22.37 | 0    | 28.17 | 0.04  | 0    | 44.72 | 95.30  |
| 21 | 0.01 | 23.38 | 0    | 30.49 | 0     | 0.01 | 47.17 | 101.06 |
| 22 | 0.01 | 23.47 | 0    | 27.39 | 0     | 0.04 | 46.05 | 96.95  |
| 23 | 0    | 23.51 | 0    | 27.96 | 0.04  | 0.03 | 46.35 | 97.89  |
| 24 | 0    | 23.51 | 0    | 28.12 | 0.01  | 0.01 | 46.42 | 98.08  |

**Barite**

|   | Mg | S     | Sr   | Ca   | Ba    | Fe   | O     | Total  |
|---|----|-------|------|------|-------|------|-------|--------|
| 1 | 0  | 14.40 | 1.55 | 0.45 | 58.03 | 0.00 | 28.78 | 103.21 |
| 2 | 0  | 13.90 | 1.25 | 0.21 | 58.71 | 0.07 | 27.99 | 102.12 |
| 3 | 0  | 14.16 | 1.35 | 0.40 | 57.21 | 0.13 | 28.31 | 101.56 |
| 4 | 0  | 14.16 | 1.39 | 0.36 | 56.98 | 0.15 | 28.28 | 101.32 |

**Gypsum**

|   | Mg   | S     | Sr | Ca    | Ba   | Fe   | O     | Total |
|---|------|-------|----|-------|------|------|-------|-------|
| 1 | 0.01 | 21.19 | 0  | 28.96 | 0    | 0.28 | 43.37 | 93.81 |
| 2 | 0.02 | 22.43 | 0  | 28.38 | 0.02 | 0.27 | 45.00 | 96.12 |
| 3 | 0.01 | 22.69 | 0  | 29.40 | 0.03 | 0.04 | 45.74 | 97.91 |

*Supplementary data Table 3. Major element chemistry (wt.%) in sulphides*

**Pyrite**

|  | Fe | S | As | Co | Cu | Zn | Mn | Sb | Total |
|---|---|---|---|---|---|---|---|---|---|
| 1 | 46.27 | 54.37 | 0.05 | 0 | 0.65 | 0.01 | 0.02 | 0.03 | 101.38 |
| 2 | 45.43 | 53.74 | 0.02 | 0 | 0.86 | 0.04 | 0.01 | 0.00 | 100.10 |
| 3 | 46.18 | 54.31 | 0.06 | 0 | 0.22 | 0.02 | 0.02 | 0 | 100.81 |
| 4 | 45.63 | 53.43 | 0.06 | 0 | 0.61 | 0.00 | 0.02 | 0 | 99.75 |
| 6 | 45.54 | 53.86 | 0.07 | 0 | 0.78 | 0.01 | 0.01 | 0 | 100.26 |
| 7 | 45.74 | 53.54 | 0.03 | 0.01 | 1.31 | 0 | 0 | 0 | 100.62 |
| 8 | 45.27 | 52.74 | 0.09 | 0.02 | 2.07 | 0.29 | 0 | 0 | 100.47 |
| 9 | 46.71 | 54.17 | 0.03 | 0.00 | 0.15 | 0 | 0 | 0 | 101.06 |
| 10 | 45.24 | 53.60 | 0.03 | 0 | 1.32 | 0 | 0 | 0 | 100.18 |
| 11 | 45.17 | 53.71 | 0.12 | 0 | 1.05 | 0 | 0.01 | 0 | 100.06 |
| 12 | 44.95 | 53.78 | 0.21 | 0 | 1.22 | 0 | 0 | 0 | 100.16 |
| 13 | 43.81 | 53.85 | 0.13 | 0.01 | 2.15 | 0.27 | 0 | 0 | 100.22 |
| 14 | 41.25 | 52.85 | 0.08 | 0 | 5.22 | 0 | 0 | 0 | 99.39 |
| 15 | 46.12 | 54.01 | 0.28 | 0 | 0.71 | 0 | 0.03 | 0 | 101.16 |
| 16 | 45.91 | 53.52 | 0.40 | 0 | 0.63 | 0 | 0 | 0 | 100.46 |
| 17 | 45.90 | 54.81 | 0.20 | 0 | 0.81 | 0.30 | 0.01 | 0 | 102.02 |
| 18 | 45.58 | 53.79 | 0.16 | 0.00 | 0.91 | 0.53 | 0 | 0 | 100.97 |

**Sphalerite**

|  | Fe | S | As | Co | Cu | Zn | Mn | Sb | Total |
|---|---|---|---|---|---|---|---|---|---|
| 1 | 5.16 | 32.35 | - | 0 | 0 | 58.47 | - | - | 95.98 |
| 1_1 | 8.07 | 32.94 | - | 0 | 0 | 53.72 | - | - | 94.77 |
| 2 | 2.69 | 33.34 | 0.00 | 0 | 2.05 | 62.66 | 0.10 | 0.17 | 101.02 |
| 4 | 4.35 | 33.69 | 0 | 0 | 2.20 | 60.10 | 0.12 | 0.01 | 100.48 |
| 5 | 3.65 | 33.71 | 0 | 0 | 2.03 | 60.88 | 0.02 | 0.01 | 100.32 |
| 5_U | 9.41 | 33.04 | - | 0.03 | 0 | 52.49 | - | - | 95.79 |
| 7 | 2.08 | 33.27 | 0.03 | 0.01 | 1.96 | 61.97 | 0.04 | 0.02 | 99.40 |
| 8 | 2.25 | 33.33 | 0 | 0.01 | 1.91 | 62.46 | 0.03 | 0 | 100.03 |
| 9 | 6.08 | 33.86 | 0 | 0 | 5.98 | 54.97 | 0.04 | 0 | 101.66 |
| 10 | 3.29 | 33.61 | 0 | 0 | 2.31 | 61.45 | 0.03 | 0.02 | 100.74 |

*Table 3 continued: Sulphides*

Chalcopyrite

|     | Fe    | S     | As   | Co   | Cu    | Zn   | Mn   | Sb   | Total |
|-----|-------|-------|------|------|-------|------|------|------|-------|
| 1   | 29.98 | 35.08 | 0    | 0.01 | 33.99 | 0.09 | 0.02 | 0.07 | 99.14 |
| 2   | 29.81 | 35.16 | 0    | 0.00 | 34.08 | 0.01 | 0.04 | 0.05 | 99.31 |
| 3   | 29.65 | 35.17 | 0    | 0.01 | 34.11 | 0.07 | 0.03 | 0.05 | 99.09 |
| 4   | 29.55 | 35.26 | 0.09 | 0.00 | 34.08 | 0.08 | 0.03 | 0.02 | 99.05 |
| 5   | 29.15 | 35.21 | 0.04 | 0.02 | 33.62 | 0.10 | 0.02 | 0.02 | 98.19 |
| 6   | 27.69 | 34.68 | 0.02 | 0    | 32.53 | 0.19 | 0    | 0.01 | 95.16 |
| 7   | 29.54 | 35.08 | 0.02 | 0.01 | 33.99 | 0.08 | 0.03 | 0.06 | 98.82 |
| 8   | 30.04 | 35.31 | 0    | 0.01 | 34.53 | 0.01 | 0.00 | 0    | 99.91 |
| 9   | 30.00 | 34.75 | 0    | 0.02 | 34.26 | 0.52 | 0    | 0.03 | 99.57 |
| 10  | 29.94 | 35.20 | 0.09 | 0.00 | 33.98 | 0.02 | 0.01 | 0    | 99.24 |
| 11  | 30.14 | 35.31 | 0    | 0.01 | 34.30 | 0    | 0.01 | 0.01 | 99.78 |
| 12  | 29.42 | 35.25 | 0    | 0    | 33.76 | 0    | 0.01 | 0.00 | 98.44 |
| 13  | 30.00 | 35.14 | 0    | 0    | 33.89 | 0.02 | 0    | 0    | 99.05 |
| 14  | 29.18 | 35.07 | 0.01 | 0.00 | 33.66 | 0    | 0.00 | 0.01 | 97.97 |
| 15  | 29.49 | 34.60 | 0    | 0.00 | 32.33 | 0.01 | 0.02 | 0.05 | 96.49 |
| 16  | 30.10 | 35.66 | 0    | 0.00 | 32.66 | 0.16 | 0.03 | 0    | 98.61 |
| 17  | 30.30 | 35.31 | 0    | 0.02 | 33.03 | 0.00 | 0.02 | 0    | 98.68 |
| 18  | 30.38 | 35.35 | 0    | 0.03 | 33.50 | 0.05 | 0.01 | 0    | 99.31 |
| 19  | 29.96 | 35.33 | 0    | 0.00 | 33.20 | 0.01 | 0.00 | 0    | 98.53 |
| 20  | 29.50 | 35.55 | 0.03 | 0.01 | 33.47 | 0.97 | 0.02 | 0.02 | 99.57 |
| 21  | 29.70 | 35.31 | 0    | 0.01 | 33.63 | 0.57 | 0.00 | 0    | 99.21 |

*Supplementary data Table 4. LA-ICP-MS trace metal measurements in sulphides (ppm)*

|  | Co | Ni | Zn | As | Sb | Pb | U |
|---|---|---|---|---|---|---|---|
| py (core) | 234.79 | 5.13 | 37.55 | 379.18 | 0.35 | 6.98 | 0.12 |
| py | 399.73 | 3.24 | 1.43 | 310.80 | 0.20 | 3.53 | 0.00 |
| py | 7.06 | -0.43 | 632.24 | 18.33 | 0.90 | 10.99 | 0.25 |
| py | 1.18 | -0.59 | 514.12 | 807.04 | 1.87 | 150.66 | 0.24 |
| py | 406.83 | 1.54 | 4.21 | 217.75 | 0.12 | 2.18 | 0.06 |
| py | 696.05 | 3.40 | 29.87 | 524.16 | 0.62 | 13.76 | 4.94 |
| ccp | 0.39 | -0.84 | 629.32 | 26.73 | 7.75 | 9.31 | 0.31 |
| py (aggregate) | 29.27 | -0.13 | 149.01 | 366.13 | 0.87 | 27.21 | 5.54 |
| py (cleavage) | 0.36 | -2.40 | 269.82 | 1203.22 | 2.81 | 91.46 | 1.93 |
| sph | 4.01 | -18.29 | 7649720.22 | 63862.61 | 2527.95 | 71222.00 | 1.60 |
| sph | 4.35 | -1.30 | 3570755.48 | 35643.19 | 1895.06 | 9648.06 | 0.22 |
| ccp | 0.10 | 1.18 | 407.10 | 57.64 | 5.83 | 25.59 | 0.44 |
| py (porous) | 125.34 | 1.17 | 0.92 | 253.98 | 0.42 | 5.53 | 1.78 |
| py (edge) | 0.44 | 0.43 | 128239.48 | 179.51 | 36.89 | 311.53 | 1.69 |
| py (cleavage) | 1.04 | 1.45 | 15253.72 | 1988.10 | 17.68 | 919.09 | 10.90 |

# 3 Sulfidation of major rock types of the oceanic lithosphere: an experimental study at 250°C and 400 bars

*Catharina Los (1), Wolfgang Bach (1,2)*

Contact: los@uni-bremen.de, tel. 0049 421 218 65406

(1) Geosciences Department, University of Bremen, Klagenfurter Str. 2, 28359 Bremen, Germany

(2) MARUM, Center for Marine and Environmental Sciences, Leobener Str. 28359 Bremen, Germany

## 3.1 Abstract

Circulation of hydrothermal fluids within the oceanic crust is a major factor in mass and heat transfer between hydrosphere and lithosphere. Many occurrences of massive sulfide have been reported along the mid-ocean ridges, showing effective mass transfer of sulfur and metals in these systems. Besides precipitation of sulfide at the seafloor, replacive sulfide formation in the sub-seafloor has been documented. However, different lithologies are expected to have different

affinities to sulfidization. To investigate the role of rock composition on sulfidization efficiency, we have conducted batch experiments at 250°C and 400 bars that placed an $H_2S$-rich hydrothermal fluid into contact with four different rock types: dunite (olivine separates), troctolite, basalt, and serpentinite. These rocks were exposed to fluids containing 20 mmol/kg total dissolved sulfide for durations between 1 and 10 weeks. In situ fluid sampling allowed us to determine the evolution of the concentrations of ionic solutes and dissolved gases. Solid products were analyzed after termination of the experiments, using XRD, SEM, TG and VSM. Geochemical modeling was employed to compare observed reaction with equilibrium thermodynamic predictions.

Sulfide (in the form of euhedral pyrite crystals) could be observed only in the basalt experiment. In all other runs, conditions were too reducing for sulfide formation. Instead, the troctolite and peridotite experiments showed serpentinization of olivine and magnetite formation. Plagioclase in troctolite experienced desilicification, resulting in andradite. The stability field of sulfide in the $H_2$-$H_2S$ activity plane is diminished due to the prevalence of andradite in hydrothermally reacted troctolite and sulfidization in the troctolite experiment was hence inhibited. The serpentinite experiment showed very little reaction and no sulfide formation. Our results show that olivine-rich seafloor lithologies are not very prone to sulfidation; basaltic crust appears to have a larger potential to form sulfide deposits. In some experiments, pyrrhotite did not form although $H_2$-$H_2S$ activities plot in the pyrrhotite stability field of the Fe-O-S phase diagram. We suggest that the higher oxidation state in basalt allows for the precipitation of pyrite, which is not stable under the more reducing conditions prevailing where water interacts with olivine-rich lithologies.

## 3.2   Introduction

Hydrothermal fluid circulation within the oceanic lithosphere plays a large role in mass and heat transfer on Earth. Rock alteration can occur through exposure to magmatic fluids and percolating seawater close to spreading ridges, by infiltration of seawater in (deep) fractures or by the development of core complexes (e.g., Smith et al. 2008; Melchert et al. 2008; Petersen et al. 2009). The reactive fluid leaches out fluid mobile elements, which are re-deposited upon cooling

and oxidation when the fluid ascends to the ocean floor (Seewald and Seyfried 1990). Local enrichments of heavy metals such as Fe, Cu, Zn and Ni are often captured within sulfide minerals. Although many sulfide-bearing root zones are discovered, not all rock types have the same potential to form massive sulfide deposits.

Sulfide is present in minor amounts in most lithologies exposed at the seafloor, displaying its stability in the oceanic lithosphere. In basalts or gabbros sulfides often have a magmatic origin (Czamanske and Moore 1977; Peach et al. 1990), which is visible in sulfur isotopes; altered rocks show more mixed signatures (e.g., Delacour et al. 2008a), implying S-addition to the system through hydrothermal processes. One sulfur enrichment process leading to hydrothermal sulfide formation is thermogenic sulfate reduction above $250°C$, which has been suggested to be driven by protons released from Mg-metasomatism (Shanks et al. 1981). At lower temperatures abiotic sulfate reduction is kinetically sluggish and seawater sulfate reduction is catalyzed microbially (Alt and Shanks 1998; Delacour et al. 2008a; Schwarzenbach et al. 2012; Alt et al. 2013). Deeper sections of the lithosphere consist of ultramafic rock types such as plagioclase-bearing troctolites, where not many sulfides are reported (Früh-Green et al. 1996; Alt et al. 2007; Delacour et al. 2008b). Instead, metals are commonly stored in spinels or as oxides. Hydrothermal circulation can destabilize these minerals and dissolve them, increasing metal content in the fluid. One example of hydrothermal alteration is the hydration of peridotite, manifested as serpentinization (Seyfried and Dibble 1980; Godard et al. 2013; Klein et al. 2015; and others). During this process, magnetite forms and high amounts of $H_2$ are produced, causing de-sulfidation of the ultramafic rock (Frost 1985; Klein and Bach 2009). The resulting release of $H_2S$ and subsequent transport may result in the precipitation of sulfide phases close to the seafloor (Alt and Shanks 2003; Bach et al. 2004a; Delacour et al. 2008b). Sulfides can also form replacively, postdating other alteration events and overprinting preexisting alteration textures (Marques et al. 2006; 2007).

In the case of replacement of the host rock by sulfides, an ore body with a high metal concentration can form. Such sulfide deposits have been discovered along many plate boundaries in all exposed lithologies of the oceanic lithosphere. Especially freshly formed basalt is well known to host large amounts of pyrite, a relatively oxidized sulfide phase that is found here surrounded by zones of silicification, chloritization and sericitization (upflow zone of TAG, Humphris et al. 1995). This pyrite is often enriched in trace elements through zone refining processes (Hannington et al. 1998). At depth, pyrite fragments are cemented either by anhydrite (shallow) or quartz

(deeper sections). In the upflow zone, sulfidation can actually replace wall rock or create sulfide-bearing veins, observed both in drill cores (Hannington et al. 1998; Bach et al. 2004a) and ophiolite sections (Zierenberg et al. 1988; Adamides 2010).

Several experimental studies have looked into seawater-rock interaction and replacive sulfide formation. Bischoff and Dickson (1975) showed that at 200°C, seawater-basalt interaction decreased fluid pH because Mg-metasomatism released $H^+$ from the rock. Simultaneous Mg-Ca exchange resulted in precipitation of sulfate as anhydrite (Mottl and Holland 1978). Mottl et al. (1979) found anhydrite and additional pyrite or pyrrhotite at 300°C and 400°C; these sulfide phases were also observed in experimental runs where no sulfate was added in solution. The authors linked sulfate reduction to ferrous iron oxidation. Shanks et al. (1981) tested this iron oxidation with fayalite-seawater experiments at 250°C and 350°C and different w/r ratios. They found that at low w/r (<50), pyrrhotite and magnetite formed while at higher ratios, more oxidizing conditions prevailed and pyrite, hematite and anhydrite were present. These examples show that sulfur plays a large role in alteration of the oceanic crust and that more study on sulfidation is needed.

This communication looks at the potential of different lithologies to form sulfide minerals upon interaction with sulfide-bearing solutions. We conducted experiments that placed basalt, troctolite, serpentinite and pure olivine (to resemble peridotite protolith) in contact with an $H_2S$-rich solution representing a black smoker vent fluid. Our experiments used the same fluid with 20 mmol/kg $H_2S$ for all rock types in order to distinguish the rock potential, with different water-to-rock (w/r) ratios. In natural systems, a w/r >10 is hard to realize except right next to a discharge area with high upflow rates. However, as a high w/r oxidizes the system and the used fluid adds large quantities of sulfur, it represents the most favorable conditions to form pyrite that we could test. Both the solid reaction products and the composition of the reaction fluids (including dissolved gases) were analyzed in order to determine the rock potential; this was then compared to modeled thermodynamic mineral stability.

## 3.3 Methods

### 3.3.1 Experimental setup

In order to simulate water-rock reactions under hydrothermal conditions, a powdered (75-150 $\mu$m fraction) rock sample and de-oxygenized milliQ-water were weighed in a flexible gold cell (volume of roughly 100 mL). NaOH was added to acquire a fluid pH of 9-9.5 at 250°C. $Na_2S$-flakes were added to this fluid and the cell was closed immediately after with a titanium ring attached to a pressure vessel. A tube connected to a valve at the top of the autoclave allowed us to sample the fluid during the reaction. The flexible gold cell was flushed with nitrogen and the headspace of the valve was emptied using this pressure. The autoclave was filled with water and closed tightly. This water was pressurized with air and the whole setup was placed within a heater. Two thermocouples (at top and bottom of the pressure vessel) monitored temperature in the reaction cell, which was set to 250°C. During heating, the pressure increased by expansion of the fluid within the pressure vessel; we decompressed when it exceeded 420 bars. When 250°C was reached, the system stabilized and pressure was kept constant around 400 bars for 1-10 weeks depending on the $H_2$ produced by the ongoing reaction. At 400 bar and 250°C, $H_2$ solubility in mildly salty solutions is very high (Sleep et al. 2004) and all $H_2$ produced is dissolved in the fluid ($H_2$,aq). Activities of $H_2$ and $H_2S$ were calculated from measured concentrations of these compounds, assuming unity activity coefficients. Because the aim of this study was to form sulfide minerals, the reaction was stopped when conditions moved outside the pyrite or pyrrhotite stability field. For the experimental setup, see fig.1 from Shibuya et al. (2013).

### 3.3.2 Different experiments

Five experiments were run, listed below with starting pH at 25°C: The very first basalt experiment was shut down after one day due to pressure loss. Basalt: 5.2046 g rock, 74.9675 mL fluid, 223 mg $Na_2S$, fluid pH of 9.5, ran for 63 days; Troctolite: 4.486 g rock, 72.385 mL fluid, 198 mg $Na_2S$, fluid pH 11.0, ran for 49 days; Olivine: 0.8976 g rock, 74.6063 mL fluid, 192 mg $Na_2S$, fluid pH 11.5, ran for 9 days; Serpentinite: 0.7876 g rock, 73.4624 mL fluid, 181 mg $Na_2S$, fluid pH 10.5, ran for 11 days. After termination of each experiment, solids were removed and centrifuged in milliQ to remove reaction fluid and salt build-up, and then dried under low-$O_2$ conditions.

### 3.3.3 Analyses

Fluid samples were taken by carefully opening the pressure valve. After removal of the headspace of the valve (1.5 mL) an airtight syringe was used to capture 1 mL of fluid. Dissolved gases in the basalt experiment were measured using a 7820A Agilent Gas-Chromatograph (GC) equipped with a thermal conductivity detector (TCD) for $H_2$, led through a Molsieve 60/80 column with $N_2$ as carrier gas. Measured standards contained 1.031 vol.% $H_2$, 1.031 vol.% CO, 1.012 vol.% $CO_2$ and 0.996 vol.% $CH_4$. For the other experiments, a Peak Performer 1 was used and a standard with 10 ppm $H_2$ and CO; the taken samples were diluted to fall within the range calibrated by the standard. Major element chemistry was measured on fluid samples diluted with 1% $HNO_3$ using Inductively Coupled Plasma-Optical Emission Spectroscopy (ICP-OES) of the type Varian Vista using 3 standards to calibrate (Konz, VF2, VF10). These measurements were performed on the degassed samples after GC-measurement in order to maximize the use of fluid samples, since every sample decreased the water-to-rock ratio within the gold cell. For dissolved $H_2S$ an additional sample was taken where all sulfur was fixated directly with zinc-acetate; this sample was measured using a Dr5000 Photometer.

Solids were analyzed using a Supra 40 Scanning Electron Microscope (SEM) with an XFlash 6/30 Energy Dispersive X-ray (EDX)-detector (15 kV) or with electron microprobe analysis (EMPA) using a Cameca SX100 (20 kV, 1 $\mu$m beam size) on the starting material. Thermogravimetry was done using a Netzsch DTA-TG machine using a heating rate of 10 K/min. X-ray powder diffraction (XRD) analysis was performed on both starting and product materials using a Philips X′Pert Pro multipurpose diffractometer equipped with a Cu-tube (k$\alpha$ 1.541, 45 kV, 40 mA), a fixed divergence slit of 1/4°, a 16 samples changer, a secondary Ni-Filter and the X′Celerator detector system. An Axios Plus of Panalytical was used for X-ray Fluorescence bulk rock data, at ICBM in Oldenburg, Germany (see table 3.1 for bulk and mineral compositions) just on starting material. This technique was performed on glass pellets and data quality was checked using a PS-S black shale standard; detection limits were never higher than 0.03 wt.%; the average error was 0.1.

Magnetic properties were measured at the Norwegian University of Science and Technology (NTNU). High and low temperature magnetic susceptibility was measured using an Agio MFK1-A Kappabridge with CS4 and CS-L units, respectively, analyzing the type of magnetic mineral looking for the Curie temperature (high temperature) and possible Verwey transition (low

temperature) if the mineral was magnetite. To quantify this magnetic phase, saturation magnetization (which increases linearly with the amount of magnetic mineral) was determined using hysteresis loops and high temperature magnetic measurements performed with a Princeton Measurements Corporation MicroMag 3900 Vibrating Sample Magnetometer (VSM). This value was corrected for linear paramagnetic slope and the curves were further analyzed using the Igor software package.

### 3.3.4   Modeling

To predict geochemical behavior and mineralogical changes, the EQ3/6 work package (Wolery and Jarek, 2003) was used. A database for 500 bars was constructed; equilibrium constants were determined using SUPCRT92 (Johnson et al. 1992) while activity coefficients were calculated using the Debye-Hückel equation. In these models, the starting material was entered as a special reactant whose composition was derived from XRF-data on the materials used. Ferrous iron components were taken to be 0.8-0.9 for the mafic rock types and 0.33 for the serpentinite. Different ratios were modeled (10, 20, 50, 100) in order to find the best conditions for sulfide formation. This outcome was used to calculate the amount of sample that should be added to the fluid.

The predicted mineral stability in the Fe-O-S system at 250°C and 400 bars was plotted in an activity-activity diagram, using Log a $H_2S$ vs. Log a $H_2$ as axis variables. The changing w/r during the experiment was not taken into account because reaction time could not be accurately estimated due to unknown kinetic variables. Instead, modeled reactions were allowed to run to the end, and at several w/r because this ratio changed during the run. The changing ratio limited the number of possible samples; subtracting too much fluid would move the system out of the preferred stability field. Speciation of measured total sulfur in the fluid samples was predicted using the EQ3/6 software to calculate $H_2S$-activity, assuming an activity coefficient of 1 since these species have neutral charge.

### 3.4   Results

We have executed 4 successful runs with a duration of 1-10 weeks each. The reacted material has been imaged using SEM (fig. 3.1a-d) and major fluid chemistry is given in fig. 3.2a-e and table

| SAMPLE | olivine | troctolite | | |
|---|---|---|---|---|
| datatype | bulk rock | bulk rock | mineral (ol) | mineral (pl) |
| $SiO_2$ | 40.81 | 41.06 | 39.55 | 47.79 |
| $Al_2O_3$ | n.d. | 5.39 | 0.04 | 30.7 |
| $FeO, total$ | 9.55 | 12.21 | 13.79 | 0.92 |
| MgO | 49.42 | 34.18 | 46.24 | 0.95 |
| CaO | <0.05 | 3.52 | 0.08 | 16.84 |
| $Na_2O$ | n.d. | 0.57 | 0.02 | 2.68 |
| $K_2O$ | n.d. | 0 | 0.01 | 0.02 |
| $TiO_2$ | n.d. | 0.07 | 0.01 | 0.04 |
| $P_2O_5$ | 0 | 0.01 | n.d. | n.d. |
| MnO | 0.14 | 0.19 | 0.25 | 0.05 |
| $Cr_2O_3$ | n.d. | n.d. | 0.01 | 0.01 |
| Total | 100.29 | 97.20 | 97.95 | 97.36 |
| Source | Jarosewich et al. 1980 | XRF | EMPA | EMPA |

| SAMPLE | basalt | | | | serpentinite |
|---|---|---|---|---|---|
| datatype | bulk rock | mineral (fsp) | mineral (cpx) | mineral (chl) | bulk rock |
| $SiO_2$ | 49.03 | 57.86 | 50.55 | 30.84 | 37.21 |
| $Al_2O_3$ | 15.39 | 27.08 | 1.6 | 17.37 | 4.97 |
| $FeO, total$ | 9.17 | 0.99 | 14.59 | 38.42 | 14.48 |
| MgO | 7.94 | 0.27 | 12.67 | 12.54 | 26.44 |
| CaO | 10.91 | 4.6 | 19.28 | 0.27 | 2.45 |
| $Na_2O$ | 2.86 | 5.35 | 0.31 | 0.16 | 0.04 |
| $K_2O$ | 0.23 | 3.76 | n.d. | 0.02 | 0.07 |
| $TiO_2$ | 1 | 0.06 | 0.62 | 0.05 | 0.51 |
| $P_2O_5$ | 0.14 | n.d. | n.d. | n.d. | 0.07 |
| MnO | 0.17 | 0.03 | 0.36 | 0.31 | 0.2 |
| $Cr_2O_3$ | n.d. | n.d. | 0.03 | 0.01 | n.d. |
| Total | 97.31 | 100.2 | 100.48 | 88.91 | 86.44 |
| Source | XRF | EMPA | EMPA | EMPA | XRF |

Table 3.1: Bulk rock and average mineral composition (oxides in wt%)

3.2. $H_2$ and $H_2S$ activity during reaction progress are also shown in table 3.2 and in fig. 3.3 along with the modeled stable mineral phase in the Fe-O-S system.

### 3.4.1   Olivine

San Carlos olivine ($Fo_{90}$; for composition see table 3.1) was allowed to react with fluid in a w/r of 83, leading to serpentinization with formation of brucite and magnetite (fig. 3.1a).

Olivine dissolution is visible from increasing dissolved Si shortly after the reaction started, and its slight decrease after 1 day coincides with serpentine formation. Mg, Ca, Fe and Al also decrease slightly during the reaction while Si and K remain roughly constant in the output fluid (fig. 3.2a); Ca and K are likely introduced to the system as trace amounts in the $Na_2S$-flakes. Fe is partially taken up in serpentine and in magnetite but some remains in the fluid; the presence of only 0.1 wt.% magnetite detected with the VSM coincides with roughly 5% serpentinization, consistent with the small amount of weight loss at the 600°C serpentine dehydration point in thermogravimetry.

During the run, an increasing amount of $H_2$ was released as olivine serpentinization proceeded through the oxidation of ferrous iron (Klein et al. 2009). Measured $H_2$ and $H_2S$ concentrations in the output fluid show that the system plots within the pyrrhotite field (green hexagrams in fig. 3.3). However, only upon cooling at the end of the experiment, a 6 mmol/kg decrease in S content is seen in the output fluid (fig. 3.2e), suggesting the possible formation of pyrrhotite. This drop in dissolved sulfur would coincide with 0.50 mmol S or 42.4 mg pyrrhotite; this is 0.5% of the sample weight, explaining its invisibility.

### 3.4.2   Troctolite

Troctolite from Hole 1309D (core 248R-2 15-17 cm, retrieved at 1193.6 mbsf) consisted of 25% anorthite-rich plagioclase and 75% olivine (table 3.1); the main reaction products detected using XRD are lizardite (70%), andradite (10%), saponite (10%) and magnetite (5%) (fig. 3.1b); no relic olivine or plagioclase was observed using electron microscopy. The experiment started with a w/r of 16.5.

An initial peak in the release of Al, Fe, Mg, Ca, K and Si showed simultaneous dissolution of olivine and plagioclase (fig. 3.2b), but their fluid concentrations decreased again upon incorporation in the main secondary minerals, Mg disappearing completely from the output fluid.

66

| exp. | olivine | | | troctolite | | | | | | |
|------|------|------|------|------|------|------|------|------|------|------|
| t(days) | **0** | **1** | **6** | **3** | **18** | **31** | **45** | **47** | | |
| $Al$ | 0.001 | 0.005 | 0.003 | 0.128 | 0.059 | 0.066 | 0.074 | 0.076 | | |
| $Ca$ | 0.007 | 0.006 | 0.002 | 0.003 | 0.001 | 0.001 | 0.001 | 0.001 | | |
| $Fe$ | 0.000 | 0.003 | 0.001 | 0.003 | 0.001 | 0.001 | 0.001 | 0.001 | | |
| $K$ | 0.014 | 0.014 | 0.016 | 0.107 | 0.045 | 0.044 | 0.045 | 0.054 | | |
| $Mg$ | 0.002 | 0.002 | 0.000 | 0.003 | 0.000 | 0.002 | 0.000 | -0.002 | | |
| $Mn$ | 0.000 | 0.000 | 0.000 | 0.000 | 0.000 | 0.000 | 0.000 | 0.000 | | |
| $Na$ | 8.940 | 40.223 | 39.887 | 43.074 | 53.479 | 51.586 | 52.532 | 51.758 | | |
| $P$ | 0.001 | 0.002 | 0.000 | 0.002 | -0.001 | 0.001 | 0.001 | -0.001 | | |
| $\Sigma S$ | n.d. | 20.804 | 22.988 | 27.819 | 24.821 | 24.667 | 25.346 | 25.819 | | |
| $Si$ | 0.021 | 0.055 | 0.051 | 0.573 | 0.144 | 0.114 | 0.105 | 0.107 | | |
| $Ti$ | 0.000 | 0.000 | 0.000 | 0.000 | 0.000 | 0.000 | 0.000 | 0.000 | | |
| $H_2(aq)$ | 62.864 | 134.555 | 1.801 | 13.725 | 2.662 | 35.328 | *15409.516* | | | |
| $H_2S(aq)$ | 1.145 | 0.261 | 1.793 | 0.008 | 0.032 | 0.904 | 0.358 | | | |
| **exp.** | basalt | | | | | | serpentinite | | | |
| **t(days)** | **0** | **15** | **28** | **36** | **50** | **62** | **1** | **4** | **7** | **11** |
| $Al$ | 0.827 | 0.083 | 0.086 | 0.094 | 0.076 | 0.110 | 0.073 | 0.066 | 0.065 | 0.064 |
| $Ca$ | 0.002 | 0.002 | 0.005 | 0.004 | 0.001 | 0.002 | 0.001 | 0.001 | 0.001 | 0.001 |
| $Fe$ | 0.010 | 0.003 | 0.003 | 0.000 | 0.000 | 0.000 | 0.001 | 0.002 | 0.002 | 0.002 |
| $K$ | 0.142 | 0.467 | 0.568 | 0.616 | 0.509 | 0.669 | 0.133 | 0.116 | 0.122 | 0.146 |
| $Mg$ | 0.005 | 0.005 | 0.014 | 0.002 | 0.002 | -0.001 | 0.000 | 0.000 | 0.000 | 0.000 |
| $Mn$ | 0.000 | 0.000 | 0.000 | 0.000 | 0.000 | 0.000 | 0.000 | 0.000 | 0.000 | 0.000 |
| $Na$ | 45.993 | 27.682 | 27.522 | 26.959 | 21.422 | 24.524 | 38.631 | 36.893 | 36.497 | 36.282 |
| $P$ | 0.003 | 0.001 | 0.001 | 0.001 | 0.004 | 0.001 | 0.001 | 0.001 | 0.000 | 0.000 |
| $\Sigma S$ | 22.657 | 24.821 | 25.377 | 20.741 | 17.711 | 19.350 | 18.763 | 26.242 | 23.708 | 21.019 |
| $Si$ | 4.254 | 9.875 | 9.977 | 9.925 | 7.410 | 8.650 | 1.027 | 1.103 | 1.138 | 1.169 |
| $Ti$ | 0.000 | 0.001 | 0.001 | 0.000 | 0.000 | 0.000 | 0.000 | 0.000 | 0.000 | 0.000 |
| $H_2(aq)$ | 0.002 | 0.057 | 7.724 | 0.038 | 0.044 | 0.045 | 2.542 | 2.875 | 1.819 | 2.040 |
| $H_2S(aq)$ | 0.654 | 0.482 | 0.429 | 0.429 | 0.432 | 0.435 | 0.678 | 0.635 | 0.415 | 0.460 |

Table 3.2: Measured fluid chemistry of all samples, including dissolved gas content, given in mmol/kg. The $H_2S(aq)$ is calculated from EQ3/6
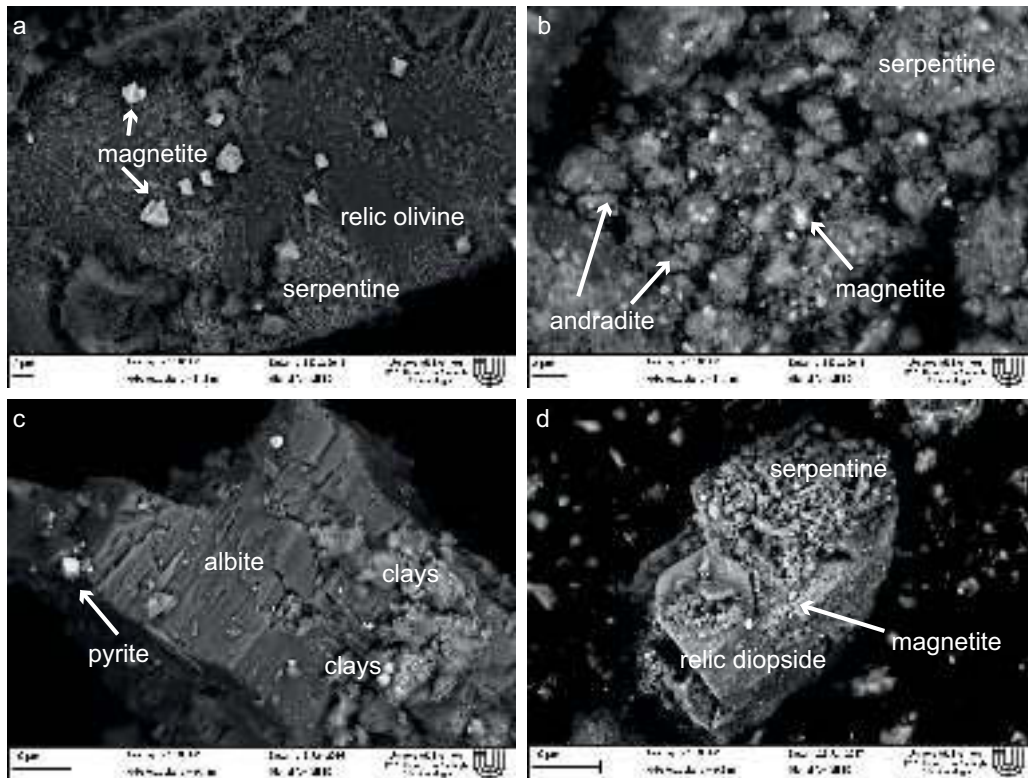
Figure 3.1: SEM images of reaction products of olivine (a), troctolite (b), basalt (c) and serpentinite (d) experiment. All samples show only superficial alteration; cuts through the grains only show primary minerals.

Na is not taken up in any phase (fig. 3.2e). The detection of minor anatase ($TiO_2$) and cristobalite ($SiO_2$) in XRD shows supersaturation and precipitation of these phases.

This experiment shows olivine hydration and thus releases large amounts of $H_2$ during the run. Consequently, the fluid compositions plot within the pyrrhotite and later the magnetite field (fig. 3.3, blue stars), but again pyrrhotite is not observed. Dissolved sulfide first went up to 28 mmol/kg and decreased during the run to 24 mmol/kg after 20 days (fig. 3.2e). After that, sulfur content in the fluid was seen to increase slightly again. This changing S-content during reaction could be interpreted as redissolution of pyrrhotite, releasing S and Fe to the solution. A simultaneous Fe peak suggests this as well but a later decrease after 30 days shows that Fe might be captured in magnetite and hydrogarnet (andradite).

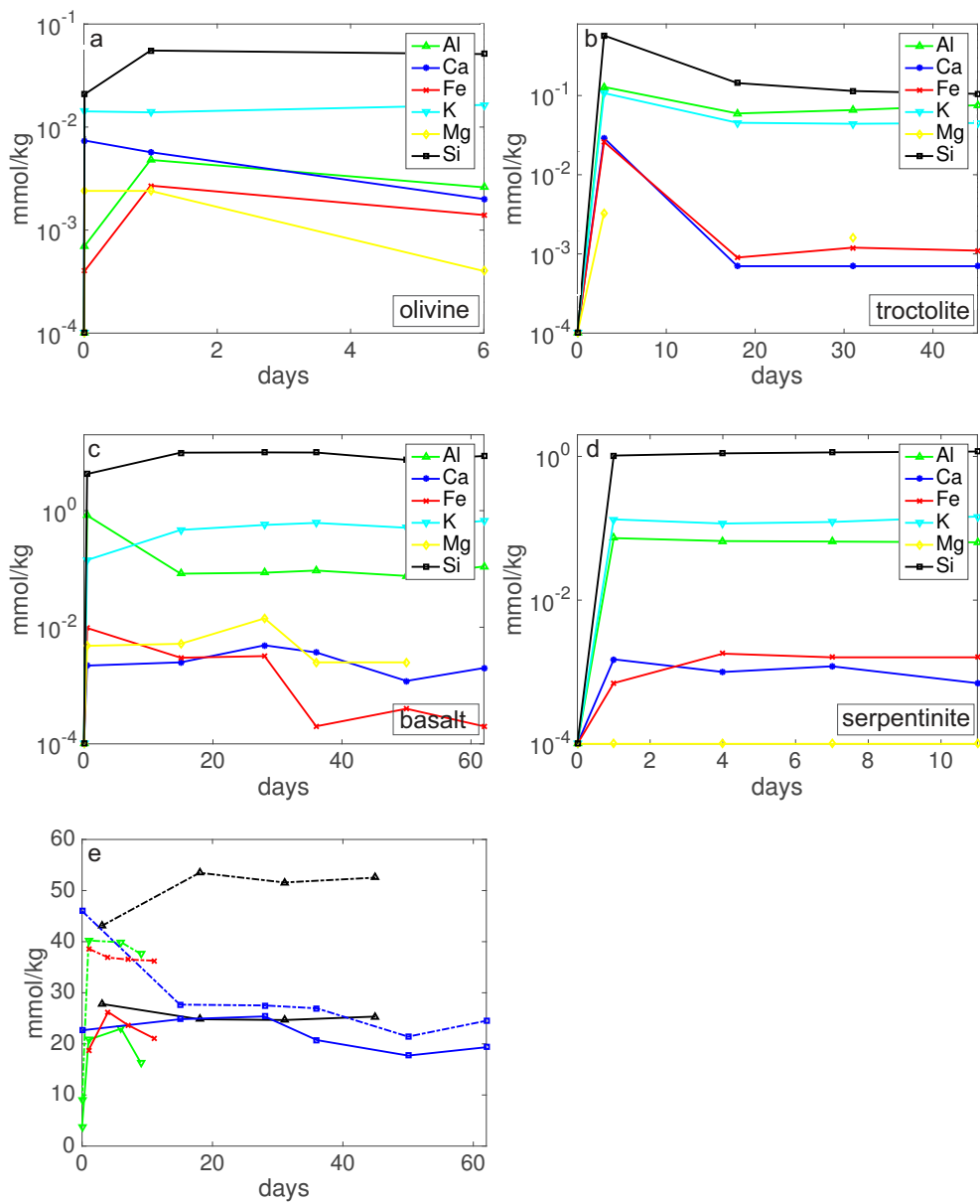Basalt Optical microscopy and XRD on the basaltic starting material were used to estimate

Figure 3.2: Major element concentrations in fluids from olivine (a), troctolite (b), basalt (c) and serpentinite (d) experiment; (e) shows the different S (solid line) and Na (dotted line) changes in all experiments, where olivine is represented by downward triangles, troctolite by upward triangles, basalt by squares and serpentinite by crosses. Note the similar trend for olivine and serpentinite.

the proportions of the major phases including plagioclase (58%), clinopyroxene (20%) and chlorite (15%) and minor phases such as apatite and spinel. The starting w/r was 14.

Fluid data show the rapid increased Si and Al at early stages of reaction, with some minor K and Ca (fig. 3.2c). This accounted for the dissolution of plagioclase. Aluminum contents in the fluid quickly decreased while Si remained elevated. One possible sink of Al may be the observed analcime ($NaAlSi_2O_6 \bullet H_2O$), as Na also decreased very quickly in the fluid (fig. 3.2e). A simultaneous drop in dissolved S and Fe recorded the formation of pyrite (see fig. 3.1c). Later decreasing Mg and Ca after 28 days (w/r of 13 at that point due to fluid extraction by sampling) could be captured in tremolite or epidote, but due to the small amounts of Ca released (total of 5 $\mu$mol in solution) this would not result in detectable amounts. Minerals found in the reacted specimen using XRD and electron microscopy include clinopyroxene (27%), plagioclase (55%), chlorite (9%), clays (8%), analcime and pyrite (both below detection limit in XRD). This shows that the reaction did not go to completion as relic pyroxene and feldspar phases make up more than half of the sample volume.

Measured gas concentrations are consistent with the formation of pyrite (black circles in fig. 3.3). During reaction, an increasing amount of $H_2$ was produced, slowly shifting the reaction into the pyrrhotite field. However, the last measurement point is again situated within the pyrite field and no evidence for the presence of pyrrhotite is found, either with SEM, VSM or XRD. Low temperature alteration phases like clays can be due to cooling artifacts before opening of the reaction cell.

### 3.4.3   Serpentinite

The reaction of serpentinite rock (roughly 80% serpentine minerals and minor magnetite, Ni-Co-sulfides and pyroxene and some olivine relics, based on optical and electron microscopy) with $H_2S$-rich fluid was expected to be relatively close to equilibrium, since the reaction of olivine with the same fluid resulted in serpentinite. The starting w/r was 93, as to have very oxidizing conditions and a large addition of sulfur to the system.

The resulting serpentine and magnetite product minerals (fig. 3.1d) seen in the SEM still closely resemble the starting material. Unlike in all other experiments, released major element ions in the fluid samples did not decrease with reaction progress. Instead, they remained constant or even increased slightly (see Si in fig. 3.2d). This is consistent with the idea that this reaction is
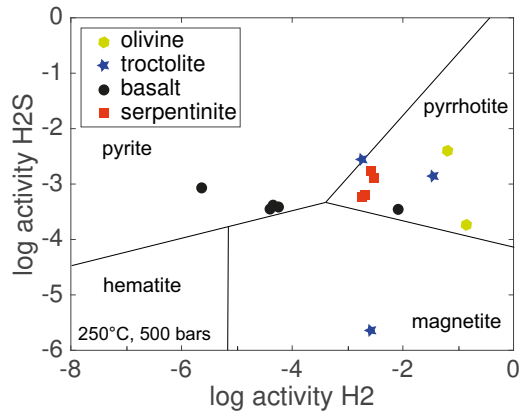
Figure 3.3: Mineral stability in the Fe-O-S system. Plotted points come from all experiments. For discussion, see text.

already close to equilibrium from the start. The only ions to decrease during the reaction (with 3 mmol/kg so 0.225 mmol in the actual amount of fluid present) are the ones added to the system, Na and S, and they are close to the amounts for the olivine experiment (fig. 3.2e). These elements are believed to go into the formation of clay minerals and a sulfide phase, respectively, when relic olivine and pyroxene are serpentinized (fig. 3.2d). However, once again no pyrrhotite is observed despite the dissolved gas concentrations showing favorable conditions for its formation (red squares in fig. 3.3). Instead, minor amounts of newly grown magnetite are present, along with Ni- and Co-bearing sulfide minerals. These minerals were not taken into consideration for the reaction path model due to their small quantities, but they might play a role in the behavior of sulfide in the reactive fluid through remobilization of S (not likely, since the dissolved sulfur content in this experiment is the lowest of all, see fig. 3.2e) or uptake of small amounts of sulfur. Noteworthy is also the dissolved iron content, which is 10 times lower than in the olivine experiment. This can either mean that the system is so close to equilibrium that no Fe is released into the fluid, or that all Fe is quickly captured as magnetite. There is no indication for new magnetite formation during the experimental run based on XRD and VSM measurements. However, magnetic susceptibility before and after heating the sample to 650°C (i.e., above the magnetite Curie temperature) showed that the solid reaction product had a stronger susceptibility signal after the heating cycle was complete. We have not examined the causes for the different behavior and a discussion of this

71

phenomenon is outside the scope of the paper. It is still interesting to note that Fe apparently was reactive in the sulfidation experiment, such that the formation of new magnetite during heating was more favorable or that magnetite properties (e.g., grain size, magnetic domain distribution and size) may have changed.

## 3.5   Discussion

### 3.5.1   Models vs. experiments

Reaction path models for all experimental runs are given in fig. 3.4a-d. For most runs the predicted reaction path does not comply with the observed mineral products (see also mineral overview provided in table 3.3) as these reactions did not go to completion. Differences between models and reality could also be due to the model taking into account mineral stability instead of mineral formation temperature, which would lead to the prediction of higher temperature minerals than actually observed. Most likely, however, is the inability of thermodynamic models to properly predict mineral kinetics and the detection limit of methods such as XRD and SEM. The discrepancies in the magnetite-pyrite-pyrrhotite-hematite system will be discussed below.

The olivine reaction path model in EQ3/6 predicts serpentinization, as is observed. At the beginning of the run, a high w/r favors the formation of pyrrhotite. This decreases the amount of $H_2S$, shifting the system towards magnetite stability. However, magnetite is not expected to form before Xi reaches 0.40 (fig. 3.4a), a point not reached in our experiment. Still, magnetite is observed while pyrrhotite is not, implying that S-activity in the fluid was too low to influence the far-from-equilibrium serpentinization reaction by the capture of Fe in a sulfide phase. Very low oxygen fugacities could explain this, as they make sulfide unstable (Frost 1985). This however would mean that the fluid samples should plot at lower $H_2S$-activity than they do now (fig. 3.3); our modeled speciation, where 1% of $\Sigma$ S was present as $H_2S$ may have been an overestimation.

The troctolite experiment also predicts the observed serpentinization and shows a halted increase in pyrrhotite when magnetite becomes stable at Xi=0.1 (fig. 3.4b). This could imply that initially, pyrrhotite was stable in the reaction cell, decreasing $H_2S$-activity (through uptake of S), moving the system towards the lower right corner of the fig. 3.3 where magnetite becomes the stable phase. Equilibrium between pyrrhotite and magnetite is therefore expected in the troctolite, but only the latter phase is observed; the grain size of relic pyrrhotite could be too

| | abbreviation | Xi=.05 Olivine | Xi=1 Troctolite | Xi=.1 Basalt | Xi=.01 Serpentinite |
|---|---|---|---|---|---|
| serpentine | srp | 18.93 | 29.09 | | 16.25 |
| brucite | brc | 4.64 | | | |
| magnetite | mag | 6.42 | 11.7 | | 4.66 |
| pyrite | py | | | 5.97 | |
| pyrrhotite | po | 2.47 | 3.25 | 4.85 | |
| epidote | ep | | | 19.11 | |
| chlorite | chl | | 49.95 | 36.7 | 24.94 |
| tremolite | tr | | 69.21 | 49.47 | 32.23 |
| phlogopite | phl | | | 24.71 | 16.01 |
| analcime | anl | | | 3.72 | |
| andradite | adr | | 28.99 | 24.93 | 9.15 |
| microcline | mc | | | 4.63 | |

predicted if Xi goes to 1

seen

both

Table 3.3: Diagram with expected and observed mineralogy. The diagram shows which minerals are expected when the reaction goes to completion (blue), which are actually observed (yellow) and which are both modeled and observed (green). The numbers represent saturation indices for predicted minerals at the predicted final reaction progress (Xi mentioned above each column) of each run

small. Another possibility is that andradite stability overlies the magnetite and part of the pyrrhotite stability field when some Si is added to the system (fig. 3.5) and it may thus have inhibited further pyrrhotite (and magnetite) formation. The basalt reaction path model (fig. 3.4c) predicts the observed formation of pyrite; the amount of formed sulfide (<28 mg) is however too small to be quantified using XRD. It also predicts the observed analcime; both pyrite and analcime disappear early in the reaction path, implying that the experiment was halted before this point (Xi=0.03) was reached.

The serpentinite experiment did not progress far since the fluid quickly reached equilibrium with the rock (fig. 3.2d). This means that we should compare the reaction path model at Xi=0.01 with our observations, where only serpentine, magnetite and possibly some small amounts of tremolite are predicted (fig. 3.4d). Except for the tremolite, this is in line with our observations. It is worth to note that, despite the high amount of sulfur added, no sulfide phase is predicted,

even though the activity-activity plot shows the reaction within the pyrrhotite stability field. This might be a similar overestimation of the activity of $H_2S$ as in the olivine run, as pyrrhotite is not predicted in the reaction path model, or pyrrhotite formation kinetics may have been sluggish. We did not increase the w/r further however, as this would leave us with too few solids to analyze.

Despite all predicted S-bearing phases using induced $H_2$ and $H_2S$ activity, only basalt succeeded in the net capture of sulfide. $H_2S$-activity in all the other runs must therefore have been lower than estimated in the EQ3/6 software. We deduced the percentage of total sulfur present as $H_2S$ from speciation calculations on the 250°C reactive fluid using EQ6 software. These highly pH dependent speciation calculations may cause a slight error since starting fluid pH at 25°C could not be measured, only inferred from the added $Na_2S$ as dissolution and equilibration with $Na_2S$ took place during heating and start of the water-rock interaction.

### 3.5.2 Silica activity

In those experiments including serpentinization, dissolved silica content was of great importance. Pure olivine serpentinization occurs under low Si-activity and will result in the additional formation of brucite while higher Si-activity (for example through the initial presence of pyroxenes) leads to serpentine as only reaction product (Frost and Beard 2007). The dissolving minerals in the troctolite experiment increased the Si-content in the system and the large amount of andradite (instead of other Ca-silicates such as Si-richer tremolite or chlorite) showed that this is a factor that should not be ignored. Besides increased Si and Ca concentration (compare fig. 3.2a and 3.2b), pH should be above 9 and silica activity should not exceed 2.5 mmol/L because Ca-Fe silicates besides andradite might become stable (Beard and Hopkinson 2000). Andradite is only observed in the troctolite experiment and may impede sulfide formation, as it decreases the availability of Fe for sulfides.

To analyze the stability of andradite, a diagram similar to fig. 3.3 can be plotted that includes ions such as Ca, Si, Al and Mg. After suppressing non-observed phases (everything except plagioclase, saponite, andradite, serpentine, chlorite, brucite, olivine and magnetite), andradite plots right where the hematite, magnetite and part of the pyrrhotite stability field are in the absence of silica (fig. 3.5). The presence of both magnetite and andradite implies that the system has experienced a shift in Si-activity, which is confirmed by fig. 3.2b and implies that magnetite must postdate andradite. We already know from fluid measurements (fig. 3.2e) that
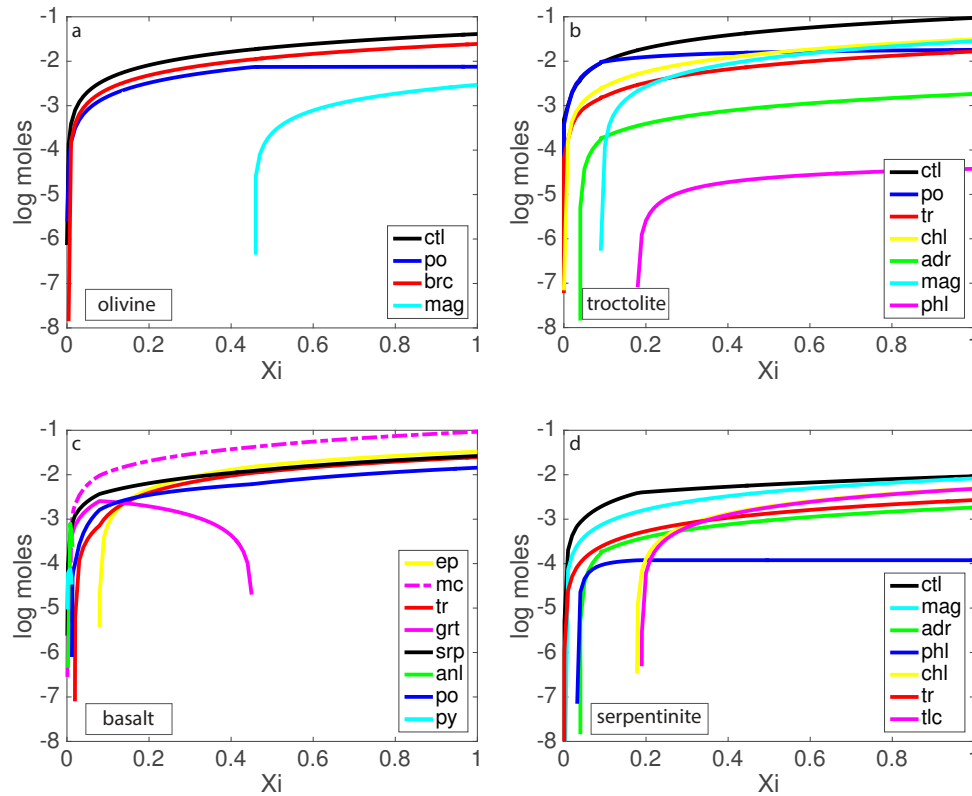
74

Figure 3.4: EQ3/6-based reaction path models for olivine (a), troctolite (b), basalt (c) and serpentinite (d) reaction with hydrothermal fluid showing the expected mineral assemblage with reaction progress. For discussion, see text.

dissolved sulfur content also evolves: the small initial decreasing S-content in the fluid can be explained by formation of pyrrhotite while a later re-dissolution is shown by sulfur release back into the fluid. Dissolved $H_2$ and $H_2S$ contents (fig. 3.3) show that this trend is probably due to an increased $H_2$-production upon olivine serpentinization. The Fe released from pyrrhotite re-dissolution was assumed to be captured in magnetite. However, the elevated Si content in this fluid also allows the formation of an iron-silicate phase: andradite. One could argue that by this, magnetite crystallization is partially inhibited until Si-activity dropped due to precipitation.

The presence of andradite related to serpentinization is discussed by several authors (e.g. Frost 1985; Bideau et al. 1991; Früh-Green et al. 1996; Plümper et al. 2014; Ghosh et al. 2017). It is even observed in Hole 1309D where our troctolite starting material was retrieved, although at

different depth (Frost et al. 2008). They reported garnet growth in veins, surrounded by prehnite on the contact with anorthite, implying that the garnet formed below 350°C by simple 'desilicification' of plagioclase instead of Ca-metasomatism. A similar process is expected in the troctolite experiment, where andradite results from dissolution of plagioclase and release of Si instead of addition of Ca to the system. Aluminum can be taken out of solution by chlorite precipitation, but elevated Al contents and the limited amount of expected chlorite show that this did not occur. This could be related to a batch experiment's limited ability to mimic a natural flow-through system. Instead, saponite is observed as a possible Al-bearing phase, but since this clay mineral is metastable, the presence of chlorite is still suspected.

Likewise, in the basalt experiment chlorite is predicted to form but could not be detected. Chlorite is known as a phase that is difficult to synthesize directly from hydrothermal fluids (e.g., Small et al. 1992); hence, sluggish kinetics can account for its absence. Other silicate phases (such as epidote or microcline) are predicted to form along the reaction paths, but empirical data indicate that higher temperatures are often required for their formation (e.g., Bird and Spieler 2004). Another possibility is that chlorite has been overlooked in the measurements. Indeed, the mass of chlorite estimated from the amount of Ca released to the fluid and assuming that it takes up the left-behind Al is <0.1 g (i.e., <2 wt.% of solids). We did find clay minerals in the solid reaction products this run, which probably formed metastably.
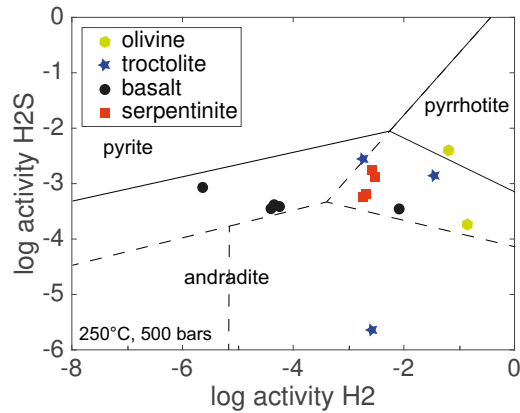


Figure 3.5: Andradite stability field overlaps with magnetite, hematite and parts of the pyrrhotite and pyrite field. Si-addition to the system has severe results in reaction products.

76

### 3.5.3  Sulfide stability in serpentinites

Water-rock ratio (and effectively oxygen fugacity) is crucial to sulfide stability (Frost 1985; Alt and Shanks 1998). High ratios result in relatively oxidizing conditions and allow for pyrite and high sulfur-phases. These conditions are often related to basalt-hosted hydrothermal systems or to carbonated serpentinites, where the system is buffered at a higher oxygen fugacity than pure serpentinization through equilibrium with magnesite. Lower water-rock ratios result in high metal sulfides or even native metals. Examples of both types can be found at the Iberia Margin, where Beard and Hopkinson (2000) discovered pentlandite, heazlewoodite and awaruite in deeper sections, and andradite, magnesite and even hematite close to fracture zones.

It is noteworthy that our serpentinite experiment had the highest w/r of all but shows no signs of sulfides. This must mean that the total sulfur input was too low in this reducing system to allow for sulfide formation. Therefore, water-rock ratio is only deterministic for sulfide formation as long as it puts the system at a higher oxidation state. Instead, magnetite is observed in this run, which shows that the activity of $H_2S$ was again lower than predicted by the model. This same process occurred in the olivine experiment, where $fO_2$ remains low because of $H_2$-production and all sulfur stays in solution as $HS^-$, not precipitating any sulfides but magnetite instead (cf. Alt and Shanks 1998). The basalt experiment on the other hand had the lowest w/r and was the easiest to sulfidize, even though in absolute numbers, the least sulfur was added to this system. This shows that S-activity is more important than the absolute S-content, and it shows the readiness of basalt to sulfidize compared to the other tested lithologies, which were more reducing and produced more $H_2$ during reaction with hydrothermal fluid (fig. 3.3). In natural systems, most large sulfide deposits can also be found in mafic rock (TAG, Snake Pit, Lucky Strike), as opposed to ultramafic rock types.

### 3.5.4  Comparison to natural samples: implications for the formation of massive sulfide deposits in different lithologies

To compare different rock types under similar reaction conditions and apply the results from above on a natural system, we will compare them to the Atlantis Massif (30°N, MAR) where serpentinites, gabbros and troctolites have been discovered close to an actively venting system (Delacour et al. 2008a, 2008b). The southern wall is located below the Lost City Hydrothermal

Field and shows more oxidizing conditions; serpentinized peridotite and gabbros in this area both display isotopically heavy but low total sulfur contents (Delacour et al. 2008a), often present as sulfate. This implies leaching of magmatic sulfides and oxidation of the remnant sulfide minerals, resulting in sulfate and some pyrite. At the central dome, less seawater influence is observed (Delacour et al. 2008b). Here, gabbro and troctolite samples at depth showed mainly primary magmatic sulfides while serpentinized samples closer to the seafloor showed higher sulfur contents and a mixed isotopic signature between magmatic and seawater. This is thought to come from seawater-gabbro interaction, and subsequent serpentinization with this fluid.

Unfortunately, this example cannot provide more insight in troctolite sulfidation, because only leaching of magmatic sulfides has been observed. However, the gabbroic section in the southern wall is more prone to pyrite formation than serpentinite, even though the latter formed under relatively high $fO_2$ conditions. The lack of sulfides in the olivine and serpentinite experiments compares nicely to this observation. Low-S Ni-Cu sulfides are observed in the serpentinite experiment, but because the minerals seem to be deeply inbedded in the serpentinite they are thought to result from serpentinization and not the sulfidation experiment. Extra proof for this is the absence of any sulfide phase in the olivine experiment; the relatively low sulfur activity inhibited formation of pyrrhotite and favored magnetite instead.

## 3.6    Summary

Reaction of olivine, troctolite, basalt and serpentinite with a fluid bearing 20 mmol/kg $H_2S$ at 250°C and 400 bars did not always result in the expected sulfidation of rock. The olivine experiment showed partial serpentinization (roughly 5%) with the formation of magnetite instead of the thermodynamically predicted pyrrhotite; this might relate to the sluggish formation kinetics of the latter phase. The serpentinite experimental run was close to equilibrium with the fluid from the start and only showed minor growth of magnetite. The troctolite resulted in full hydration of olivine, while all plagioclase was transformed into andradite and clays. Once again, the presence of predicted pyrrhotite contradicted observations. A dip in sulfur content in the fluid and a later sulfur release suggests that pyrrhotite might have been present temporarily, being replaced later on by magnetite.

Only in the basalt experiment a sulfide phase was formed. Euhedral pyrite crystals were detected on the dissolving plagioclase and pyroxene minerals, as well as the Na-zeolite analcime.

Although this run had the lowest w/r, its oxidized nature allowed for pyrite to precipitate. The other lithologies imposed conditions too reducing for pyrite to form. The activity of $SiO_2$ and $H_2S$ proved very important for the sulfidation of the system. In the troctolite experiment, andradite stability overlapped with magnetite and pyrrhotite, possibly inhibiting their formation. The high amount of added sulfur did not counteract this process. Oxygen fugacity also proved to be important, as the more oxidizing basalt was the only one to produce pyrite despite the higher amounts of $H_2S$ added to the other lithologies. This may be explained by higher sulfur fugacity under oxidizing conditions being more important than the total amount of dissolved sulfide.

This study presents the first evidence for replacive pyrite formation, which is observed in hydrothermal stockwork zones (e.g., in the TAG active hydrothermal system).

Basaltic rock compositions appear to have a higher affinity for sulfidization that more olivine-rich lithologies. Further studies are needed to explain the apparent sulfidization of serpentinized peridotite by fluids with low sulfide contents at the Rainbow hydrothermal system.

## 3.7 Acknowledgements

## 3.8 References

Adamides, N.G., 2010. Mafic-dominated volcanogenic sulphide deposits in the Troodos ophiolite, Cyprus Part 2 –A review of generic models and guides for exploration. Applied Earth Science 119(4), 193-204.

Alt, J.C., Shanks III, W.C., 1998. Sulfur in serpentinized oceanic peridotites: Serpentinization processes and microbial sulfate reduction. Journal of Geophysical Research 103(B5), 9917-9929.

Alt, J.C., Shanks III, W.C., 2003. Serpentinization of abyssal peridotites from the MARK area, Mid-Atlantic Ridge: Sulfur geochemistry and reaction modeling. Geochimica et Cosmochimica Acta 64(4), 641-653.

Alt, J.C., Shanks III, W.C., Bach, W., Paulick, H., Garrido, C.J., Beaudoin, G., 2007. Hydrothermal alteration and microbial sulfate reduction in peridotite and gabbro exposed by detachment faulting at the Mid-Atlantic Ridge, $15°20'N$ (ODP Leg 209): A sulfur and oxygen isotope study. Geochemistry, Geophysics, Geosystems 8(8), Q08002. http://dx.doi.org/10.1029/2007GC001617

Alt, J.C., Schwarzenbach, E.M., Früh-Green, G.L., Shanks III, W.C., Bernasconi, S.M., Garrido, C.J., Crispini, L., Gaggero, L., Padrón-Navarta, J.A., Marchesi, C., 2013. The role of serpentinites in cycling of carbon and sulfur: Seafloor serpentiniation and subduction metamorphism. Lithos 178, 40-54.

Bach, W., Garrido, C.J., Paulick, H., Harvey, J., Rosner, M., 2004a. Seawater-peridotite interactions: First insights from ODP Leg 209, MAR 15N. Geochemistry, Geophysics, Geosystems 5(9), Q09F26. http://dx.doi.org/10.1029/2004GC000744

Beard, J.S., Hopkinsons, L., 2000. A fossil, serpentinization-related hydrothermal vent, Ocean Drilling Program Leg 173, Site 1068 (Iberia Abyssal Plain): Some aspects of mineral and fluid chemistry. Journal of Geophysical Research 105(B7), 16527-16539.

Bideau, D., Hebert, R., Hekinian, R., Cannat, M., 1991. Metamorphism of Deep-Seated Rocks from The Garrett Ultrafast Transform (East Pacific Rise Near $13°25'S$). Journal of Geophysical Research 96(B6), 10079-10099.

Bird, D.K., Spieler, A.R., 2004. Epidote in geothermal systems, in: Liebscher, A., Frantz, G. (Eds.), Epidotes. Reviews in Minealogy and Geochemistry, Mineralogical Society of America, Geochemical Society 56, pp. 235-300.

Bischoff, J.L., Dickson, F.W., 1975. Seawater-basalt interaction at $200°C$ and 500 bars: implications for origin of sea-floor heavy-metal deposits and regulation of seawater chemistry. Earth and Planetary Science Letters 25, 385-397.

Czamanske, G.K., Moore, J.G., 1977. Composition and phase chemistry of sulfide globules in basalt from the Mid-Atlantic Ridge rift valley near $37°N$ lat. Geological Society of America

bulletin 88, 587-599.

Delacour, A., Früh-Green, G.L., Bernasconi, S.M., Kelley, D.S., 2008a. Sulfur in peridotites and gabbros at Lost City (30°N, MAR): Implications for hydrothermal alteration and microbial activity during serpentinization. Geochimica et Cosmochimica Acta 72, 5090-5110.

Delacour, A., Früh-Green, G.L., Bernasconi, S.M., 2008b. Sulfur mineralogy and geochemistry of serpentinites and gabbros of the Atlantis Massif (IODP Site U1309). Geochimica et Cosmochimica Acta 72, 5111-5127.

Frost, B.R., 1985. On the Stability of Sulfides, Oxides, and Native Metals in Serpentinite. Journal of Petrology 26(1), 31-63.

Frost, B.R., Beard, J.S., 2007. On Silica Activity and Serpentinization. Journal of Petrology 48, 1351-1368.

Frost, B.R., Beard, J.S., McCaig, A., Condliffe, E., 2008. The Formation of Micro-Rodingites from IODP Hole U1309D: Key To Understanding the Process of Serpentinization. Journal of Petrology 49, 1579-1588.

Früh-Green, G.L., Plas, A., Lécuyer, C., 1996. Petrologic and stable isotope constraints on hydrothermal alteration and serpentinization of the EPR shallow mantle at Hess Deep (Site 895), in: Mével, C., Gillis, K.M., Allen, J.F., Meyer, P.S. (Eds.), Proceedings of the Ocean Drilling Program. Scientific Results, Vol. 147.

German, C.R., Petersen, S., Hannington, M.D., 2016. Hydrothermal exploration of mid-ocean ridges: Where might the largest sulfide deposits be forming? Chemical Geology 420, 114-126.

Ghosh, B., Morishita, T., Ray, J., Tamura, A., Mizukami, T., Soda, Y., Ovung, T.N., 2017. A new occurrence of titanian (hydro)andradite from the Nagaland ophiolite, India: Implications for element mobility in hydrothermal environments. Chemical Geology 457, 47-60.

Godard, M., Luquot, L., Andreani, M., Gouze, P., 2013. Incipient hydration of mantle lithosphere at ridges: A reactive-percolation experiment. Earth and Planetary Science Letters 371-372, 92-102.

Hannington, M.D., Galley, A.G., Herzig, P.M., Petersen, S., 1998. Comparison of the TAG mound and the stockwork complex with Cyprus-type massive sulfide deposits, in: Herzig, P.M., Humphris, S.E., Miller, D.J., Zierenberg, R.A. (Eds.), Proceedings of the Ocean Drilling Program. Scientific Results, Vol. 158.

Humphris, S.E., Herzig, P.M., Miller, D.J., Alt, J.C., Becker, K., Brown, D., Brügmann, G.,

Chiba, H., Fouquet, Y., Gemmell, J.B., Guerin, G., Hannington, M.D., Holm, N.G., Honnorez, J.J., Itturino, G.J., Knott, R., Ludwig, R., Nakamura, K., Petersen, S., Reysenbach, A-L., Rona, P.A., Smith, S., Sturz, A.A., Tivey, M.K., Zhao, X, 1995. The internal structure of an active sea-floor massive sulphide deposit. Nature 377, 713-716.

Johnson, J.W., Oelkers, E.H., Helgeson, H.C., 1992. Supcrt92: A software package for calculating the standard molal thermodynamic properties of minerals, gases, aqueous species, and reactions from 1 to 5000 bar and 0 to 1000°C. Computers & Geoscience 18(7), 899-947.

Klein, F., Bach, W., 2009. Fe-Ni-Co-O-S Phase Relations in Peridotite-Seawater Interactions. Journal of Petrology 50(1), 37-59.

Klein, F., Bach, W., Jöns, N., McCollom, T., Moskowitz, B., Berquó, T., 2009. Iron partitioning and hydrogen generation during serpentinization of abyssal peridotites from 15°N on the Mid-Atlantic Ridge. Geochimica et Cosmochimica Acta 73, 6868-6803.

Klein, F., Grozeva, N.G., Seewald, J.S., McCollum, T.M., Humphris, S.E., Berquó, T.S., Kahl, W.-A., 2015. Experimental Constrains on Fluid-Rock Reactions during incipients Serpentinization of Harzburgite. American Mineralogist 100(4), 991-1002.

Marques, A.F.A., Barriga, F., Chavagnac, V., Fouquet, Y., 2006. Mineralogy, geochemistry, and Nd isotope composition of the Rainbow hydrothermal field, Mid-Atlantic Ridge. Mineral Deposita 41, 52-67.

Marques, A.F.A., Barriga, F.J.A.S., Scott, S.D., 2007. Sulfide mineralization in an ultramafic-rock hosted seafloor hydrothermal system: From serpentinization to the formation of Cu –Zn –(Co)-rich massive sulfides. Marine Geology 245, 20-39.

Melchert, B., Devey, C.W., German, C.R., Lackschewitz, K.S., Seifert, R., Walter, M., Mertens, C., Yoerger, D.R., Baker, E.T., Paulick, H., Nakamura, K., 2008. First evidence for high-temperature ″off-axis″ venting of deep crustal heat: the Nibelungen hydrothermal field, Southern Mid-Atlantic Ridge. Earth and Planetary Science Letters 275, 61-69.

Mottl, M.J., Holland, H.D., 1978. Chemical exchange during hydrothermal alteration of basalt by seawater: I. Experimental results for major and minor components of seawater. Geochimica et Cosmochimica Acta 42, 1103-1115.

Mottl, M.J., Holland, H.D., Corr, R.S., 1979. Chemical exchange during hydrothermal alteration of basalt by seawater: II. Experimental results for Fe, Mn and sulfur species. Geochimica et Cosmochimica Acta 43, 869-884.

Peach, C.L., Mathez E.A., Keays, R.R., 1990. Sulfide melt silicate melt distribution coefficients for noble-metals and other chalcophile elements as deduced from MORB –implications for partial melting. Geochimica et Cosmochimica Acta 54, 3379-3389.

Petersen, S., Kuhn, K., Kuhn, T., Augustin, N., Hékinian, R., Franz, L., Borowski, C., 2009. The geological setting of the ultramafic-hosted Logatchev hydrothermal field (14°45′N, Mid-Atlantic Ridge) and its influence on massive sulfide formation. Lithos 112, 40-56.

Plümper, O., Beinlich, A., Bach, W., Janots, E., Austrheim, A., 2014. Garnets within geode-like serpentinite veins: Implications for element transport, hydrogen production and life-supporting environment formation. Geochimica et Cosmochimica Acta 141, 454-471.

Schwarzenbach, E.M., Früh-Green, G.L., Bernasconi, S.M., Alt, J.C., Shanks III, W.C., Gaggero, L., Crispini, L., 2012. Sulfur geochemistry of peridotite-hosted hydrothermal systems: Comparing the Ligurian ophiolites with oceanic serpentinites. Geochimica et Cosmochimica Acta 91, 283-305.

Seewald, J.S., Seyfried, W.E., 1990. The effect of temperature on metal mobility in subseafloor hydrothermal systems: constraints from basalt alteration experiments. Earth and Planetary Science Letters 101, 388-403.

Seyfried Jr., W.E., Dibble Jr., W.E., 1980. Seawater-peridotite interaction at 300°C and 500 bars: implications for the origin of oceanic serpentinites. Geochimica et Cosmochimica Acta 44, 309-321.

Shanks II, W.C., Bischoff, J.L., Rosenbauer, R.J., 1981. Seawater sulfate reduction and sulfur isotope fractionation in basaltic systems: Interaction of seawater with fayalite and magnetite at 200-350°C. Geochimica et Cosmochimica Acta 45(11), 1977-1995.

Shibuya, T., Yoshizaki, M., Masaki, Y., Suzuki, K., Takai, K., Russell, M.J., 2013. Reactions between basalt and $CO_2$-rich seawater at 250 and 350°C, 500 bars: Implications for the $CO_2$ sequestration into the modern oceanic crust and the composition of hydrothermal vent fluid in the $CO_2$-rich early ocean. Chemical Geology 359, 1-9.

Sleep, N.H., Meibom, A., Fridriksson, Th., Coleman, R.G., Bird, D.K., 2004. $H_2$-rich fluids from serpentinization: Geochemical and biotic implications. Proceedings of the National Academy of Sciences of the United States of America 101(35), 12818-12823.

Small, J.S., Hamilton, D.L., Habesch, S., 1992. Experimental simulation of clay precipitation within reservoir sandstones 1: Techniques and examples. Journal of Sedimentary Research

62(3), 508-519.

Smith, D.K., Escartin, J., Schouten, H., Cann, J.R., 2008. Fault rotation and core complex formation: significant processes in seafloor formation at slow-spreading mid-ocean ridges (Mid-Atlantic Ridge, 13-15°N). Geochemistry, Geophysics, Geosystems 9(3), Q03003. http://dx.doi.org/10.1029/2007GC001699.

Wolery, T.W., Jarek, R.L., 2003. Software User′s Manual EQ3/6, Version 8.0, Sandia National Laboratories. Albuquerque, NM, USA.

Zierenberg, R.A., Shanks III, W.C., Seyfried Jr., W.E., Koski, R.A., Strickler, M.D., 1988. Mineralization, Alteration, and Hydrothermal Metamorphism of the Ophiolite-Hosted Turner-Albright Sulfide Deposit, Southwestern Oregon. Journal of Geophysical Research 93(B5), 4657-4674.

# 4 Anhydrite precipitation and iron redistribution in low temperature flow-through experiments representing marine hydrothermal recharge zones

*Catharina Los (1), Wolf-Achim Kahl (1), Wolfgang Bach (1,2)*

Contact: los@uni-bremen.de, tel. 0049 421 218 65406

(1) Geosciences Department, University of Bremen, Klagenfurter Str. 2, 28359 Bremen, Germany

(2) MARUM, Center for Marine and Environmental Sciences, Leobener Str. 28359 Bremen, Germany

## 4.1 Abstract

Hydrothermal circulation in the oceanic lithosphere results in mineral alteration. Anhydrite is an important secondary mineral in the recharge zones of these hydrothermal systems. It forms when infiltrating seawater becomes heated and reacts with the Ca released from the host rock. Anhydrite often precipitates as pore fill and as veins, showing its potential to affect the porosity and permeability of the shallow crust. To mimic the off-axis formation of anhydrite, we performed flow-through experiments where we injected a sulphate solution in pre-fractured basalt at temperatures between 95 and 140°C. Below 110°C, no anhydrite was detected although the fluid was supersaturated in the mineral. Instead, only hematite, clays and zeolites were observed.

Above 120°C, anhydrite was present but in smaller amounts than could be expected from thermodynamic models. In these runs, many different Fe-phases such as hematite, magnetite and pyrite were observed and show that Fe-activity at these low temperatures was high. The presence of secondary pyrite is of particular interest as it must result from thermochemical sulphate reduction, which is thought to occur only at much higher temperatures. This process may imply that the potential energy for microbial life in ridge flank systems is much lower than previously thought.

The used experimental setup enabled us to make scans of the ongoing reaction. Although the mineral precipitates were too small to be picked up, the scans could show small shifts between rock fragments during the run. This shows that structural and chemical analysis can be combined using these X-ray transparent flow-through cells, which is a large step forward in experimental work.

## 4.2   Introduction

Anhydrite is a common secondary mineral in seawater-rock interactions. The precipitation of anhydrite ($CaSO_4$) directly from seawater at temperatures >150°C is a well-known phenomenon (Bischoff and Seyfried 1978). Others reported anhydrite precipitation upon mixing of seawater and hydrothermal fluids; anhydrite formed above discharging hydrothermal fluids as chimneys (Haymon 1983). Mixing with hydrothermal fluids can also result in anhydrite formation in the sub-seafloor (Chiba et al. 1998; Bach et al. 2003; Kuhn et al. 2003; Schmidt et al. 2010 and many others) where it cements breccia fragments or occurs as veins (Humphris 1998). Another mode of anhydrite precipitation observed in the oceanic lithosphere is during recharge. The mineral forms in the crust after seawater passed through a shallow crustal section, heating the fluid and enriching it in Ca. In this case, the sulphate mineral can precipitate at lower temperatures than in seawater as solubility values will be different due to changes in fluid chemistry; Teagle et al. (1998) noted anhydrite precipitation at temperatures as low as 50-70°C at ODP Hole 504B. Not all dissolved sulphate precipitates as anhydrite; in fact, calculations by Teagle et al. (1998) and Alt et al. (2003) show that a large part must leave the crust after circulation, possibly through diffuse venting. At inactive hydrothermal systems the mineral can also be absent due to its retrograde solubility. Anhydrite therefore plays a large role in controlling the permeability of the shallow oceanic crust and understanding its behaviour close to its formation and dissolution

temperature is important.

The precipitation of anhydrite is not the only result of seawater recharge. High porosity in the upper crustal section leads to open system circulation with high w/r (>50, Seyfried and Mottl 1982) in which basalt can dissolve. Released Si, Fe and alkali ions precipitate in layered clays such as nontronite (Alt and Honnorez 1984), as well as Fe-oxyhydroxides (goethite, hematite etc) and celadonite (Andrews 1980) under low temperature oxidizing conditions (Seyfried and Bischoff 1979; Staudigel et al. 1996). During this process, the rock becomes enriched in $Fe^{3+}$ and in total Fe, as a result of the oxidation of leached ferrous iron and subsequent precipitation of it, seen in Fe-oxyhydroxides (Andrews 1977; Alt 1995). At greater depths circulation is limited due to decreasing permeability, leading to more reducing conditions with saponite and zeolites like analcime and eventually sulphides in the non-oxidative diagenesis zone (Andrews 1977), where no sulphate is observed any more.

Although anhydrite formation is known to be a rapid process at high temperatures related to seafloor hydrothermal discharge zones (Haymon 1983), the time scale of precipitation in shallow hydrothermal systems such as the Reykjanes field in Iceland is likely much longer. The present study aims to understand and mimic this low temperature (<150°C) formation of anhydrite in a basaltic substrate. To facilitate precipitation we have used pre-fractured cores, in which we injected a calcium sulphate bearing solution at a very low flow rate (0.01 mL/min) at a temperature range of 100-150°C, typical for off-axis circulation (Lister 1982). We measured outlet fluid compositions and monitored precipitation by $\mu$-tomography. Besides anhydrite, the enrichment and different occurrences of Fe are another topic of interest in this communication.

## 4.3   Methods

### 4.3.1   Flow-through setup

A pre-fractured basalt core (diameter of 1.8 cm and core length of 2.5-3.0 cm) was surrounded by a FEP (fluoroethylenepropylene) shrink sleeve and placed within a PEEK (polyetheretherketone) reaction cell (fig. 4.1), which can resist temperatures up to 150°C and is X-ray transparent. The sample had PEEK plugs at the bottom and the top to inhibit flow between the core and the shrink sleeve. Fluid was only allowed to enter the core through one hole in the middle of the plug, connected to a PEEK tube (diameter of 1.80 mm) that was attached to a pump with reactive

fluid (input) and could only leave the core through tubing led towards the waste bin (output). Pressure regulators were installed on both sides. The core was flushed with the reaction solution at 25°C for a day to wet the pores and main fracture.
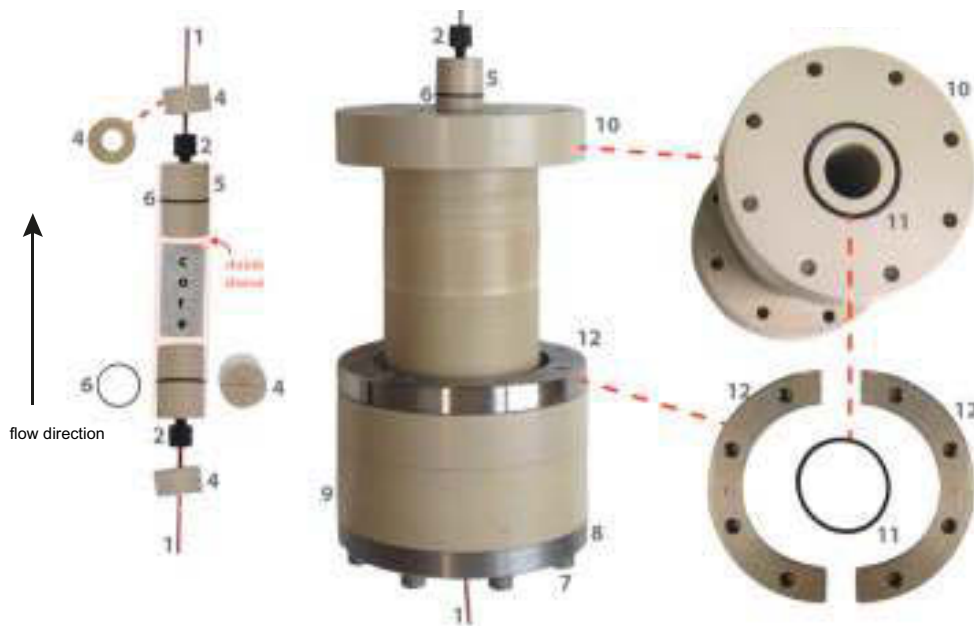


Figure 4.1: Setup of PEEK cell and sample orientation (from: Kahl et al. 2016, supplementary material).

The experiment was initiated by placing the reaction cell in the oven and heating the reaction fluid and basalt core to 95 (a), 95-110 (b), 120 (c) or 140 (d)°C. For experiment (b) we increased the temperature from 95°C (run time of 15 days) to 110°C (run time of 5 days) after the analysis of solids in run (a) showed no precipitation. At 110°C however the set-up was rapidly clogged and we were forced to use a lower concentration inlet solution at higher temperature runs. Runs (a) and (b) were therefore performed with a starting solution that contained 14.5 mmol dissolved gypsum/L while (c) and (d) had starting fluids with 10.2 mmol/L. This change was made in order to stay just below the saturation point of anhydrite, which would potentially clog the inlet tubing upon heating of the fluid. The fluid was allowed to equilibrate with air, and flow rate was set at 0.010 mL/min.

During the run front- and back-pressure sensors monitored pressures before and after the reaction cell; if the gradient became more than 20 bars (normal flow caused ~45 bars pressure at

both sides) the experiment was considered to be clogged. Flow was inhibited either by the desired precipitation in fractures and pores or by narrowing of the tubing. The runs lasted 66 days (a), 20 days (b), 32 days (c) and 10 days (d) and in both run c and d, the tubing was found to be full of a white precipitate that could be identified as gypsum. The resulting water-rock ratio ranged between 5-50, or an effective w/r between 35-350 when only a rim of 1 mm around the fracture was considered as the amount of rock in contact with fluid.

### 4.3.2 Measurements

Before, during and after the experiment, a 3D X-ray scan of the core was made using $\mu$-tomography with a ProCon CT-Alpha device. This technique acquires X-ray images of the sample during its 360° rotation (in this case in 1600 steps), detecting density contrasts within the core. The images were made at 125 kV and 350 $\mu$A using an X-ray WorX source and a Hamamatsu detector; under these conditions and a sample diameter of 1.8 cm (which determines the minimum distance the sample has to be placed away from the X-ray source in order to project the full sample on the detector), the pixel size was 13.6 x 13.6 $\mu$m$^2$. At the start and end of each experimental run an additional, more detailed scan of the inlet or outlet area (depending on the most promising geometry for potential precipitation) was made with a resolution of 9.6 x 9.6 $\mu$m$^2$. A 3D reconstruction of the obtained image stack was made using the Frauenhofer Volex software.

The scanned 3D-volumes were further analysed using the Avizo Fire software, version 9.0 and later. First, the scans were filtered using the Sigma Filter function (resolution of 13-14 $\mu$m). Consequently different grey values were segmented and given a mineral label, distinguishing unaltered rock, possible newly grown minerals and pore space.

The hydrothermal flow through cell was scanned every 1-2 weeks, for which the flow had to be stopped and the reaction cell was decoupled from the fluid circuit. The fluid inside the basalt was kept in place but the scan was started after the cell had cooled to 30°C as thermal shrinking during a scan would make 3D reconstruction, which uses overlap in the first and last image of a 360° rotation, impossible. Each consecutive scan was registered through labeling of recognizable small features both in the first scan of the sample and in the new scan, after which the new scan was transformed to have the same orientation as the old one. Then the labeled areas were compared in 4D, analyzing changes in volume and shape in newly grown minerals and pores over time.

89

Fluid samples taken from the outlet tubing were used to monitor mineral dissolution. The fluids were then diluted with a 1% $HNO_3$-solution and analysed using a Varian Vista Inductively Coupled Plasma-Optical Emission Spectroscopy (ICP-OES) device; data quality was checked using three standards. LOD for Fe was 0.001 mg/L. For pH-measurements, a pH-meter for small vessels was used and calibrated with three solutions of pH 4.01, 10.00 and 7.00.

These fluid compositions were used to infer the in situ speciation and mineral solubility using the EQ3/6 modelling software (Wolery and Jarek 2003). We used the cmp database (composite non-Pitzer) from the EQ3/6 software package, which includes many low-temperature phases. Some phases critical for this study were added to it, using log K values calculated with the SUPCRT92 software (Johnson et al. 1992) and the D11AB database; calculated values are presented in table 4.1. Additionally we modelled the reaction paths of each run from the start.

To analyse dissolving minerals in basalt over time we used the Geochemist′s Workbench (GWB) software (Bethke 1996) with a 250 bars thermodynamic database for ridge flank systems described by Türke et al. (2015). Dissolution rate is given by $r_k = A_S$ $k_+$ (1-Q/K), where $A_s$ is the reactive surface area, $k_+$ is the rate constant (calculated with the Arrhenius equation, using $E_A$ is the activation energy; see table 4.2 for input parameters) and Q and K represent the activity product and equilibrium constant of the reaction. To increase Fe-content we assumed that magnetite had a five times higher reactive surface area than the other minerals (2500 $cm^2$ $g^{-1}$), which could be justified by its small grain size.

Table 4.1: log K values for dissociation reactions of potential sulphate minerals in the system

| T(°C) | reaction | | |
|---|---|---|---|
| | Anhydrite[1] | Gypsum[2] | Bassanite[3] |
| 0 | -4.10 | -4.53 | -3.45 |
| 25 | -4.31 | -4.48 | -3.66 |
| 60 | -4.76 | -4.61 | -4.12 |
| 100 | -5.39 | -4.90 | -4.73 |
| 150 | -6.27 | -5.43 | -5.60 |
| 200 | -7.28 | -6.13 | -6.59 |
| 250 | -8.46 | -7.04 | -7.75 |
| 300 | -9.96 | -8.30 | -9.23 |

---

[1]Anhydrite ($CaSO_4$) = $Ca^{2+}$+ $SO_4^{2-}$
[2]Gypsum ($CaSO_4 \bullet 2H_2O$) = $Ca^{2+}$+ $SO_4^{2-}$+ $2H_2O$
[3]Bassanite ($CaSO_4 \bullet 0.5H_2O$) = $Ca^{2+}$+ $SO_4^{2-}$+ $0.5H_2O$

The bulk rock composition of the basaltic starting material (table 4.3) was determined using Wavelength Dispersive X-Ray Fluorescence (WDXRF) on glass beads. The measurements were performed with a Panalytical Axios machine (Almelo, the Netherlands) in Oldenburg at ICBM. The glass beads were prepared as described by Eckert et al. (2013). Relative precision on the standard for the measured elements ranged from 0.1-3.6.

Table 4.2: Mineral kinetic input parameters used in GWB modelling

| Mineral (95°run) | Mass (g) | $k_+$ (mol m$^2$ s$^{-1}$) | $E_A$ (J/mol) | $A_s$ (cm$^2$ g$^{-1}$) |
|---|---|---|---|---|
| Albite | 100 | 3.55E-10 | 54390 | 250 |
| Anorthite | 400 | 1.00E-04 | 62760 | 250 |
| Diopside | 500 | 1.02E-08 | 40580 | 500 |
| Magnetite | 50 | 3.02E-12 | 18620 | 500 |
| Mineral (120°run) | Mass (g) | $k_+$ (mol m$^2$ s$^{-1}$) | $E_A$ (J/mol) | $A_s$ (cm$^2$ g$^{-1}$) |
| Albite | 100 | 3.55E-10 | 54390 | 250 |
| Anorthite | 400 | 1.00E-04 | 62760 | 250 |
| Diopside | 500 | 1.02E-08 | 40580 | 500 |
| Magnetite | 50 | 3.02E-12 | 18620 | 2500 |

Formed precipitates were studied after opening of the reaction cell with a scanning electron microscope (Supra 40 SEM with XFlash 6/30 EDX-detector) on the fractured fragments using an acceleration voltage of 15 kV.

Table 4.3: Bulk rock composition of starting material

| oxide (wt.%) | basalt |
|---|---|
| $SiO_2$ | 49.03 |
| $TiO_2$ | 1.47 |
| $Al_2O_3$ | 15.39 |
| $FeO, total$ | 10.19 |
| MnO | 0.17 |
| MgO | 7.94 |
| CaO | 10.91 |
| $Na_2O$ | 2.86 |
| $K_2O$ | 0.23 |
| $P_2O_5$ | 0.14 |
| $SO_3$ | 0.2 |
| Total | 98.7 |

## 4.4    Results and Discussion

The cutting edge technology of flow-through cells combined with $\mu$-tomography asks for a different manuscript structure, where analyses on fluid and solid products are directly compared with models and possible effects from the experimental setup. Results and discussion are therefore put together and are ordered according to theme.

### 4.4.1    Fluid chemistry and solid products

Fluid samples show cation exchange between water and rock, which confirms that some reaction took place at all tested temperatures. Ca and $SO_4$ were initially taken up by the solid phase but quickly went back to their old values. Na, Si, K and Mg were released; their concentration went down again over time (fig. 4.2, appendix table S1) through precipitation. Fe is never detected in the output fluid. The system showed to be quite sensitive to temperature, as after each scan and consequent cooling-heating event, the chemistry differed slightly (see blue bars in fig. 4.2). Measured pH of the output fluids decreased over time from 7.0 to 6.2.

   Precipitation of new phases was only detected on part of the fracture surface. An overview of the runs and their input parameters and output minerals is given in table 4.4. The main alteration included silicates and there were many Fe-bearing phases (fig. 4.3). Although anhydrite was formed at 120°C and 140°C it occurs in much lower quantities than expected and shows dissolution textures. This asks for a justification of our experimental setup, given in the following section.

Table 4.4: Overview of parameters in different experimental runs

| T (°C) | length (cm) | run (days) | porosity (%) | eff. w/r |
|--------|-------------|------------|--------------|----------|
| 95 | 2.5 | 66 | 6.5 | 365 |
| 110 | 2.7 | 20 | 7 | 100 |
| 120 | 3.0 | 32 | 6.1 | 146 |
| 140 | 2.6 | 10 | 5.5 | 34 |

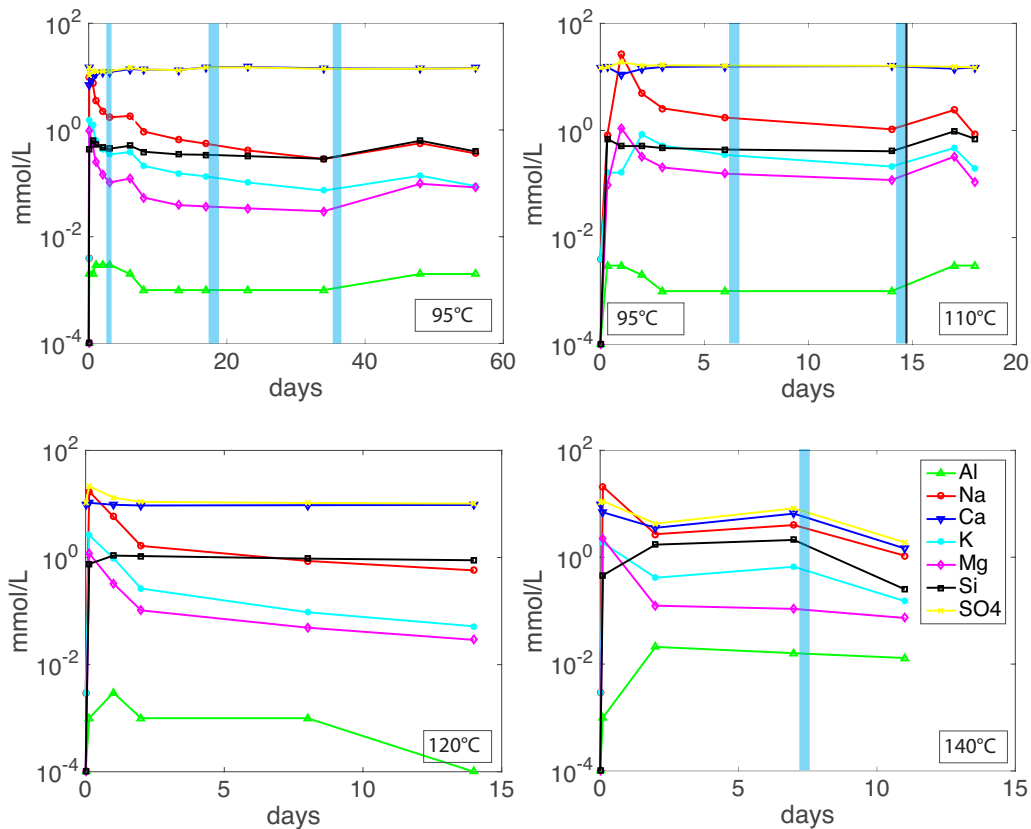| T (°C) | SI anh | SI gy | secondary minerals | other features |
|--------|--------|-------|--------------------|----------------|
| 95 | 4.21 | 1.5 | hem, sap | 100 $\mu$ displaced |
| 110 | 5.56 | 1.5 | hem, sap | little alteration |
| 120 | 4.59 | 1.1 | anh, hem, mag, sap, mes | tubing clogged |
| 140 | 5.59 | 0.94 | anh, hem, mag, sap, mes, py | tubing clogged |

Figure 4.2: Major element fluid chemistry for all the runs, given in mmol/L. Vertical blue bars indicate temporary stop in fluid flow to accommodate a scan.

### 4.4.2 The experiments

**Flow-through setup** The flow-through cell has some limitations that might have affected reaction progress. The pump and tubing system were not completely airtight, meaning that some $CO_2$ may have entered the solution and equilibration of the inlet fluid with air may have occurred. As we did not observe any carbonate phases, we rule out any large effects on mineralogy. It may however have affected the pH of the fluids, as the observed values of 6.2-7 are lower than can be expected during cation release in fluid-rock interaction.

Cooling of the fluid in the tubing poses a real problem that cannot be avoided, as the system has to be cooled before opening the reaction cell or before scanning. Fluid chemistry changes notably from before to after the scan, showing that cooling may have caused some
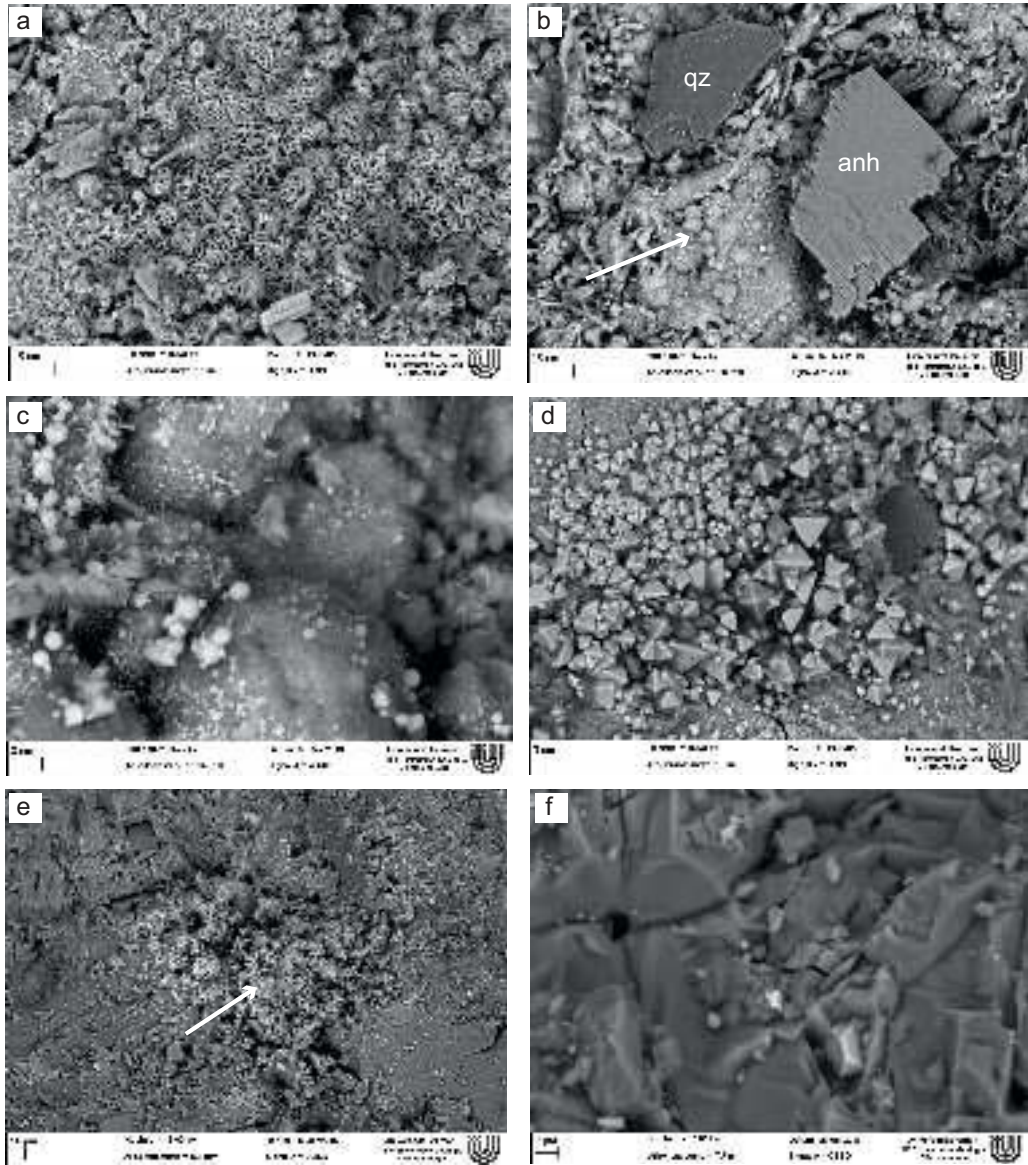
93

Figure 4.3: SEM images of the basalt; a) hematite rosettes in pore space; b) anhydrite and quartz crystal on globular Fe (white arrow); c) globular Fe with pure Fe spots; d) octahedral magnetite; e) skeletal Fe-phase (white arrow); f) unaltered basalt.

re-equilibration. However, stabilization to former levels is observed at the next fluid measurement (fig. 4.2) implying that possible low-temperature phases have re-dissolved.

The final, major problem is clogging of the inlet tubing. Although we have tried to keep anhydrite and gypsum below their precipitation point before interaction with rock, the detection of gypsum in the tubes at both 120 and 140°C and its suspected presence in the tubing of the 110°C run shows that precipitation did occur. It must be mentioned that, although we measured gypsum, the phase most likely precipitated as anhydrite, since this is the stable sulphate phase at elevated temperatures. Later cooling in the presence of the pure calcium sulphate solution may have caused the transformation into gypsum. In the basalt core, other ions came into solution and this possible retrograde phase transition is not observed.

**Chosen fluid composition** The starting reactive fluid contained 0.015 (runs a and b) and 0.010 moles (runs c and d) of dissolved gypsum/L. This may seem very little and cannot result in a lot of anhydrite formation; in a run of 66 days, 0.015 mmol at a flow rate of 0.010 mL/min results in 14.3 mmoles of sulphate added to the system. Of this, 8-11 mmoles are expected to drop out to reach equilibrium at temperatures between 95 and 140°C, forming roughly 10-13 mg of anhydrite. However, mineral saturation would be reached for gypsum during heating if slightly higher concentrations of calcium and sulphate in the starting fluid were used (0.020 mol/L), which is undesirable. Below the transition temperature of gypsum and anhydrite at 54.5°C (Otálora and García-Ruiz 2014), the saturation index of gypsum should stay <1 if this mineral is to stay in solution. Since anhydrite precipitation is sluggish (Pina 2009; Morales et al. 2012) we assumed a supersaturation of 5 before its formation. This value turned out to be quite accurate as in the 110°C and 140°C runs anhydrite overstepped this and the tubing before the reaction cell was rapidly clogged. Input fluids should therefore stay just below this point for anhydrite. This set of conditions severely limited the possible fluid input compositions and resulted in the used solutions as most feasible scenarios. To make anhydrite precipitation as likely as possible, no other ions were added to the solution.

**Temperature and pressure** Our main objective was to form anhydrite under ridge-flank conditions, so we tested temperatures between 100-150°C. Anhydrite was slightly supersaturated (SI of 4.2) in the inlet fluid at 95°C and even more at 110°C (5.6; see table 4.4). Gypsum was also

supersaturated in both fluids (SI of 1.5), but this phase was not formed at these temperatures far above the transition temperature with anhydrite. Since no anhydrite precipitation was observed in these experiments, new runs at slightly higher temperatures and accordingly modified fluid compositions (see previous section on fluid chemistry) were performed, resulting in successful anhydrite precipitation at $120°C$ and $140°C$. Increasing temperatures further was not possible as the PEEK material used for the reaction cell and tubing experiences a phase transition at $152°C$. Pressure has very little effect on anhydrite formation; log K values for the anhydrite dissociation reaction between 2 and 250 bars at $120°C$ ranged from -5.73 to -5.55.

These experiments show that temperatures around $100°C$ are definitely too low to form anhydrite in a matter of months. This implies that growth kinetics are inhibited because the fluids are highly supersaturated and cannot explain its absence. It does not mean that alteration is absent below $100°C$; many signs of re-equilibration of silicate minerals are observed. These will be discussed in more detail in a later section.

**Flow rate**   The choice of flow rate was an arbitrary one, based on the literature. Luhmann et al. (2017) performed basalt flow-through experiments at $150°C$ and a variety of flow rates to study its effect on fluid-rock interaction. Although relatively high flow rates (0.1 mL/min) result in higher w/r ratios and thus more reactive fluid in the system, the residence time of that fluid becomes shorter, as does the time to equilibrate the system. In the experiments by Luhmann et al. (2017) these high flow rates resulted in a rapid increase in system permeability and only dissolution occurred as transport rates exceeded reaction rates by a few orders of magnitude, a factor represented by the Damköhler number (Da). Low Da represents a system where reaction rate is much lower than the mass transport rate, resulting in the flushing of the system. At a high Da, the reaction rate is more rapid and fluid is not taken away before it can re-precipitate minerals. Very low flow rates therefore result in a more equilibrated and rock-dominated system. This can lead to rapidly decreasing permeability and zoning with more dissolution upstream and precipitation downstream (Luhmann et al. 2017). Slow anhydrite kinetics benefit most from long equilibration times so we chose a low flow rate of 0.01 mL/min.

### 4.4.3 Experiments vs. models

As seen above, the experimental setup cannot explain the lack of anhydrite precipitation. The saturation overstepping needed before anhydrite forms is well known (Pina 2009; Morales et al. 2012). However, the small quantities of anhydrite in our runs show that growth did occur, but was less extensive than anticipated, even taking slow kinetics into account. We will therefore shift our focus to the other observed alteration features, searching for an explanation for the low amounts of anhydrite.

Clay phases are manifested as a fine-grained cover on the fracture in all runs. We could not identify them with confidence but saponite and traces of nontronite are the most likely. Voids contained clays and Fe-rich platelets that were identified as hematite based on their crystal shape (fig. 4.3a). All runs also show the formation of a globular, Fe-rich crust with <1 wt.% S covering the basalt minerals on the fractured surface (see arrow in fig. 4.3b). These botryoidal shapes were tentatively identified as hematite based on their similarities with EDX measurements from the platelets. The globules could contain traces of Mn and were occasionally dotted with small Fe spots too small to identify (fig. 4.3c). The 120°C run also displayed a line of octahedral magnetite crystals (fig. 4.3d), pyrite framboids and platy anhydrite crystals along with minor quartz (fig. 4.3b) as well as skeletal growth of a Fe-rich phase (arrow in fig. 4.3e). The 140°C run also showed some anhydrite, but this mineral showed clear dissolution structures and was sometimes covered with Fe-globules or pyrite framboids. Despite the high w/r used in our experiments, the formation of secondary minerals on the fracture surface was patchy.

Reaction path models showed that expected secondary phases were clays, zeolites, hematite, and, for the higher temperature runs (120 and 140°C), additional magnetite, anhydrite, pyrite and hydrogarnet (table 4.5). The minerals in the table are ordered according to their occurrence with reaction progress Xi, hematite forming early in the reaction and magnetite much later. These minerals do not coexist spatially but are anticipated at different times or different depths in the core. High water-rock conditions next to the fracture are best represented by the first phases forming in the model; later steps have become more rock-dominated and reducing. The first phases to form in the model are clays such as saponite and nontronite as well as hematite and, in the higher temperature runs, anhydrite. This is consistent with our experiments (see table 4.5). A later step involves formation of pyrite, which is observed in the 120°C run and sporadically in the 140°C experiment. Its presence implies that more reducing conditions prevail away from the inlet.

97

However, mass balance calculations using cumulative fluid output and bulk rock data (table 4.1) show that the maximum possible alteration is 1%, in which case the reaction does not move as far as this pyrite field for most runs.

The 110°C run was stopped after 20 days due to clogging of the inlet tubes and shows the least signs of alteration. It did however show a surface roughness not observed in the starting material displayed in fig. 4.3f, confirming that reaction did take place. The 95°C run points out that alteration occurs even below 100°C if the experiment runs long enough, mainly resulting in fuzzy clays and zeolite rods plus occasionally globular Fe-crust. All runs thus show that the main alteration does not involve the calcium and sulphate ions but uses released Si, Fe and Mg. Especially the variety of Fe occurrences caught our interest and will be discussed in more detail. But first, we will compare the modelled and observed results to natural systems.

### 4.4.4   Observed mineralogy: experiments vs. nature

As shown by Luhmann et al. (2017), there will be in-depth changes in a flow-through core since the infiltrating fluid changes composition upon interaction with rock. In nature this is seen especially as changes in the oxidation state with depth when the previously reacted fluid percolates deeper in the crust and w/r decreases (Alt 1995; Pichler et al. 1999). This early stage of infiltration leads to increased alkali and Fe content in the fluid phase, resulting in Fe-oxyhydroxides, celadonite (Andrews 1980) and K-Ca clays (Alt and Honnorez 1984). At depth, more reducing conditions produce Mg-Fe rich clays (saponite) and zeolites (analcime), a transition that is occasionally even observed within a single alteration halo as the progressive uptake of oxygen form the infiltrating fluid (Andrews 1980). Eventually this process can lead to pyrite formation in the non-oxidative diagenesis zone (Andrews 1977). Some natural examples of this mineral sequence include the Reykjanes hydrothermal system (Tómasson and Kristmannsdóttir 1972), DSDP site 417 (Alt and Honnorez 1984) and Southwest Indian ridge (Nakamura et al. 2007).

Oxidation state of the system might thus be crucial to the alteration mineralogy in our experiments. Redox changes are visible in the iron occurrence at depth in our flow-through core (fig. 4.4), showing hematite and clays at the inlet, magnetite slightly closer to the outlet area and pyrite even deeper in the core. To analyse the oxidation state within the sample at different depths, we used the GWB modelling software. Calculated Gibbs energy for the observed

| | 95°C | 110°C | 120°C | 140°C |
|---|---|---|---|---|
| hematite | x | x | x | x |
| diaspore | | | | |
| chlorite | | | | |
| saponite | x | x | x | x |
| nontronite | ? | ? | ? | ? |
| pyrite | | | x | x |
| mesolite | x | x | ? | |
| andradite | | | | |
| anhydrite | | | x | x |
| celadonite | | | | |
| microcline | | | | |
| annite | | | | |
| minnesotaite | | | | |
| magnetite | | | x | x |
| quartz | | | x | (x) |

| predicted during reaction | |
|---|---|
| observed | x |

Table 4.5: Overview of modelled and observed mineralogy

Fe-bearing phases (hematite, magnetite, nontronite and pyrite) showed that the affinity for hematite formation is the highest under all fluid compositions (high and low Fe, high and low pH) except at low dissolved $O_2$ ($10^{-50}$) where magnetite takes over. At temperatures around 140°C pyrite can also form after sulphate reduction. This is a potential explanation for the low observed sulphate, as part of it may have become reduced. We do observe anhydrite dissolution features, but pyrite is not spatially associated with anhydrite and we rule this out as a reason for the low anhydrite abundance.

Related to anhydrite we do see some quartz; deposition of quartz and anhydrite is also recorded in nature for similar conditions (Tómasson and Kristmannsdóttir 1972). It occurs only in the middle of the core, where pore spaces are available for the quartz to grow in. This shows
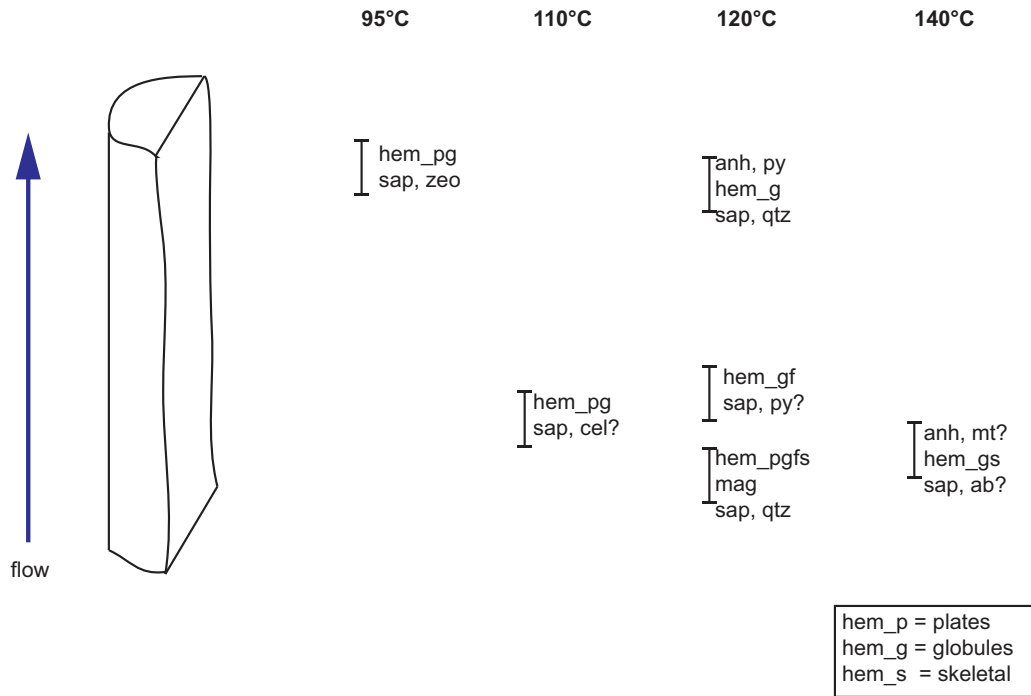
Figure 4.4: Secondary mineralogy observed in the altered cores with depth. Observed mineralogy is ordered based on temperature of the experiment.

that besides depth or oxidation state, surface irregularities also play a role in the formation of secondary phases. Hematite platelets focus in pore space while globules grow on asperities. These local heterogeneities create microenvironments that cannot be explained by a whole rock alteration trend but we will elaborate on this later. It is however clear that Fe plays a large role in this low temperature basalt alteration.

### 4.4.5   Iron mobility

The different Fe-bearing mineral phases (magnetite, hematite, Fe-Mn-rich crust) within the basalt core show that Fe has been present in the fluid phase. Fe-mobility and redistribution in hydrothermally altered rocks has been mentioned in many environments, including some at lower temperatures (MORB: Bach and Edwards, 2003; pillow basalts: Polat et al. 2012; PGE-deposit in ultramafics: Holwell et al. 2017; continental volcanic basin: Zhang et al. 2015). After initial release from primary minerals as $Fe^{2+}$ (olivine, pyroxenes, chlorite), iron is rapidly captured in

clays (Andrews 1980) or zeolites and Fe-oxyhydroxides upon oxidation (Markússon and Stefánsson 2011). Staudigel et al. (1996) calculated small Fe-fluxes for low temperature hydrothermal basalt alteration, implying that this element's mobility was spatially limited and no significant Fe is present in output fluids. This suggests that iron stability in fluids is short lived.

Fe-transport in fluids depends on the possibility to form complexes with ligands. Most experimental and thermodynamic studies on Fe stability look at high temperature saline fluids, where the $Cl^-$-complex plays a large role (Ding and Seyfried 1992; Seyfried and Ding 1995; Douville et al. 2002; Seward et al. 2014). Seyfried and Bischoff (1981) state that iron is practically immobile at temperatures $<300°C$, where most Cl-complexes become unstable (Berndt et al. 1989; Seewald and Seyfried, 1990). Some low temperature ($<200°C$) complexes with Cl are possible but the largest amount of dissolved iron occurs as $Fe^{2+}$, even if the fluid is slightly saline (Heinrich and Seward 1990); Fe-OH complexes are more important in this environment.

In our Cl-free solution, a Pourbaix diagram (or potential pH diagram) nicely displays the Fe-species stability. We replotted the diagram of Beverskog and Puigdomenech (1996) at Fe=$10^{-8}$ M for $120°C$ (fig. 4.5a), showing that in our pH range the most likely forms of iron are as hematite, magnetite or non-complexed $Fe^{2+}$. As the field of the latter is quite small at neutral pH, transport is unlikely to go far and the solids are expected to form quickly from solution. Our measured pH values below 7.0 make it impossible to form magnetite, but the in situ values were most likely higher as $CO_2$-uptake form the air could lower fluid pH during the 2-hour sample collection process. In our fluid, Fe can thus either precipitate as magnetite or become oxidized to $Fe^{3+}$, which is unstable and forms hematite. Upon contact with the sulphate-bearing fluid, the iron oxidation can also lead to sulphate reduction, forming pyrite. This is indicated in fig. 4.5b, where a sulphate activity of 0.020 mol/L is assumed. This process is known as thermochemical sulphate reduction (TSR) and proceeds through abiotic reduction of sulphate. This reduction of sulphate through Fe is recorded in experiments at 250-350°C (Shanks et al. 1981) but our results imply that this process might also take place at temperatures as low as $120°C$.

We tried to explain the link between different Fe-bearing minerals and depth with a GWB model that takes mineral dissolution kinetics into account. Input minerals included anorthite, albite, diopside and magnetite (for input parameters, see table 4.2). The fluid was observed to follow the same trend as we measured, and secondary minerals included initial hematite, anhydrite shortly after formation, saponite a bit later, and late stage pyrite. Because our
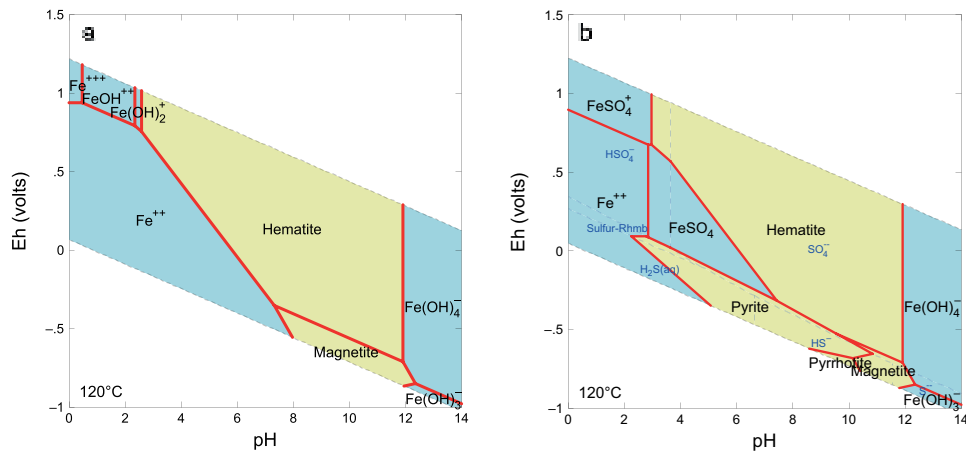
Figure 4.5: pH vs. Eh diagram showing stability of aqueous species; a) At an Fe-activity of 10-8, $Fe^{2+}$ is the main free species around neutral pH. It can be captured as hematite or magnetite due to small shifts in pH and Eh; b) In the presence of 0.02 mol/L sulphate, the diagram looks different and pyrite, pyrrhotite and the $FeSO_4$(aq) species play a role.

percolating fluid continuously reacts with rock the deeper it gets, we can convert this time-based model to a depth-based model where deeper percolated fluid has had a longer reaction time. The depth based model would expect hematite and anhydrite close to the inlet and stay present over the core length, as does saponite, while pyrite comes in later. This resembles our observations although the important interplay between hematite and magnetite is left out if magnetite is used as input mineral. The anhydrite problem however is not solved as this model also predicts its direct formation upon saturation.

**Crystal shapes of iron-bearing phases** Hematite in the reacted cores shows up with different crystal morphologies: globules, framboids or platy crystals. Mineral growth consists of two steps: nucleation of crystals and continued growth of these crystals (Stumm 1992). Nucleation depends on the overstepping of a certain activation energy, which makes it energetically favourable over growth. If this barrier is not reached, growth on already existing crystals is more likely depending on the amount and type of crystal sites to grow on (Steefel and Van Capellen 1990; Putnis et al. 1995; Otálora and García-Ruiz 2014). In one environment or from one solution, multiple hematite morphologies have been previously reported (Demianets et al. 2003).

The globules and Fe-rich crust shows that growth was non-crystalline, probably representing

102

precipitation from a thin fluid film on the surface. This may occur especially at asperities, where the flow rate is severely reduced. The amorphous phase also contains up to 1 wt.% S and up to 18 wt.% Mn, especially at low temperatures. Similar structures rich in Mn have been mentioned for a hydrothermal deposit at $12°50'$N (Dekov et al. 2011).

The presence of framboids or colloids can indicate high nucleation rates and slow growth. This often occurs at very high supersaturation (Butler and Rickard 2000; Ohfuji and Rickard 2005). Each formed crystal seed does not expand much because it is more favourable to form a new framboid. Eh was found to affect pyrite nucleation rates (Butler and Rickard 2000): a small Eh increase led to a large increase in framboid formation. Changes in oxidation state of our percolating fluid may thus have affected both the stable iron phase and the crystal shape, the most favourable oxidation state resulting in more rapid crystallization and thus framboidal growth.

Another common occurrence under rapid nucleation and slow growth circumstances is skeletal growth (observed in the high temperature runs, fig. 4.3e). Growth is localized only on the tip of the branch that grows further outward (Jamtveit and Hammer 2012). Like botryoids, they only form in low flow conditions.

Large crystals of magnetite and the plate-like hematite rosettes imply the exact opposite. Fewer crystals are observed per surface area, but these are larger and better developed. Nucleation was more difficult in these settings and continued growth on an existing surface was preferred, expanding the size of the limited amount of crystals. The crystal size is also expected to increase when fluid flow decreases, explaining the larger crystals close to the outlet.

Besides nucleation kinetics and geochemistry, the role of microorganisms should never be ruled out at lower temperatures (Zeng et al. 2012; Bach and Edwards 2003). However, as thermodynamic sulphide reduction is observed here at temperatures as low as 140°C, less reduced iron may be available and microbial processes might be less important than previously thought.

### 4.4.6   Changes in core geometry

Each experiment was monitored using X-ray tomography. One scan was made at the beginning and one at the end of each run. The resulting reconstructed 3D volumes were mainly compared at the places where precipitation was observed in SEM, which was always on the main fracture surface. The scans sometimes showed a narrowing of the main fracture (fig. 4.6) but no new grey value was observed (which would indicate a new phase). From the size of the detected crystals in

SEM (up to 20 $\mu$m) we deduced that the resolution of the $\mu$-tomography scans for samples this size (voxel size of 13.6 x 13.6 x 13.6 $\mu$m$^3$) was too low, hence this method is not capable of showing in situ alteration.



Figure 4.6: X-ray tomography scan of the 95°C run, showing no narrowing of pores between start (left) and right (end) of the experiment. The top images represent a top view; bottom images are cut at the red line and viewed from the right (see arrow). Here the reacted basalt shows the formation of a new fracture.

A striking feature in the scans however was the formation of new fractures in the 95 and 120°C run perpendicular to the flow direction. Registration of single fractured blocks allowed us to show the displacement between them and a vector displaying the direction and distance of the shift in the 95°C run are given in fig. 4.7. Yellow colours indicate a high shift (up to 100 $\mu$m) between the 2 scans, purple means a low shift. The new fractures in both runs developed at different depths in the core for both runs, but their orientation perpendicular to the flow direction is the same. This implies that they result from a force working in this orthogonal direction. There are several options for this: (1) bending of the rock sample in the reaction cell; (2) fluid pressure gradients over the length of the core; (3) crystallization pressure; and (4) further shrinking of the surrounding shrink sleeve, which would result in the observed thinning in the y- and stretching in x- and z-direction (95°C run) or compression in all directions (120°C run). We observed that the new fracture has pushed the upper rock fragment 100 $\mu$m towards the outlet. As the fracture occurred at different depths in both samples (exactly halfway in 95°C run, close to inlet in the

120°C run) stress localization in previous heterogeneities is expected to determine the exact location of fracture initiation. This is confirmed by a detailed view of the fracture in the 95°C run (fig. 4.8) where the fracture seemed to start at two sides; one side within a cluster of pores and on the other side at the point where the main fracture split in two fracture paths. Both would cause a stress anomaly at the point of the fracture, leading to its initiation. The two fractures met in the middle, forming one new fracture that divided the sample halve in two.
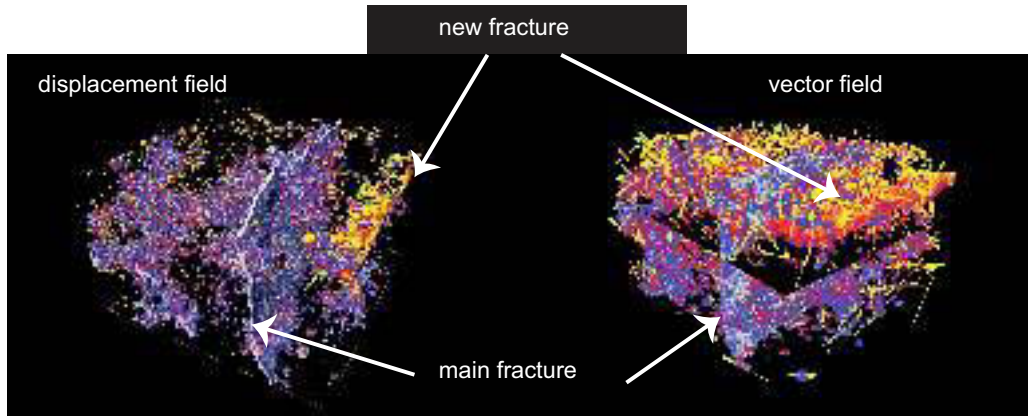


Figure 4.7: Displacement field (left) and vector field (right) of the new fracture in the 95°C experiment. Displacement is roughly 100 $\mu$m upwards (towards outlet).
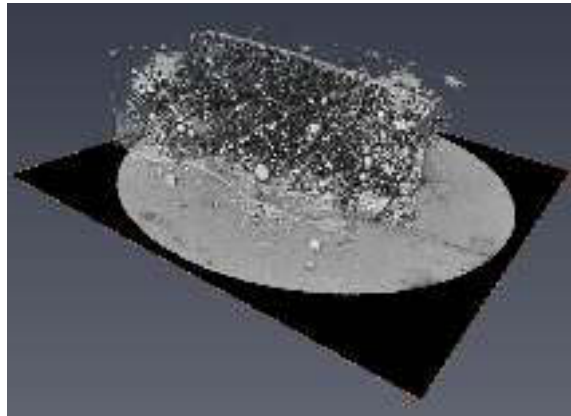


Figure 4.8: Avizo segmented image of pore space and fracture. The new fracture goes sideways; on the side facing to the front it nucleates in a split in the main fracture, on the side facing away it goes through a cluster of larger pores.

To test these different scenarios, a Discrete-Element-Model (DEM) (Jamtveit et al. 2000, 2009) with a simple 2D plane of nodes was set up with extendable rods (depending on internal stress) connecting them in a hexagonal grid (fig. 4.9). Input parameters involved fluid flow rate, reaction rate (and expansion rate $\Delta V$ upon reaction), diffusion rates (both of matter and heat), pressure gradient, rock permeability and fracture geometry by leaving out some connecting rods. Fluid was always modelled to come in from the top. Scenario (1) was not tested in this simple model as the boundary conditions concerning confining pressure were set; bending was not expected to occur in such short samples and there was no evidence of it in the measured displacement of the different fragments, which were offset purely in the direction perpendicular to the fault (see fig. 4.7). The input parameters of rock properties were set the same in every run (standard basalt permeability of 10-15). Scenario (2) was tested thoroughly, setting a confining pressure of 40 bars on all sides except the outlet which had 36 bars, but a fluid pressure gradient of 4 bars (which was the maximum gradient observed during the experiment) was not seen to cause any fractures. Although displacement could be seen, this was acting perpendicular to the existing fracture, pushing the rock fragments sideways. Even with very favourable fracture geometry to cause fracturing (fig. 4.9a) stress localization in the model was minimal. We therefore rule out this mechanism as a cause for new fracture formation.
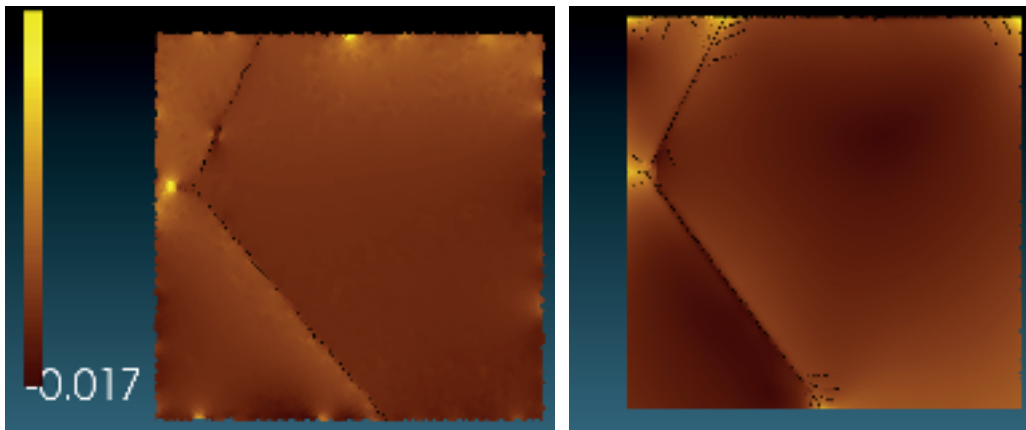


Figure 4.9: DEM output images; a) shows stress localization at the fracture tip when a fluid pressure gradient of 4 bars is present over the core length; b) fracture geometry after reaction with 2% volume increase.

Scenario (3) of crystallization pressure could be tested by increasing the reaction rate and

resulting volume change (taken as 0.02 according to a 2% alteration; this is a 10 times exaggeration but the real values showed nothing in the model time). Although at this point some new fractures were observed (fig. 4.9b), their geometry did not match the one observed in our experiments and this mechanism can also not account for the perpendicular fractures. We did however see the stress localization in the tip of fractures, confirming that stress localization might have been the cause of breaking.

Scenario (4) could not be modelled, as the pressure at the plane boundaries was fixed. Instead, we tested this hypothesis by measuring the diameter of all reconstructed volumes before and after the run. The 110°C run and 120°C run indeed showed a thinning of 0.10 and 0.05 mm respectively, the 95°C run however showed a thickening of 0.15 mm. Still, the narrowed pores visible in the 120°C run prove that the core was pushed together, leading to the suspicion that the shrinking sleeve was to blame. As this material contracts during heating, it is used to fit around the basalt core and it was heated by blowing hot air (130°C) at it until no water can pass between the sleeve and the core. However, during the experiment further heating could have led to increased shrinking. This is therefore considered as the most likely reason for the observed shift and contraction within the cores over time, and not factors such as bending or crystallization.

## 4.5   Implications

The difficulties to form anhydrite through percolation of a pre-fractured basalt core at temperatures up to 140°C show that in nature, this process will probably be slow. Thermodynamic models cannot properly predict anhydrite formation as only small amounts of this mineral are formed, even at high supersaturation (SI>5).

The results of this study furthermore highlight the potentially large role of Fe in ridge flank systems. Redistribution of iron in several mineral phases indicates changing w/r with depth in the core. Different crystal habits of hematite show that fluid composition is likely heterogeneous and saturation indices may change on short distances, most likely related to different flow rates through surface roughness. Iron appears to be very reactive, and thermochemical sulphate reduction (TSR) occurs within a few days in the 120°C and 140°C run.

Especially this last point may have large implications, as it affects the habitability of the ridge flanks. Much less free reduced iron may be present as a potential energy source for microbial life than previously thought (see Bach and Edwards 2003). This might imply that off axis systems

do not become inhabited at a high rate. However, a detailed study of natural samples is needed to confirm if similar short-distance Fe-mobilization takes place in ridge flank systems.

## 4.6    Acknowledgements

## 4.7    References

Alt J.C., 1995. Subseafloor processes in mid-ocean ridge hydrothermal systems. In: Humphris S.E., Zierenberg R., Mullineaux L., Thomson R. (Eds.), Seafloor Hydrothermal Systems: Physical, Chemical, Biological and Geological Interactions. Geophysical Monograph, Vol. 91. American. Geophysical Union, pp. 85-114

Alt J.C., Davidson G.J., Teagle D.A.H., Karson J.A., 2003. Isotopic composition of gypsum in the Macquarie Island ophiolite: Implications for the sulfur cycle and the subsurface biosphere in oceanic crust. Geology 31: 549-552

Alt J.C., Honnorez J., 1984. Alteration of the upper oceanic crust, DSDP site 417: mineralogy and chemistry. Contributions to Mineralogy and Petrology 87: 149-169

Andrews A.J., 1977. On the effect of low-temperature seawater-basalt interaction on the distribution of sulfur in oceanic crust, layer 2. Earth and Planetary Science Letters 46: 68-80

Andrews A.J., 1980. Saponite and Celadonite in Layer 2 Basalts, DSDP Leg 37. Contributions to Mineralogy and Petrology 73: 323-340

Bach W., Edwards K.J., 2003. Iron and sulfide oxidation within the basaltic ocean crust: Implications for chemolithoautotrophic microbial biomass production. Geochimica et Cosmochimica Acta 20: 3871-3887

Bach W., Roberts S., Vanko D.A., Binns R.A., Yeats C.J., Craddock P.R., Humphris S.E., 2003. Controls of fluid chemistry and complexation on rare-earth element contents of anhydrite from

the Pacmanus subseafloor hydrothermal system, Manus Basin, Papua New Guinea. Mineralium Deposita 38: 916-935

Berndt M.E., Seyfried Jr. W.E., Janecky D.R., 1989. Plagioclase and epidote buffering of cation ratios in mid-ocean ridge hydrothermal fields: Experimental results in and near the supercritical region. Geochimica et Cosmochimica Acta 53: 2283-2300

Bethke C.M., 1996. Geochemical Reaction Modeling. Oxford University Press, New York

Beverskog B., Puigdomenech I., 1996. Revised Pourbaix diagrams for iron at 25-300°C. Corrosion Science 38(12): 2121-2135

Bischoff J.L., Seyfried Jr., W.E., 1978. Hydrothermal chemistry of seawater from 25 to 350°C. American Journal of Science 278: 838-860

Butler I.B., Rickard D., 2000. Framboidal pyrite formation via the oxidation of iron (II) monosulfide by hydrogen sulphide. Geochimica et Cosmochimica Acta 64-15: 2665-2672

Chiba H., Uchiyama N., Teagle D.A.H., 1998. Stable isotope study of anhydrite and sulfide minerals at the TAG hydrothermal mound, Mid-Atlantic Ridge, 26°N. In: Herzig, P.M., Humphris, S.E., Miller, D.J., and Zierenberg, R.A. (Eds.), Proceedings of the Ocean Drilling Program, Scientific Results, Vol. 158, pp. 85-90

Dekov V., Boycheva T., Hålenius U., Billström K., Kamenov G.D., Shanks W.C., Stummeyer J., 2011. Mineralogical and geochemical evidence for hydrothermal activity at the west wall of 12°50′N core complex (Mid-Atlantic ridge): A new ultramafic-hosted seafloor hydrothermal deposit? Marine Geology 288: 90-102

Demianets L.N., Pouchko S.V., Gaynutdinov R.V., 2003. $Fe_2O_3$ single crystals: hydrothermal growth, crystal chemistry and growth morphology. Journal of Crystal Growth 259: 165-178

Ding K., Seyfried Jr. W.E., 1992. Determinatino of Fe-Cl complexing in the low pressure supercritical region (NaCl fluid): Iron solubility constraints on pH of subseafloor hydrothermal fluids. Geochimica et Cosmochimica Acta 56: 3681-3692

Douville E., Charlou J.L., Oelkers E.H., Bienvenu P., Jove Colon C.F., Donval J.P., Fouquet Y., Prieur D. and Appriou P., 2002. The rainbow vent fluids (36°14′N, MAR): the influence of ultramafic rocks and phase separation on trace metal content in Mid-Atlantic Ridge hydrothermal fluids. Chemical Geology 184: 37-48

Eckert S., Brumsack H.-J., Severmann S., Schnetger B., März C., Fröllje H., 2013. Establishment of euxinic conditions in the Holocene Black Sea. Geology 41(4): 431-434

Gudbrandsson S., Wolff-Boenisch D., Gislason S.R., Oelkers E.H., 2011. An experimental study of crystalline basalt dissolution from 2≤ pH≤ 11 and temperatures from 5 to 75°C. Geochimica et Cosmochimica Acta 75: 5496-5509

Haymon R.M., 1983. Growth history of hydrothermal black smoker chimneys. Nature 301: 695-698

Heinrich C.A., Seward T.M., 1990. A spectrophotometric study of iron (II) chloride complexing from 25 to 200°C. Geochimica et Cosmochimica Acta 54: 2207-2221

Holwell D.A., Adeyemi Z., Ward L.A., Smith D.J., Graham S.D., McDonald I., Smith J.W., 2017. Low temperature alteration of magmatic Ni-Cu-PGE sulfides as a source for hydrothermal Ni and PGE ores: A quantitative approach using automated mineralogy. Ore Geology Reviews, http://dx.doi.org/10.1016/j.orefeorev.2017.025

Humphris S.E., Cann J.R., 2000. Constraints on the energy and chemical balances of the modern TAG and ancient Cyprus seafloor sulfide deposits. Journal of Geophysical Research 105 (B12): 28.477-28.488

Humphris S.E., 1998. 12. Rare Earth Element Composition of anhydrite: implications for deposition and mobility within the active TAG hydrothermal mound. In: Herzig P.M., Humphris S.E., Miller D.J., Zierenberg R.A. (Eds.), Proceedings of the Ocean Drilling Program, Scientific Results Vol. 158, pp. 143-159

Jamtveit B., Hammer Ø., 2012. Sculpting of Rocks by Reactive Fluids. Geochemical Perspectives 1(3): 341-480

Jamtveit B., Austrheim H., Malte-Sørensen A., 2000. Accelerated hydration of the Earth?s deep crust induced by stress perturbations. Nature 408: 75-78

Jamtveit B., Putnis C., Malte-Sørensen A., 2009. Reaction induced fracturing during replacement processes. Contributions to Mineralogy and Petrology 157: 127-133

Janecky D.R., Seyfried Jr. W.E., 1984. Formation of massive sulfide deposits on oceanic ridge crests: Incremental reaction models for mixing between hydrothermal solutions and seawater. Geochimica et Cosmochimica Acta 48: 2723-2738

Johnson J.W., Oelkers E.H., Helgeson H.C., 1992. Supcrt92: A software package for calculating the standard molal thermodynamic properties of minerals, gases, aqueous species, and reactions from 1 to 5000 bars and 0 to 1000°C. Computers & Geoscience 18(7): 899-947

Kahl W.-A., Hansen C., Bach W., 2016. A new X-ray-transparent flow-through reaction cell for a

$\mu$-CT-based concomitant surveillance of the reaction progress of hydrothermal mineral-fluid interactions. Solid Earth 7: 651-658

Kristmannsdóttir H., 1979. Alteration of basaltic rocks by hydrothermal activity at 100-300°C. In: Mortland M., Farmer V. (Eds.), Developments in Sedimentology, Vol. 27. Elsevier, Amsterdam, pp. 359-367

Kuhn T., Herzig P.M., Hannington M.D., Garbe-Schönberg D., Stoffers P., 2003. Origin of fluids and anhydrite precipitation in the sediment-hosted Grimsey hydrothermal field north of Iceland. Chemical Geology 202: 5-21

Lister C.R.B., 1982. ′Active′ and ′passive′ hydrothermal systems in the ocean crust. In: Fanning K.A., Manheim F.T. (Eds.), The dynamic environment of the Ocean floor. DC Heath, Lexington, MA, pp. 441-470

Luhmann A.J., Tutolo B.M., Bagley B.C., Mildner D.F.R., Seyfried Jr W.E., Saar M.O., 2017. Permeability, porosity, and mineral surface area changes in basalt cores induced by reactive transport of $CO_2$-rich brine. Water Resources Research 53:1908-1927, doi:10.1002/2016WR019216

Markússon S.H., Stefánsson A., 2011. Geothermal surface alteration of basalts, Krýsuvík Iceland –Alteration mineralogy, water chemistry and the effects of acid supply on the alteration process. Journal of Volcanology and Geothermal Research 206: 46-59

Morales J., Astilleros J.M., Fernández-Díaz L., 2012. A nanoscopic approach to the kinetics of anhydrite (100) surface growth in the range of temperatures between 60 and 120°C. American Mineralogist 97: 995-998

Mottl M.J., 1983. Metabasalts, axial hot springs, and the structure of hydrothermal systems at mid-ocean ridges. Geological Society of America Bulletin 94: 161-180

Mottl M.J., Holland H.D., Corr R.S., 1979. Chemical exchange during hydrothermal alteration of basalt by seawater: II. Experimental results for Fe, Mn and sulfur species. Geochimica et Cosmochimica Acta 43: 869-884

Nakamura K., Kato Y., Tamaki K., Ishii T., 2007. Geochemistry of hydrothermally altered basaltic rocks from the Southwest Indian Ridge near the Rodriguez Triple Junction. Marine Geology 239: 125-141

Ohfuji H., Rickard D., 2005. Experimental syntheses of framboids –a review. Earth Science Reviews 71: 147-170

Otálora F., García-Ruiz J.M., 2014. Nucleation and growth of the Naica giant gypsum crystals. Chemical Society Reviews 43(7): 2013-2026

Pichler T., Ridley W.I., Nelson E., 1999. Low-temperature alteration of dredged volcanics from the Southern Chile Ridge: additional information about early stages of seafloor weathering. Marine Geology 159: 155-177

Pina C.M., 2009. Nanoscale dissolution and growth on anhydrite cleavage faces. Geochimica et Cosmochimica Acta 73: 7034-7044

Polat A., Longstaffe F., Weisener C., Fryer B., Frei R., Kerrich R., 2012. Extreme element mobility during transformation of Neoarchean (ca. 2.7 Ga) pillow basalt to a Paleoproterozoic (ca. 1.9 Ga) paleosol, Schrieber Beach, Ontario, Canada. Chemical Geology 326-327: 145-173

Putnis A., Prieto M., Fernández-Díaz L., 1995. Fluid supersaturation and crystallization in porous media. Geological Magazine 132: 1-13

Schmidt K., Garbe-Schnberg D., Bau M., Koschinsky A., 2010. Rare earth element distribution in $>400°C$ hot hydrothermal fluid from 5°S, MAR: The role of anhydrite in controlling highly variable distribution patterns. Geochimica et Cosmochimica Acta 74: 4058-4077

Seewald J.S., Seyfried Jr. W.E., 1990. The effect of temperature on metal mobility in subseafloor hydrothermal systems: constraints from basalt alteration experiments. Earth and Planetary Science Letters 101: 388-403

Seward T.M., Williams-Jones A.E., Migdisov A.A., 2014. The chemistry of metal transport and deposition by ore-forming hydrothermal fluids. Treatise Geochemistry 2nd ed. 13, pp. 29-57

Seyfried Jr. W.E., Bischoff J.L., 1979. Low temperature basalt alteration by seawater: an experimental study at 70°C and 150°C. Geochimica et Cosmochimica Acta 43: 1937-1947

Seyfried Jr. W.E., Bischoff J.L., 1981. Experimental seawater-basalt interaction at 300°C, 500 bars, chemical exchange, secondary mineral formation and implications for the transport of heavy metals. Geochimica et Cosmochimica Acta 45: 135-147

Seyfried Jr. W.E., Ding K. 1995. Phase equilibria in subseafloor hydrothermal systems: a review of the role of redox, temperature, pH and dissolved Cl on the chemistry of hot spring fluids at Mid-Ocean Ridge. In: Humphris S.E., Zierenberg R., Mullineaux L., Thomson R. (Eds.), Seafloor Hydrothermal Systems: Physical, Chemical, Biological and Geological Interactions. Geophysical. Monograph, Vol. 91. American Geophysical Union, pp. 248-272

Seyfried Jr. W.E., Mottl M.J., 1982. Hydrothermal alteration of basalt by seawater under

seawater-dominated conditions. Geochimica et Cosmochimica Acta 46: 985-1002

Seyfried Jr. W.E., Pester N.J., Ding K., Rough M., 2011. Vent fluid chemistry of the Rainbow hydrothermal system (36°N, MAR): Phase equilibria and in situ pH controls on subseafloor alteration processes. Geochimica et Cosmochimica Acta 75: 1574-1593

Shanks W.C., Bischoff J.L., Rosenbauer R.J., 1981. Seawater sulfate reduction and sulfur isotope fractionation in basaltic systems: Interaction of seawater with fayalite and magnetite at 200-350°C. Geochimica et Cosmochimica Acta 45: 1977-1995

Staudigel H., Plank T., White B., Schmincke H.-U., 1996. Geochemical fluxes during seafloor alteration of the basaltic upper oceanic crust: DSDP sites 417 and 418. In: Bebout G. et al. (Eds.), Subduction: Top to Bottom. American Geophysical Union, Washington DC, pp. 19-38

Steefel C.I., Van Cappellen P.V., 1990. A new kinetic approach to modeling water-rock interaction: the role of nucleation, precursors, and Ostwald ripening. Geochimica et Cosmochimica Acta 54: 2657-2677

Stumm W. (1992) Chemistry of the Solid-Water Interface. John Wiley & Sons

Teagle D.A.H., Alt J.C., Halliday A.N., 1998. Tracing the chemical evolution of fluids during hydrothermal recharge: Constraints from anhydrite recovered in ODP Hole 504B. Earth and Planetary Science Letters 155: 167-182

Türke A., Nakamura K., Bach W., 2015. Palagonitization of basalt glass in the flanks of mid-ocean ridges: Implications for the bioenergetics of oceanic intracrustal ecosystems. Astrobiology 15(10); 793-803

Tómasson J., Kristmannsdóttir H., 1972. High Temperature Alteration Minerals and Thermal Brines, Reykjanes, Iceland. Contributions to Mineralogy and Petrology 36: 123-134

Wolery T.W., Jarek R.L., 2003. Software User′s Manual EQ3/6, Version 8.0, Sandia National Laboratories. Albuquerque, NM, USA

Zhang R., Zhang X., Hu S., 2015. Metal transports and enrichments in iron depositions hosted in basaltic rocks. II: Metal rich fluids and Fe origin. Journal of Asian Earth Sciences 113, 1268-1284

Zeng Z., Ouyang H., Yin X., Chen S., Wang X., Wu L., 2012. Formation of Fe-Si-Mn oxyhydroxides at the PACMANUS hydrothermal field, Eastern Manus Basin: Mineralogical and geochemical evidence. Journal of Asian Earth Science 60: 130-146

# 4.8 Appendix

Supplementary table S1. Major element fluid chemistry, given in *mmol/L*

**95°C**

| t (days) | Al | Ca | Fe | K | Mg | Mn | Na | S | Si |
|---|---|---|---|---|---|---|---|---|---|
| 0.083 | 0.002 | 7.066 | 0.000 | 1.537 | 0.948 | 0.003 | 9.530 | 10.596 | 0.444 |
| 0.583 | 0.002 | 9.744 | 0.000 | 1.262 | 0.584 | 0.002 | 7.442 | 12.449 | 0.632 |
| 1.000 | 0.003 | 11.335 | 0.000 | 0.632 | 0.252 | 0.002 | 3.532 | 12.495 | 0.530 |
| 2.000 | 0.003 | 11.767 | 0.000 | 0.439 | 0.149 | 0.002 | 2.280 | 12.430 | 0.466 |
| 3.000 | 0.003 | 12.171 | 0.000 | 0.348 | 0.104 | 0.002 | 1.728 | 12.658 | 0.446 |
| 6.000 | 0.002 | 13.858 | 0.000 | 0.387 | 0.123 | 0.004 | 1.835 | 14.526 | 0.506 |
| 8.000 | 0.001 | 13.531 | 0.000 | 0.212 | 0.054 | 0.002 | 0.936 | 13.656 | 0.391 |
| 13.000 | 0.001 | 13.277 | 0.000 | 0.154 | 0.039 | 0.001 | 0.663 | 13.225 | 0.349 |
| 17.000 | 0.001 | 15.038 | 0.000 | 0.135 | 0.037 | 0.001 | 0.553 | 14.857 | 0.343 |
| 23.000 | 0.001 | 15.180 | 0.000 | 0.104 | 0.034 | 0.001 | 0.415 | 14.910 | 0.324 |
| 34.000 | 0.001 | 14.307 | 0.000 | 0.073 | 0.030 | 0.001 | 0.286 | 13.980 | 0.288 |
| 48.000 | 0.002 | 14.098 | 0.000 | 0.139 | 0.098 | 0.001 | 0.564 | 14.005 | 0.628 |
| 56.000 | 0.002 | 14.574 | 0.000 | 0.089 | 0.084 | 0.001 | 0.363 | 14.323 | 0.396 |

**110°C**

| t (days) | Al | Ca | Fe | K | Mg | Mn | Na | S | Si |
|---|---|---|---|---|---|---|---|---|---|
| 0.333 | 0.003 | 15.223 | 0.000 | 0.163 | 0.094 | 0.001 | 0.800 | 15.119 | 0.694 |
| 1.000 | 0.003 | 11.131 | 0.000 | n.d. | 1.117 | 0.005 | 26.468 | 18.949 | 0.511 |
| 2.000 | 0.002 | 14.075 | 0.000 | 0.841 | 0.323 | 0.002 | 4.911 | 16.273 | 0.511 |
| 3.000 | 0.001 | 15.385 | 0.000 | 0.523 | 0.204 | 0.002 | 2.589 | 16.478 | 0.470 |
| 6.000 | 0.001 | 15.674 | 0.000 | 0.350 | 0.156 | 0.001 | 1.740 | 16.285 | 0.441 |
| 14.000 | 0.001 | 15.959 | 0.000 | 0.212 | 0.119 | 0.001 | 1.053 | 16.135 | 0.409 |
| 17.000 | 0.003 | 14.245 | 0.000 | 0.471 | 0.323 | 0.003 | 2.404 | 15.459 | 0.960 |
| 18.000 | 0.003 | 15.073 | 0.000 | 0.194 | 0.108 | 0.001 | 0.837 | 15.059 | 0.701 |

Table S1 continued: Major element fluid chemistry, given in mmol/L

**120°C**

| t (days) | Al | Ca | Fe | K | Mg | Mn | Na | S | Si |
|---|---|---|---|---|---|---|---|---|---|
| 0.125 | 0.001 | 10.510 | 0.000 | 2.614 | 1.190 | 0.008 | 17.120 | 21.522 | 0.758 |
| 1.000 | 0.003 | 9.671 | 0.000 | 0.978 | 0.329 | 0.009 | 5.789 | 13.079 | 1.086 |
| 4.000 | 0.001 | 9.362 | 0.000 | 0.263 | 0.103 | 0.007 | 1.646 | 10.967 | 1.065 |
| 8.000 | 0.001 | 9.494 | 0.000 | 0.095 | 0.049 | 0.003 | 0.863 | 10.427 | 0.954 |
| 14.000 | 0.000 | 9.579 | 0.000 | 0.052 | 0.029 | 0.002 | 0.575 | 10.197 | 0.889 |

**140°C**

| t (days) | Al | Ca | Fe | K | Mg | Mn | Na | S | Si |
|---|---|---|---|---|---|---|---|---|---|
| 0 | 0.000 | 9.654 | 0.000 | 0.325 | 0.330 | 0.003 | 3.152 | 10.402 | 0.038 |
| 0.1 | 0.000 | 6.924 | 0.000 | 1.860 | 2.193 | 0.015 | 20.957 | 11.176 | 0.459 |
| 2 | 0.021 | 3.551 | 0.000 | 0.413 | 0.124 | 0.003 | 2.699 | 4.276 | 1.720 |
| 7 | 0.016 | 6.545 | 0.003 | 0.663 | 0.108 | 0.003 | 3.995 | 8.222 | 2.106 |
| 11 | 0.013 | 1.463 | 0.013 | 0.151 | 0.073 | 0.002 | 1.071 | 1.895 | 0.252 |

# 5    Conclusions and perspective

Sulphur-bearing minerals play a large role in oceanic hydrothermal systems, contributing to and resulting from porosity changes in the oceanic lithosphere. The goal of this project was to investigate the replacive processes that form sulphur-bearing phases and look at their relation with rock porosity. In hydrothermal systems, off-axis infiltration and heating of seawater can lead to precipitation of anhydrite, which clogs the shallow crust. Deeper percolation results in a reactive fluid that can leach and transport metals from the host rock. Upflow and mixing of this fluid with other hydrothermal fluids or infiltrated seawater can form sub-seafloor precipitates of sulphides and sulphate as wall rock replacement or it can discharge from the seafloor and grow sulphate-sulphide chimneys. All three stages in the convection cell have a significant role for sulphur and can affect rock porosity.

Seawater recharge can result in anhydrite vein formation at high temperatures. Our flow-through experiments showed that this process might take a long time at temperatures below $120°C$ and concentrates in already existing fluid pathways. On these paths, Fe-bearing minerals also occur and they capture the oxidation state of the system, with hematite formation under oxidizing and magnetite under more reducing conditions. Around $140°C$, some of the dissolved sulphate may be reduced and precipitated as pyrite. This thermochemical sulphate reduction by iron implies that less free ions are available in solution as energy source for microorganisms. The shallow seafloor may therefore be less habitable than previously thought.

Sulphide formation from the reactive hydrothermal fluid within the crust was found to be strongly dependent on oxidation state. Our batch experiments placed olivine, troctolite, basalt and serpentinite in contact with a $H_2S$-rich hydrothermal fluid. Only the basalt showed growth of pyrite crystals where olivine, troctolite and serpentinite resulted in magnetite precipitation. The $H_2$-production related to olivine hydration during fluid-rock interaction likely kept sulphur activity in these systems too low to result in sulphide formation, something not predicted by the used chemical models. Additionally, high Si-activity in plagioclase bearing rocks might cause partial suppression of magnetite, pyrrhotite and pyrite as hydrogarnet is more stable. This feature was observed in the troctolite experiment. Although the secondary minerals grew freely on the powdered reactants, their formation is considered replacive since we did not add any metal source in the fluid and iron was provided by primary mineral dissolution. This replacive sulphidation is

thus expected to be most extensive in basalt-hosted systems.

Discharging hydrothermal fluids mix with seawater and precipitate sulphate chimneys. The chimney conduit is shielded from direct contact with seawater and corrodes the formed anhydrite. Released sulphur is reduced and can precipitate as sulphide minerals. Pyrite, chalcopyrite and sphalerite assemblages were detected in pore spaces on anhydrite grain boundaries. Pyrite crystals are often surrounded by colloform chalcopyrite, showing that fluid temperatures increased after pyrite growth. The rims of chalcopyrite contain small crystals of pyrite and sphalerite, indicating a temperature decrease. Grain boundaries thus have successfully captured fluid evolution, meaning they were connected to the fluid for some time, forming a permeable network. Additionally, pyrite is observed within anhydrite cleavage planes where it nucleates directly on the dissolving surface. Both occurrences of sulphide minerals within the chimney show the vital role of porosity for the progress of sulphide formation and fluid infiltration.

Based on these results, the three formation stages of sulphur-bearing minerals (anhydrite in the recharge zone, sulphidation in the sub-seafloor, chimney formation upon discharge) show that fluid flow and oxidation control the formed mineral assemblage. Anhydrite can temporarily clog permeable crust while in chimneys it provides a substrate for sulphide formation. In the sub-seafloor, sulphidation depends on the activity of sulphur in the fluid, which is regulated by lithology but also by water-to-rock ratio, which is directly coupled to rock porosity. The need for models that correctly predict both flow related processes and chemical equilibrium processes becomes very clear. With this multi-approached study I hope to have contributed to our understanding of the role rock porosity plays in the reaction progress of processes related to the formation of sulphur-bearing minerals.

# 6    Acknowledgements

I would like to thank Wolfgang Bach for his supervision and the freedom to make slight changes to the original project plan when other opportunities arose. I am very happy that I have had the opportunity to perform a PhD under his supervision.

I am especially thankful to Jürgen Koepke, who agreed to be the second examinator of this thesis on short notice. I also want to thank Bjørn Jamtveit, Suzanne McEnroe and Margot Godard for the opportunity to visit their institutes and learn from their experience on physical and chemical modelling, magnetic rock properties and experimental techniques.

I would like to thank Oliver Plümper for his involvement in the first part of this thesis. The idea to use FIB-SEM and TEM on the sulphide-sulphate contact has greatly contributed to the value of this work.

I want to thank everyone in the Abyss project for their feedback and lively discussions on our half-annual meetings. Especially the trainees: Adriana, Justine, Sofia, Kristina, Manu, Manolis, Barbara, Rachael, Zeudia, Carlotta, Val, Thomas, Pavel and Aurelien, I look forward to keep meeting all of you in the future and see where our careers lead us.

I also want to mention the support of my working group colleagues, both in scientific discussions and during practical challenges in the lab. I especially want to thank Patrick Monien for his support in the lab, Christian Hansen for the assistance during the setup of the batch reactors, and to Wolf-Achim Kahl for help with the preparation of the flow-through setup.

I want to thank my parents and parents in law for their interest in my project and support during this work. My parents have supported my scientific interest since I was very young and have made it possible for me to follow this path.

I also want to mention some friends here in Germany: Nikki, Dominik, Björn and Gabi, thank you for helping me to get settled in Germany and for your support, especially during the last weeks of the thesis.

Tot slot wil ik Simon Veldhuijzen bedanken voor zijn steun tijdens dit hele project. Zonder jou was het me nooit gelukt.

# 7   Affirmation

**Versicherung an Eides Statt /** *Affirmation in lieu of an oath*

**gem. § 5 Abs. 5 der Promotionsordnung vom 15.07.2015 /**
*according to § 5 (5) of the Doctoral Degree Rules and  Regulations of 15 July, 2015*

Ich / I, _____

(Vorname / First *Name*, Name / *Name*, Anschrift / *Address*, ggf. Matr.-Nr. / *student ID no., if applicable*)

versichere an Eides Statt durch meine Unterschrift, dass ich die vorliegende Dissertation selbständig und ohne fremde Hilfe angefertigt und alle Stellen, die ich wörtlich dem Sinne nach aus Veröffentlichungen entnommen habe, als solche kenntlich gemacht habe, mich auch keiner anderen als der angegebenen Literatur oder sonstiger Hilfsmittel bedient habe und die zu Prüfungszwecken beigelegte elektronische Version (PDF) der Dissertation mit der abgegebenen gedruckten Version identisch ist. / *With my signature I affirm in lieu of an oath that I prepared the submitted dissertation independently and without illicit assistance from third parties, that I appropriately referenced any text or content from other sources, that I used only literature and resources listed in the dissertation, and that the electronic (PDF) and printed versions of the dissertation are identical.*

Ich versichere an Eides Statt, dass ich die vorgenannten Angaben nach bestem Wissen und Gewissen gemacht habe und dass die Angaben der Wahrheit entsprechen und ich nichts verschwiegen habe. */ I affirm in lieu of an oath that the information provided herein to the best of my knowledge is true and complete.*

Die Strafbarkeit einer falschen eidesstattlichen Versicherung ist mir bekannt, namentlich die Strafandrohung gemäß § 156 StGB bis zu drei Jahren Freiheitsstrafe oder Geldstrafe bei vorsätzlicher Begehung der Tat bzw. gemäß § 161 Abs. 1 StGB bis zu einem Jahr Freiheitsstrafe oder Geldstrafe bei fahrlässiger Begehung. / *I am aware that a false affidavit is a criminal offence which is punishable by law in accordance with § 156 of the German Criminal Code (StGB) with up to three years imprisonment or a fine in case of intention, or in accordance with § 161 (1) of the German Criminal Code with up to one year imprisonment or a fine in case of negligence.*

_____          _____
Ort / *Place*, Datum / *Date*                               Unterschrift / *Signature*